

Design and Manufacture of Anisotropic Dry Adhesives for MEMS Compatible
Pick and Place

by

Walid Bin Khaled

A thesis submitted in partial fulfillment of the requirements for the degree of

Master of Science

Department of Mechanical Engineering
University of Alberta

© Walid Bin Khaled, 2014

Abstract

Directionality or anisotropy is one of the benchmark properties of gecko adhesion, allowing geckos to adhere strongly to a surface and detach easily with little effort. Geckos achieve anisotropy by means of intricate micro-nano hierarchical structures on its feet, which is very difficult to mimic in synthetic versions. This work demonstrates that directionality can be induced on otherwise isotropic mushroom shaped fibers simply by incorporating a defect on the edges of the cap surface in a 2-step photolithography process, thus taking advantage of what is usually considered as an undesirable effect. A hypothesis based on linear beam theory is presented to explain the phenomena of defect-dependent adhesion of cylindrical fibers, and the hypothesis is confirmed with finite element analysis on mushroom shaped fibers and empirical data. The adhesion strength and directionality of the fibers were found to depend on the shape, position and size of the defect which could be tailored based on the application of the adhesive.

Synthetic dry adhesives are commonly manufactured by a casting method using thermoset polymers such as polydimethylsiloxane (PDMS) and polyurethane, a procedure which has drawbacks such as long processing times, requirement of a vacuum, and relatively expensive base materials. Styrene-ethylene/butylene-styrene (SEBS) thermoplastic elastomer is introduced in this work as an alternative material for the manufacturing of mushroom-shaped adhesive fibers. Surface contamination tests using X-ray Photoelectron Spectroscopy (XPS) reveals that the SEBS thermoplastic elastomers are less likely to transfer oligomers upon contact with a die surface compared to polydimethylsiloxane (PDMS) and polyurethane, thus rendering this

material more suitable for sensitive gecko adhesive applications such as MEMS pick and place. With a comparable adhesion strength, along with the added advantages of much faster manufacturing using thermo-compression molding, scalability, less expensive and non-toxic raw materials, thermoplastic elastomers appear to be better suited for large scale manufacturing of these bio-mimetic adhesives.

Preface

This thesis is an original work by Walid Bin Khaled under the supervision of Dr. Dan Sameoto. All of the work presented henceforth was conducted in the Polymer Microfabrication lab and nanoFab located at the University of Alberta. Sections of chapter 2, 3 and 4 have been published as W. B. Khaled and D. Sameoto, "Anisotropic dry adhesive via cap defects," *Bioinspiration & Biomimetics*, **8**(4), 044002, 2013. Sections of chapter 5 have been published as W. B. Khaled and D. Sameoto, "Fabrication and characterization of thermoplastic elastomer dry adhesives with high strength and low contamination," *ACS Appl. Mater. Interfaces* 2014. Available: <http://dx.doi.org/10.1021/am500616a>. Sections of chapter 5 have also been published in W. B. Khaled and D. Sameoto, "Manufacture of mushroom shaped dry adhesives by thermo-compression molding of thermoplastic elastomers," *Proceedings of the Annual Meeting of the Adhesion Society*, 2014. Sections of chapter 4 have been published in W. B. Khaled and D. Sameoto, "The Deliberate Defect: A Facile Method for Mass Manufacture of Anisotropic Dry Adhesives," *Proceedings of the Annual Meeting of the Adhesion Society*, 2013.

I was responsible for all the manufacturing, data collection, analysis and composition of the manuscripts mentioned above. Dr. Dan Sameoto was the supervisory author and was involved with concept formation, experimental design, data analysis and manuscript composition. The adhesion test system referred to in section 3.5 was designed by Brendan Ferguson with the assistance of Dr. Dan Sameoto.

Acknowledgements

First and foremost, the author would like to thank Dr. Dan Sameoto for his continuous guidance and mentorship, without which it would not be possible to successfully complete this work. The author would also like to acknowledge colleagues Brendan Ferguson, Ben Bschaden and Abdul Wasay from Mechanical Engineering for their assistance in fabrication, testing and finite element modeling, Dr. Shafiul Azam from Chemical and Materials Engineering and Dr. Dimitre Karpuzov from Alberta Centre for Surface Engineering and Science (ACSES) for their valuable advice on X-ray Photoelectron Spectroscopy. In addition, the author would like to acknowledge CMS Microsystems for providing access to COMSOL Multiphysics®, Natural Science and Engineering Research Council of Canada (NSERC) and Micralyne Inc. for funding of the research under the strategic grants program.

Contents

Abstract.....	ii
Preface	iv
Acknowledgements.....	v
List of figures.....	viii
List of Tables	xiii
Glossary of Terms and Symbols	xiv
1. Gecko-inspired anisotropic adhesive.....	1
1.1 Introduction to gecko adhesion.....	1
1.2. Gecko attachment: van der Waals force or Capillary force?	1
1.3. Adhesion models.....	3
1.4.Gecko feet hierarchy and its locomotion principle.....	6
1.5.Synthetic anisotropic adhesives	9
1.6. Applications of gecko-inspired synthetic adhesives:	15
1.7. Research objective	17
2. Anisotropic adhesion via cap defects	20
2.1 Stress analysis of cylindrical fiber cap surface using linear beam theory.....	20
3. Methodologies, fabrication and testing	27
3.1 Fabrication of W1 adhesives:.....	28
3.2 Fabrication of W2 adhesives:.....	31
3.3. Fabrication of Hot-embossed anisotropic adhesive:	37
3.4. Fabrication of the carbon black composite by compression molding:.....	41
3.5. Adhesion Testing:.....	44
4. Adhesion characteristics of the polyurethane anisotropic adhesives	46
4.1. Finite element analysis of fibers with defective cap.....	47
4.2 Adhesion test result of W1 polyurethane adhesives:.....	51
4.3 Adhesion test results of W2 adhesives:.....	56
4.4 Adhesion tests at higher preloads:	64
4.5 Adhesion Force of the Hot-embossed W3 adhesives	66
4.6 Carbon Black-polyurethane composite adhesives.....	67

5. Thermoplastic elastomer as the structural material for dry adhesives	71
5.1 Background	71
5.2. Surface analysis using X-Ray Photoelectron spectroscopy (XPS):.....	75
5.2.1. XPS parameters used in the surface contamination tests:.....	79
5.2.2. Sample preparation	79
5.2.3 XPS Results:.....	81
5.3 Wire-bonding test:.....	88
5.4. Fabrication of SEBS thermoplastic elastomer adhesive samples by thermo- compression molding.....	89
5.5. Performance comparison between Kraton SEBS and polyurethane adhesives: ...	94
5.5.1. Durability comparison between Kraton and polyurethane samples.....	99
5.5.2: Real time test data:.....	102
5.6 Conductive thermoplastic elastomers:.....	104
Conclusion	107
Future Works.....	110
List of Publications.....	111
Bibliography	112
Appendix.....	123

List of figures

Figure 1.1: Schematic diagram of a peeling test 6

Figure 1.2: (a) Hierarchy of gecko structure showing the meso-scale lamella, micro-scale setal array and nano-scale spatula. (Reprinted with permission [25]); (b) magnified view of the spatula. (Reprinted with permission[26]). 7

Figure 1.3: Illustration of gecko locomotion. The figure on the top right shows how the toes roll backwards during detachment. (Reprinted with permission [27])..... 8

Figure 1.4:(a) Angled polypropylene microfibers ($E \sim 1.5\text{GPa}$) produced by rolling action on vertical fibers. (Reprinted with permission [31]). (b) Angled nanofibers produced by casting polyurethane acrylate on silicon template. (Reprinted with permission [32]).(c)Micro-nanohierarchical structure produced using a 2-step UV assisted capillary molding. (Reprinted with permission[32]). (d) Tilted hierarchical polyurethane fibers formed by casting into PDMS negative. (Reprinted with permission[24]). (e) Triangular tip micro-pillars produced by casting PDMS on Si-Glass template. (Reprinted with permission [33]). (f) Angled polyurethane fibers with tip, produced by casting and dipping technique. (Reprinted with permission [34]). (g)Directional polymer stalks formed by casting polyurethane onto hard wax. (Reprinted with permission[35]). (h) Vertical semi-circular microfibers produced by casting PDMS on Silicon template. (Reprinted with permission [36]). (i) Fibers with offset rectangular caps produced by casting PDMS on photolithographically produced photoresist mold. (Reprinted with permission[37]). (j) Tilted Janus micro-pillars produced by subjecting vertical PDMS pillars to Ar^+ ions. (Reprinted with permission[38]). (k) Inclined multiwalled carbon nanotubes produced by LPCVD followed by compression and sliding. (Reprinted with permission[39]). 11

Figure 2.1: Schematic diagrams showing the bending of a beam fixed at one end due to: (a) Shear load at tip; (b) Bending moment at tip and (c) Combination of shear load and bending moment at tip. The zoomed in top views shows infinitesimally small crack at the edge of the columns. The image is published by the author in [65] and is reprinted with permission. 22

Figure 2.2: Vector diagrams indicating the development of resultant normal stress on top of the surface of a fiber due to the counteracting shear load and bending moment as indicated in 23

Figure 3.1: Schematic illustration of the fabrication steps to produce the anisotropic adhesive 28

Figure 3.2: SEM images of the eight anisotropic adhesive samples of W1 mold consisting of fibers with circular and square caps and different defect shapes or sizes. C1 – C4 and S1 - S2 has bar shaped defects. C5 and C6 has square and toroid shaped defects respectively. Inset shows the microscopic top views. The last two images

show the array of C3 and S1 fibers from the side. The image is published by the author in [65]and is reprinted with permission.....	30
Figure 3.3: SEM images of the different adhesive samples from W2 mold demonstrating the three dimensional appearance of the fiber caps with deliberately produced defects.....	35
Figure 3.4: SEM images showing the relative fiber dimensions of the (a) square arrayed circular fibers, (b) hexagonal arrayed circular fibers and (c) square arrayed square fibers. Notice how the square arrayed circular fibers were relatively slender as compared to the other two arrangements even though all of them were subject to the same exposure doses and development time. The square array of circular caps during the DUV exposure step of fabrication would allow more light to pass between the caps as compared to the square array of square caps and the hexagonal array of circular caps, resulting in more undercut for the square arrayed fibers with circular caps.	36
Figure 3.5: Schematics for the fabrication of the hot-embossed anisotropic adhesive mold.	39
Figure 3.6: SEM images showing the hot-embossed W3 anisotropic adhesive samples. The roughness of the cap surface is a result of the micro-masking effect during the last reactive ion etching step.	40
Figure 3.7: Schematics showing the fabrication of the Carbon Black-Polyurethane composite	41
Figure 3.8: Uncured viscous composite molds before passing through the rollers	43
Figure 3.9: Adhesives made out of composite materials. Picture on the left has the composite adhesive portion embedded in plain polyurethane. Picture on the right shows a composite adhesive sample attached to a rigid backing of acrylic.....	43
Figure 3.10: (a)Schematic of the adhesion testing process showing (i) Preloading;.....	44
Figure 4.1: Sectional views showing the distribution of First-Piola Kirchhoff stress normal to the cap for a fiber with defective cap in fixed contact with a flat substrate. The fibers are pulled 10 μ m in the normal direction with the addition of 10 μ m shear displacement for (c). (a) and (c) corresponds to C1 (Figure 3.2) with 3.7 μ m defect width; (b) corresponds to C3(Figure 3.2) with 9.5 μ m defect width. It is obvious from figure (a) that the application of tensile load induces a stress concentration at the defect edge which is reduced when the cap is sheared away from the defect(c). Increasing the defect size to 9.5 μ m builds up the stress at the defect edge by more than 50%, as evident in (b). The image is published by the author in [65] and is reprinted with permission.	48
Figure 4.2: Plots of normal adhesion force against shear displacement for adhesive fibers with: (a) Square and circular caps with different defect shapes; (b) Circular caps with bar like defects of different sizes and locations; (c) Square caps with bar like defects of different sizes.C1 and S2, having small bar-like defects at the edge demonstrated the highest anisotropic adhesion. C6, with the torrid defect,	

demonstrated the least adhesion. The image is published by the author in [65] and is reprinted with permission	51
Figure 4.3: Load-drag-pull maximum adhesion force measurements in a single location for C1 adhesive designs. Drag distances are 15, 0 and -18 μm which correspond to maximum, neutral and minimum performance as seen in Figure 4.2. The image is published by the author in [65] and is reprinted with permission.	55
Figure 4.4: Bar graph comparing the maximum adhesion force of fibers as mentioned in Table 5. Bars corresponding to fibers with similar defect sizes are grouped together. The coloring scheme is the same as in Table 4.1. Each sample was tested 9 times and the mean and standard deviation was calculated and plotted.....	58
Figure 4.5: Plots of normal adhesion force vs shear displacement for samples with (a) bar-like defects; (b) bar with dimple defects and (c) rectangular defects. Inset shows defect shapes and relative size differences for each of the samples corresponding to the graphs.....	59
Figure 4.6: Plots of normal adhesion force vs shear displacement for samples with (a) finger-patterned defects; (b) rectangular defects and (c) bar-like defects. Inset shows defect shapes and relative size differences for each of the samples corresponding to the graphs. Please note that the C5 samples had hexagonal arrays of fibers with rectangular cap defects which is not to be confused with C3 samples which had square arrays of fibers with similar cap defects.....	60
Figure 4.7: Comparison of adhesion forces for samples with (a) no cap defects; and (b) central cap defects.....	61
Figure 4.8: Comparison of adhesion forces for samples with (a) small defects of similar widths and (b) large defects of similar widths.....	62
Figure 4.9: Comparison of the three fiber/cap arrangements showing the relative spacing between the caps. The square array of the circular caps apparently has the most spacing between the fibers, resulting in more undercuts for the square arrayed circular fibers from uncollimated exposure as compared to the other two arrangements.....	63
Figure 4.10: Adhesion test results of C ₁₃ polyurethane samples at larger preloads.....	65
Figure 4.11: Normal adhesion force vs shear displacement plot for the polyurethane W3 adhesives.....	66
Figure 4.12: Graph showing the log mean resistance values for different carbon black concentrations.	68
Figure 4.13: Comparison of adhesion forces of carbon black samples made out of CII mold [58]. The isotropic (non-defective) fibers are $\sim 25 \mu\text{m}$ tall, $\sim 24 \mu\text{m}$ cap diameter with $\sim 3 \mu\text{m}$ overhang and $\sim 2 \mu\text{m}$ cap thickness.	68
Figure 4.14: Comparison of adhesion between 16% carbon black-polyurethane composite adhesives and pure polyurethane adhesives made from C ₁₃ sample of W2 mold.....	69

Figure 5.1: Molecular structures of (a) Polyurethane; (b) PDMS and (c) Poly(styrene-ethylene/butylene-styrene) (SEBS). The image is published by the author in [128] and is reproduced with permission	75
Figure 5.2: Schematic diagram of an X-ray photoelectron spectrometer showing its key components	77
Figure 5.3: High resolution XPS spectra comparing control sample with (a) case 1 samples showing N 1s peaks; (b) case 3 samples showing C 1s peaks. Some of the spectrums are deliberately offset in the y-axis for clarity.	82
Figure 5.4: High resolution XPS spectra comparing control sample with (a) case 2 samples showing N 1s peaks; (b) case 2 samples showing Si 2s peaks. Some of the spectrums are deliberately offset in the y-direction for clarity.....	83
Figure 5.5: High resolution XPS spectra comparing control sample with (a) case 4 samples showing C 1s peaks; (b) case 4 samples showing Si 2s peaks. Some of the spectrums are deliberately offset in the y-direction for clarity.....	84
Figure 5.6: High resolution XPS spectra for comparing the control sample with case 5 sample showing Si 2s peaks.	85
Figure 5.7: Gold coated silicon die with 26 wire bonds. The bare ball joints with no wires were due to tip blockage which is due to the aging tip and not a bond failure.	88
Figure 5.8: Schematic diagram showing the fabrication of thermoplastic elastomer (TPE) adhesives by thermo-compression molding. (a)-(b) SEBS pellets are melted together under light pressure to form a melt, (c) a silicone rubber mold is placed on the melt a pressed down slowly until the desired force is applied, (d) after approximately 30 seconds to fill the mold, the silicone, SEBS and glass slide are removed from the hotplate and cooled before the silicone is demolded, (e) macro scale view of an SEBS adhesive sample, (f) microscopic image showing arrays of anisotropic adhesive fibers made of SEBS. The image is published by the author in [128] and is reprinted with permission.....	90
Figure 5.9: Normal adhesion force against shear displacement compared between (a) C ₁₁ and (b) C ₁₂ samples made with different materials: Kraton G1657, Kraton G1645 and ST-1060 polyurethane.	94
Figure 5.10: Normal adhesion force against shear displacement compared between (a) C ₁₃ and (b) C ₁₄ samples made with different materials: Kraton G1657, Kraton G1645 and ST-1060 polyurethane.	95
Figure 5.11: Normal adhesion force against shear displacement compared between (a) C ₃₁ and (b) C ₃₂ samples made with different materials: Kraton G1657, Kraton G1645 and ST-1060 polyurethane.	96
Figure 5.12: Normal adhesion force against shear displacement compared between (a) C ₃₄ and (b) C ₃₅ samples made with different materials: Kraton G1657, Kraton G1645 and ST-1060 polyurethane.	97
Figure 5.13: Normal adhesion force vs. shear displacement of the hot-embossed W3 adhesive prepared with different materials.	98

Figure 5.14: Comparison of the durability of the Kraton and polyurethane adhesives of the C₁₃ type: (a)-(c) durability tests with 10 cycles of 50 high-medium-low adhesion trials. The image is published by the author in [128] and is reprinted with permission..... 101

Figure 5.15: Preload (+ve force) and pull-off (-ve force) vs. time for single trials of directional adhesives at a shear displacement of 10μm away from the defect. The image is published in [126] and is reprinted with permission..... 102

Figure 5.16: Preload (+ve force) and pull-off (-ve force) vs. time graph from three consecutive adhesion test trials on smooth, unstructured SEBS (Kraton G1645 and G1657) samples. Probe velocity was 5 μm/s and the hold time at preload of 20 mN was 3 s..... 103

Figure 5.17: Dryflex fibers showing incomplete cap filling and rough cap surfaces. The dryflex material has carbon black fillers in the thermoplastic elastomer matrix... 104

Figure 5.18: Mushroom shaped fibers made from a mixture of Kraton G1657 and Dryflex C3 6068. The white spots are due to non-uniform concentration of carbon black particles in the mixture..... 105

List of Tables

Table 1.1: Summary of recent works on directional dry adhesives	10
Table 3.1: Dimensions of the different anisotropic adhesive versions of W1 mold as obtained from the SEM images and Labview Vision software. The table is published by the author in [65] and is reprinted with permission.....	31
Table 3.2: Illustration of the defect size and position for C ₁ samples.....	32
Table 3.3: Illustration of the defect size and position for C ₂ and C ₃ samples.....	33
Table 3.4: Illustration of the defect size and position for C ₄ , C ₅ and S ₁ samples	34
Table 4.1: Comparison of the maximum adhesion force of the different adhesive sub-samples with a nominal 1mN preload	57
Table 5.1: Material, conditions and durations of contact of the polymer pucks with the dies. The table is published by the author in [128] and is reproduced with permission.....	81
Table 5.2: Binding energies and relative sensitivity factors of the relevant electrons [117]. The table is published by the author in [128] and is reproduced with permission.....	81
Table 5.3: Atomic composition calculated from high resolution XPS spectrum. The table is published by the author in [128] and is reproduced with permission	86
Table 5.4: Select material properties of ST-1060 polyurethane [80], Kraton G1645 [121], and Kraton G1657 [122]. The table is published by the author in [128] and is reproduced with permission	92

Glossary of Terms and Symbols

SEBS	Styrene-ethylene-butylene-styrene
PDMS	Polydimethylsiloxane
XPS	X-ray Photo-electron Spectroscopy
IRAS	Infrared Reflection-Absorption Spectroscopy
ToF-SIMS	Time-of-flight Secondary Ion Mass Spectroscopy
FT-IR	Fourier Transform Infrared Spectroscopy
AFM	Atomic Force Microscopy
SEM	Scanning Electron Microscopy
UV	Ultra Violet
DUV	Deep Ultra Violet
JKR	Johnson, Kendal and Roberts
DMT	Derjaguin, Muller and Topolov
UHMWPE	Ultra High Molecular Weight Polyethylene
PTFE (Teflon)	Polytetrafluoroethylene
KEL-F	Polychlorotrifluoroethylene
PMMA	Polymethylmethacrylate
Nylon 66	Polyhexamethylenedipamide
PEEK	Polyetheretherketone
PSA	Pressure Sensitive Adhesives
LPCVD	Low Pressure Chemical Vapor Deposition
σ	Normal stress
E_{eff}	Effective Young's modulus
W_a	Work of Adhesion
A	Hamaker constant
h	Planck's constant

1. Gecko-inspired anisotropic adhesive

1.1 Introduction to gecko adhesion

The remarkable ability of a Gecko to climb up and down on almost all types of surfaces has perplexed researchers for decades. They can run at speeds over 1m/s on both dry and wet surfaces of different roughness and of different materials, except Teflon [1]. Not only do the gecko feet provides for strong attachment with minimal preload, thus preventing it from falling off while climbing a vertical or inverted surface, it also allows the feet to detach easily with almost no effort, thus accounting for the agility of gecko. The adhesion provided by gecko feet can theoretically support 10 times the weight of a gecko. Other benchmark properties of geckos include self-cleaning, non-self-adhering and non-stickiness by default [1]. In comparison, pressure sensitive adhesives (PSA) such as a duct tape degrade, gets dirty, self-adheres, etc. All the above-mentioned abilities of the gecko motivated scientists to investigate its locomotion in detail and consequently take a closer look at its foot structure which is responsible for providing geckos with all these abilities.

1.2. Gecko attachment: van der Waals force or Capillary force?

Early research considered several hypotheses for the gecko adhesion mechanism which included sticky secretions, suction, static electricity, interlocking, friction, etc. all of which were ruled out by 1969 after independent researches [1] . The debate continued regarding whether capillary force or van der Waals was dominant for gecko adhesion.

van der Waals forces are attractions between electrically neutral molecules and are much weaker than covalent or ionic bonds. They result from the interactions between dipoles of neighboring molecules. The dipoles could be instantaneous due to the instantaneous positions of the electrons in a molecule, or permanent arising from the electronegativity difference between atoms in a bond. An instantaneous dipole could induce a dipole in the neighboring molecule and the resulting attraction between two temporary dipoles is known as London Dispersion Force. Similarly, a permanent dipole could induce an instantaneous dipole in a nearby molecule and the resultant permanent dipole-instantaneous dipole interaction force is known as Debye force. The force between two permanent dipoles is known as Keesom force. Hydrogen bonds are very strong permanent dipole- permanent dipole attractive forces and are present between polar molecules where hydrogen is bonded with a highly electronegative atom like nitrogen, oxygen or fluorine. The dipoles produced in these bonds are much stronger because of charge concentration and hence the attractive forces between these dipoles are also significantly stronger than other dipole-dipole interactions. But they are still weaker than covalent or ionic bonds.

Autumn et al. first showed in 2002 that van der Waals forces were the major contributor [2] in gecko adhesion. But several studies conducted later questioned this claim [3-5]. Measuring the adhesion of a single gecko spatula using atomic force microscope (AFM) at different relative humidity, Huber et al. [3] and Sun et al. [4] found that the adhesion force of the spatula increases with an increase in relative humidity, proposing that surface hydration and water bridge formation might be generating the adhesive force of a spatula. Or in other words, capillary force, not van der Waals, is the major component of gecko adhesion. However, subsequent research by Puthoff et al.

[6] and Prowse et al. [7] on the effect of relative humidity on the mechanical properties of gecko setae nullified this hypothesis, demonstrating that increasing the relative humidity decreases the stiffness of the setae and increases the viscoelastic damping, which increases the adhesion of the spatula, thus invalidating the notion of water bridge formation and surface hydration. This re-asserts the original hypothesis of Autumn that van der Waals is the primary force responsible for gecko adhesion.

1.3. Adhesion models

The van der Waals force between two parallel flat surfaces, separated by a distance D , is given by [8]:

$$f_{vdw} = \frac{A}{6\pi D^3} \quad (1)$$

where A is the Hamaker constant whose value is normally in the range of 10^{-19} to 10^{-20} , depending on the material properties [8]. van der Waals forces are usually effective up to a separation distance of 50nm [9].

More useful models, suitable for biological attachments are provided by Johnson, Kendal and Roberts (JKR) and Bradley, which are outlined by Zhao et al. in [17].

According to Bradley [10], the adhesion force between two rigid (incompressible) spheres, of radii R_1 and R_2 , in contact is given by

$$P_c = 2\pi R W_a \quad (2)$$

Where $R = R_1 R_2 / (R_1 + R_2)$ and $W_a = \gamma_1 + \gamma_2 - \gamma_{12}$ is the Dupre adhesion or work of adhesion, in which γ_1 , γ_2 and γ_{12} are the surface energy of the two spheres and their interface respectively.

Johnson, Kendal and Roberts modified the classic Hertz contact theory [11] by taking into account the surface energies and adhesion and provided an expression for the adhesion of two elastic bodies in contact [12]:

$$P_c = \frac{3}{2} \pi R W_a \quad (3)$$

The resultant radius of contact between the spheres is given by

$$a^3 = \frac{R}{K} (P + 3W_a \pi R + \sqrt{\{6W_a R P_c + (3W_a \pi R)^2\}} \quad (4)$$

The apparent conflict between equation (2) and (3) was later addressed by Tabor [12, 13] who proposed a governing dimensionless parameter called the Tabor number (μ) which governs the transition from the Bradley model to JKR model [14]. The tabor number is given by [13]

$$\mu = \left(\frac{R W_a^2}{E_{eff}^2 \varepsilon^3} \right)^{1/3} \quad (5)$$

where E_{eff} is the equivalent Young's modulus given by $1/E_{eff} = (1-\nu_1^2)/E_1 + (1-\nu_2^2)/E_2$, ε is the inter-atomic spacing, $E_{1,2}$ and $\nu_{1,2}$ are Young's modulus and Poisson's ratio of the two spheres, respectively.

For $\mu < 1$, elastic deformation is insignificant and the Bradley equation would provide a good approximation. For $\mu \geq 3$, the JKR theory is applicable [14]. In the intermediate region of elasticity, other theories called Derjaguin, Muller and Topolov (DMT) [15] theory or Maugis theory (also called Maugis-Dugdale theory) [16] are applicable depending on some elastic parameter outlined in the map of elastic behavior of bodies provided by Zhao et al. [17].

While these classical theories provide good approximation for van der Waals adhesion between two spheres in contact, real biological and synthetic fibers display a variety of shapes and rarely resemble a spherical contact, rather a flat cylindrical punch would provide a better approximation. Spolenak et al. [18] theoretically investigated the effect of various contact shapes on the pull-off force for single contacts. For a rigid fibril with punch-shaped end in contact with an elastic flat surface, the pull-off force is given by [19]

$$P_c = \sqrt{8\pi E_{eff} R^3 W_a} \quad (6)$$

It must be noted that Equation (6) is only applicable for a stiff fiber in contact with an elastic flat surface and the contact radius a was assumed to be equal to the radius of the flat punch R .

Kamperman et al. [20] deduced an equation for pull-off force for a compliant flat ended fiber in contact with a flat surface of a stiff material, based on the theoretical work of Gao et al. [21]. Gao assumed the presence of an annular crack at the edge, causing stress-concentration. The pull-off force is given as

$$P_c = \left(\frac{a}{R}\right)^{\frac{3}{2}} S \sqrt{8\pi E_{eff} W_a R^3} \quad (7)$$

Where S is a shape function depending on the ratio a/R , the adhesion strength thus depending on the annular crack size at the perimeter. However, a limitation of this model is that S would become infinity when (a/R) approaches unity. So this model is only valid as long as there is an annular crack at the edge.

Peeling strength is another parameter used to demonstrate anisotropy of any adhesive. The model often used by the researchers to determine the peeling strength of dry adhesive strip is the Kendall peeling model [22] which is

$$\left(\frac{F}{b}\right)^2 \frac{1}{2hE} + \left(\frac{F}{b}\right)(1 - \cos\theta) - W_a = 0 \quad (8)$$

Where F is the peeling force, b is the width of the adhesive strip, h is the thickness of the strip, E is the elastic modulus, θ is the peeling angle and W_a is the work of adhesion.

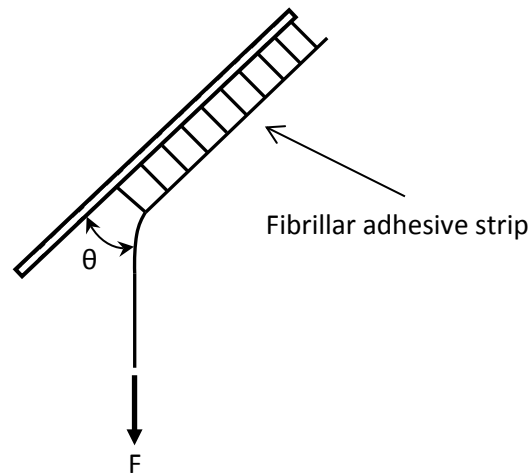


Figure 1.1: Schematic diagram of a peeling test

In this variation of the peeling test, a known load is applied at the end of the strip attached to a flat surface. The surface is tilted slowly until the onset of peeling, at which the angle θ is recorded which is the peeling angle. The adhesion energy/work of adhesion W_a is then calculated using equation (8). For anisotropic adhesives, this energy would be different depending on which end of the strip is being peeled.

1.4. Gecko feet hierarchy and its locomotion principle

Geckos have a hierarchy of micro and nano structures on the adhesive pads of its toes [23], as shown in **Figure 1.2**. The bottom of the hierarchy consists of a dense array of

slightly curved cylindrical shafts called seta, embedded in a smooth epidermal layer called lamella. Each seta is approximately $5\mu\text{m}$ in diameter, $100\mu\text{m}$ tall and inclined at angle of 45° to the lamella surface. The gap between two neighboring seta is approximately $18\mu\text{m}$ [24]. The seta branches further into hundreds of nanoscale spatular stalks (**Figure 1.2b**), each terminating into multiple thin triangular pads (5-10 nm thick, ~ 200 nm wide).

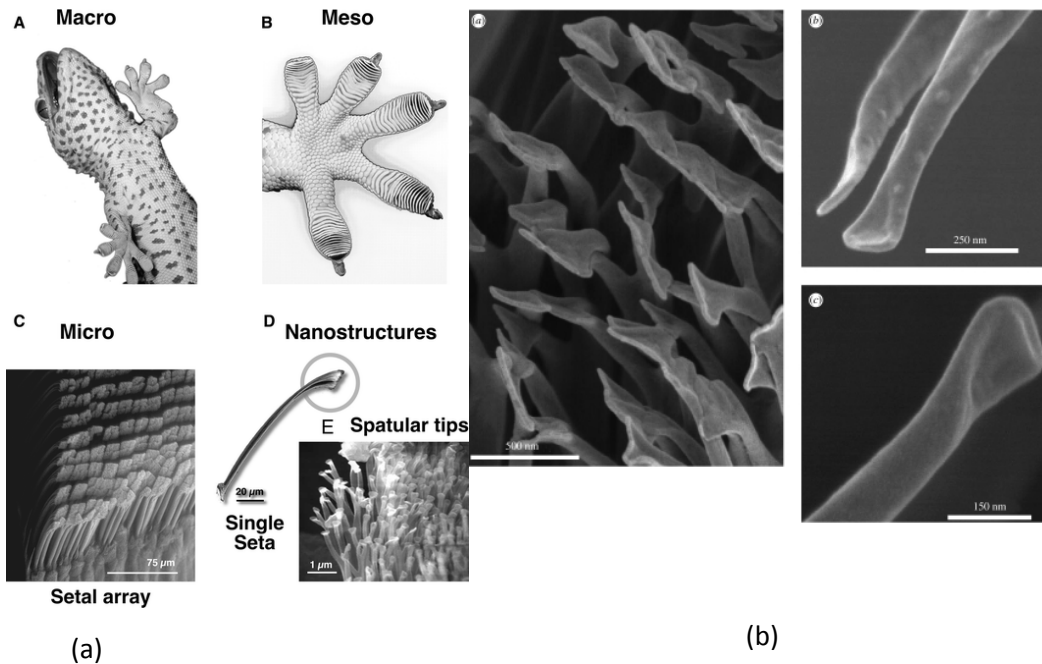


Figure 1.2: (a) Hierarchy of gecko structure showing the meso-scale lamella, micro-scale setal array and nano-scale spatula. (Reprinted with permission [25]); (b) magnified view of the spatula. (Reprinted with permission [26]).

Zhao et al. [27] described the adhesion mechanism of gecko in details. While moving, the gecko always places two diagonally opposite feet on a surface and lifts off the other two at the same time. The attached feet along with its radially positioned toes grips inward towards the body. This results in a frictional engagement of the seta towards its tilt direction, which in turn closes the crack between the nano-scale spatular pad and

the attaching surface. The seta angle drops below 30° during attachment. During detachment, the feet and its toes relax the grip followed by the rolling backward of the toes at a wide angle. The setal arrays slide opposite to the tilt direction, increasing the seta angle to more than the critical angle of 30° [28] causing the spatula stalk angle to increase. A crack opens up between the spatular pad and the attaching surface and rapidly propagates causing detachment of the spatular pad.

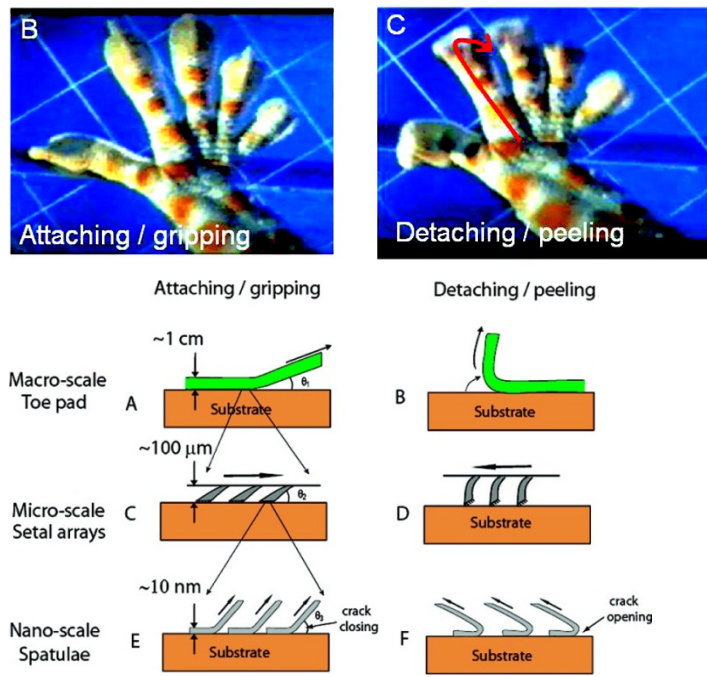


Figure 1.3: Illustration of gecko locomotion. The figure on the top right shows how the toes roll backwards during detachment. (Reprinted with permission [27])

Experiments conducted by Zhao et al. [29] and Autumn et al. [30] also showed that the gecko setal arrays demonstrate anisotropic adhesion even without the peeling action of the toes. Strong adhesion and friction was observed when the setae were sheared in the “gripping” direction (towards the tilt) whereas negligible adhesion and low friction was observed when sheared in the “releasing” direction (away from the tilt).

1.5. Synthetic anisotropic adhesives

Following the discovery that van der Waals is the primary force responsible for gecko adhesion [2], numerous researches were carried out across the world to create synthetic versions of the dry-adhesives, attempting to imitate one or more of the benchmark properties of gecko adhesion [1]. Anisotropy or directional adhesion being one of them, researchers employed various fabrication methods and materials to create fibers demonstrating anisotropic adhesion (**Figure 1.4**). Some fabricated angled fibers [24][31][32][35] and angled fibers with tilted caps [34] mimicking the angular orientation of a gecko seta. Others fabricated asymmetric fibers and/or tip, for example fibers with triangular tips [33], vertical semi-circular fibers [36], vertical fibers with offset caps [37][40], etc. Summary of some recent works on directional adhesives is presented in **Table 1.1**. Refer to the review of Sameoto and Menon [78] for details on additional works on isotropic/anisotropic dry adhesives.

Moon et al. [38] (**Figure 1.4**) fabricated tilted fibers by first producing vertical micro-pillars of PDMS using photolithography and soft-lithography and then subjected the micro-pillars to Ar⁺ ion radiation from a side, i.e. the ion beams incident angle was parallel to the backing layer of the micro-pillars. Irradiating with ions from a side caused the exposed side of the micro-pillars to stiffen and shrink resulting in tilting of the pillars towards the radiation source. The tilted micro-pillars showed better normal adhesion with respect to the vertical ones and also demonstrated anisotropy. Friction force along the tilt direction was 3 times larger than that opposite to the tilt direction.

Table 1.1: Summary of recent works on directional dry adhesives.

Shape of fibers	Fabrication of template	Material	Remarks	Reference
Angled fibers with tip	Angled photolithography, micromolding, dipping	Polyurethane	Adhesion increased with tip area. Larger the tip angle, larger the directionality	[34]
Triangular fibers with overhanging tips	Photolithography, DRIE, anodic wafer bonding	PDMS	Peeling energy greater at tip edges compared to vertices	[33]
Angled nanofibers	Plasma etching with faraday cage	Polyurethane acrylate	Shear adhesion strength towards the tilt is greater than shear adhesion strength away from the tilt	[32]
Angled nanofibers on top of vetical microfibers	2-step UV-assisted capillary molding	Polyurethane acrylate	Sustained adhesion up to a roughness of 10 μm due to the hierarchy	[32]
Tilted hierarchical fibers	Photolithography, shearing of partially cured negative mold	Polyurethane	Shear adhesion strength towards the tilt is greater than that away from the tilt	[24]
Angled fiber with an angled tip	micromachining	Polyurethane	Normal adhesion proportional to shear when sheared towards the tilt. Zero adhesion when sheared opposite to the tilt	[35]
Offset caps on square fibers	2-step photolithography	PDMS	Peeling strength from cap overhanging side greater than that from non-overhanging side	[40]
Semicircular fibers	Bosch DRIE	PDMS	Shear adhesion towards curved surface is 3 to 5 times greater than that towards flat surface	[36]
Angled nanotubes	LPCVD, compression, shearing	Multiwalled carbon nanotubes	Friction/ Shear Adhesion towards tilt direction is 40 % larger than that in the opposite direction	[39]
Angled fibers	Photolithography, soft lithography, Ar+ ion radiation	PDMS	Friction force along tilt direction was 3 times larger than that in the opposite direction	[38]

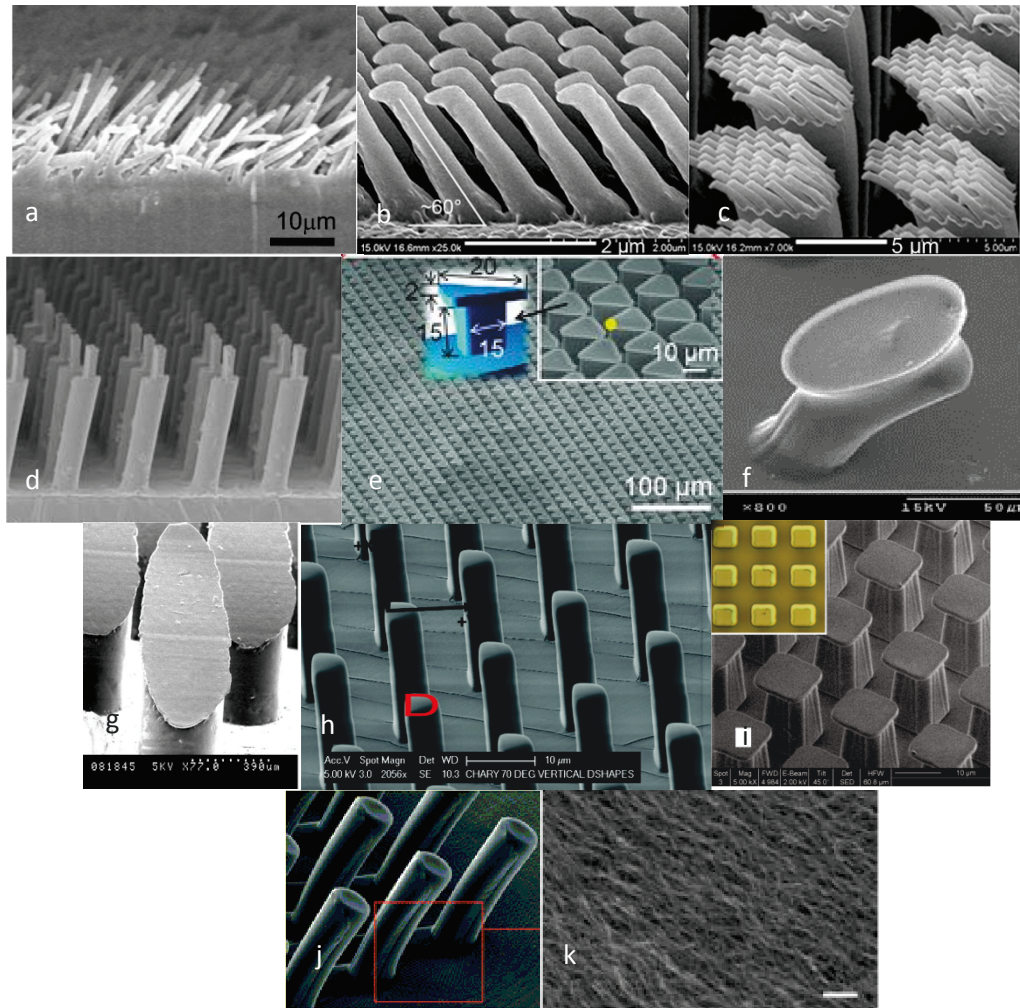


Figure 1.4:(a) Angled polypropylene microfibers ($E \sim 1.5 \text{ GPa}$) produced by rolling action on vertical fibers. (Reprinted with permission [31]). (b) Angled nanofibers produced by casting polyurethane acrylate on silicon template. (Reprinted with permission [32]). (c) Micro-nano hierarchical structure produced using a 2-step UV assisted capillary molding. (Reprinted with permission [32]). (d) Tilted hierarchical polyurethane fibers formed by casting into PDMS negative. (Reprinted with permission [24]). (e) Triangular tip micro-pillars produced by casting PDMS on Si-Glass template. (Reprinted with permission [33]). (f) Angled polyurethane fibers with tip, produced by casting and dipping technique. (Reprinted with permission [34]). (g) Directional polymer stalks formed by casting polyurethane onto hard wax. (Reprinted with permission [35]). (h) Vertical semi-circular microfibers produced by casting PDMS on Silicon template. (Reprinted with permission [36]). (i) Fibers with offset rectangular caps produced by casting PDMS on photolithographically produced photoresist mold. (Reprinted with permission [37]). (j) Tilted Janus micro-pillars produced by subjecting vertical PDMS pillars to Ar^+ ions. (Reprinted with permission [38]). (k) Inclined multiwalled carbon nanotubes produced by LPCVD followed by compression and sliding. (Reprinted with permission [39]).

Murphy et al. [34] (**Figure 1.4f**) fabricated angled microfibers with varying overhanging tip angles using techniques such as angled photolithography, micromolding and dipping. A negative template was first created using angled photolithography. Subsequent polyurethane casting and curing produced the angled fibers. The fibers were then dipped in a thin film of polyurethane and pressed to a substrate to make the mushroom tips and cured with the load on. The angle of the mushroom tips, varied from 0° to 90° in their work, depending on the pressing force on the tilted fibers during curing. The overall shear adhesion strength of the fibers increased with larger tip area, whereas larger tip angles resulted in more anisotropy (i.e. larger difference in shear resistance between the gripping and releasing direction).

Kwak et al. [33] (**Figure 1.4e**) demonstrated directional adhesion of triangular tip micropillars which they fabricated by photolithography, deep reactive ion etching, anodic wafer bonding and replica molding with PDMS. They found that the adhesion energy varied at different peeling directions (ranging from 8.8 to 17.2 mJ/cm²), the stronger adhesion being when peeled at the side of the triangular tip as opposed to the vertex. The sharp corners of the triangular tip allows the formation of a crack very easily because of the point contact, whereas the edges of the triangle forms a line contact with the attaching surface and hence it is harder to initiate a crack when peeled from the edge. The normal adhesion of the triangular tip fibers in the absence of shear was also claimed to be better as compared to angled fibers fabricated by some other groups.

Jeong et al. [32] (**Figure 1.4b**) fabricated angled nanohairs with tip by employing a faraday cage within a plasma etching system. The faraday cage directed the ions in plasma etching at an angle, producing angled nano-holes on a silicon substrate and

subsequent casting with polyurethane acrylate (PUA) produced the angled nanohairs. The angled nanofibers showed increased shear adhesion strength (when sheared towards the direction of the inclined angle) as compared to the bare PUA and also to the vertical nanohairs (21 N/cm² vs 14.5 N/cm² and 3.2 N/cm²). They also fabricated micro-nano hierarchical structure using a 2-step UV-assisted capillary molding technique. Even though the adhesion against a flat surface actually decreased (~9 N/cm² as opposed to 21 N/cm²), hierarchical structures maintained the adhesion against a rough surface of up to 10 μm after which the adhesion dropped dramatically (at 20 μm roughness).

Jin et al. [24] (**Figure 1.4d**) fabricated tilted adhesive fibers by using a shearing technique on partially cured PDMS mold. The primary mold, consisting of vertically aligned hierarchical fibers, was fabricated out of silicon using conventional photolithography. A negative replica was then made by casting PDMS onto the primary mold and demolding after partial curing. The PDMS replica was then sheared to create the inclined trenches and cured fully with the shear load on. Polyurethane was then cast and cured onto the negative mold to produce the tilted hierarchical fibers. The angle of inclination of the fibers was controlled by controlling the amount of shear applied to the partially cured PDMS mold. Adhesion testing showed that shearing the tilted fibers towards the tilt direction resulted in an increased normal and friction adhesion, as compared to those when sheared away from the tilt direction. The magnitude of the normal and shear adhesion increased with the decrease of the tilt angle ($\theta < 90$).

Kim et al. [35] (**Figure 1.4g**) fabricated and applied some directional polymer stalks under the feet of a climbing robot (sticky bot). The master mold was fabricated using hard wax and the final adhesives were made by casting polyurethane on it. The stalks

were inclined at an angle of 20° to the vertical and terminating at tips at an angle of 45° to the vertical. These adhesive patches, when sheared towards the direction of inclination, demonstrated normal adhesion proportional to the shear, and no adhesion when sheared the opposite way.

Sameoto et al. [40] (**Figure 1.4i**) fabricated offset rectangular caps on square fibers using 2-step photolithography and subsequent PDMS casting. The anisotropic fibers had large cap overhang at one side and none on the opposite side. Peeling test results show that the peel strength was greater when peeled from the non-overhanging side and weaker when peeled from the side of large cap overhang. Also, the overall peel strength increased with increase in cap overhang.

Tamelier et al. [36] (**Figure 1.4h**) reported the fabrication of anisotropic adhesive by simply creating vertically aligned semicircular fibers. The fabrication involved Bosch deep reactive ion etching process of silicon to make $19\mu\text{m}$ deep semicircular cross section trenches. The adhesive fibers were made by casting PDMS and basically had curved sidewall and a flat sidewall. Load-Drag-Pull tests on the fibers showed that the shear adhesion force of the fibers were approximately 3 to 5 times larger when the fibers were sheared towards the curved face as compared to shearing towards the flat face. Shearing towards the curved face would result in a larger contact area with the flat face as compared to the contact area with the curved face when sheared towards the flat face.

Non-polymer materials like carbon nanotubes have also been used to produce gecko-inspired adhesives. The vertically aligned carbon nanotubes showed high friction [39, 41, 42], some even larger than that of gecko. Zhou et al. [39] fabricated arrays of tilted

multi-walled carbon nanotube which demonstrated anisotropic friction depending on the sliding direction (**Figure 1.4k**). Vertical multi-walled carbon nanotubes were first produced using low pressure chemical vapor deposition with iron catalyst. The vertical nanotubes were then subjected to compression and sliding at 120 °C, causing them to tilt to an angle of ~68°. The friction force of the angled arrays of nanotubes against a steel ball was up to 40 % larger when sheared towards the tilt direction as compared to that in the opposite direction.

1.6. Applications of gecko-inspired synthetic adhesives:

The gecko-inspired synthetic adhesives have seen most of its applications in climbing robots, inspired by the original purpose of the gecko footpad fibers, which is to provide locomotion to geckos. Climbing robots traditionally relied mainly on suction caps for climbing [43-45], while magnets were also employed in some cases [46][47]. Suction caps will restrict the pace of motion of the robots as it requires some time to create the vacuum needed for suction. In addition, the requirement of a pump onboard also restricts the locomotory capabilities of the robot, and the suction caps are also useless in vacuum environments. An alternative to the suction cups are the pressure sensitive adhesives (PSA) which has potential drawbacks as well. PSA can only be used a few times with no adhesion control and leaves residues on the surface. In space conditions, they often evaporate, get brittle and degrade [48].

Magnet-based robots can only be employed on metallic surfaces, thus limiting its usability. On the other hand, the gecko-inspired, synthetic adhesives, being dependent mainly on van der Waals adhesion, would work fine on a range of materials, as well as in vacuum environments. There are several reports of isotropic/anisotropic dry adhesives

being used or proposed in robotic climbing applications [49-52]. Henrey et al. [53] developed legged sand robots with timing belts for space climbing applications, all of them utilizing PDMS adhesive fibers for climbing. Daltorio et al. [49] used micro-structured PVS strips on the wheels of their climbing robots. With the addition of a long tail of approximately 25 cm, their robots could climb vertically on smooth glass with reasonable traction. One of the best performing climbing robots called “Stickybot” were developed by Kim et al. [35]. Stickybot employed wedge-shaped directional polyurethane stalks as the attachment structure on its foot. Hierarchical conformability of Stickybot as well as the directionality of the polymer stalks allowed it to climb a range of smooth vertical surfaces including glass, glossy ceramic tile, acrylic and polished granite at speeds up to 4cm/s.

Another important application of gecko inspired adhesives is micromanipulation of small, flat objects like dies or silicon platelets. Menguc et al. [54] demonstrated how gecko-inspired angled PDMS micro-pillars can be used for manipulation of micrometer scale silicon micro-platelets as well as centimeter scale glass cover slips, with a pick to release adhesive force ratio of 39:1. Carlson et al. [55] demonstrated transfer printing of silicon platelets using PDMS stamps by using shear as a means of adhesion control during release. Kim et al. [56] used similar stamps except with four pyramidal ridges at the vertices to perform the transfer printing of silicon platelets. The maximum ratio of pick to release adhesive forces was 1000:1 in that case. However, the holding force while transferring the platelets was low and hence the stamp design was not appropriate for the transport of heavier platelets. Yang et al. [57] fabricated arrays of angled PDMS posts and demonstrated how they can potentially be used for continuous transfer of microscopic silicon platelets by attaching them to the surface of a roller.

Brendan Ferguson [58] in his thesis demonstrated how mushroom shaped isotropic dry adhesive fibers made of polyurethane can be used for MEMS pick and place applications using a shearing technique for releasing. Jeong et al. [32] demonstrated the application of hierarchical slanted nano-hairs with directional adhesion in transferring a TFT-LCD glass (47.5 x 37.5 cm²). He utilized the frictional anisotropy of the polyurethane acrylate hierarchical fibers in performing the transfer.

Dry adhesives have also been investigated for use in grappling in space. Parness et al. [48] utilized arrays of wedge shaped PDMS fibers to design a grappling tool for space applications and tested the adhesives on a variety of relevant surfaces found in satellites and space assets in earth orbit like solar panels. The adhesives worked well on smooth surfaces and did not show any significant drop in performance at -80°C under vacuum.

Another potential application of gecko adhesives is in the field of medical science. Kwak et al. [59] demonstrated the application of mushroom shaped PDMS micro-pillars as a medical patch. The adhesive strength of the patch, however, was less than half of that of the traditional acrylic patches and hence this technology requires further improvement prior to introduction in the market.

1.7. Research objective

As mentioned in the introduction and also in section 1.4, the attractive feature of gecko adhesion is not just the high normal adhesion strength but also the ability to quickly release with minimum effort, provided by the directionality of adhesion. The main objective of our research was to create a directional dry adhesive which could potentially be applied in a robotic pick-and-place system for MEMS device transfer. The research was intended for future application by Micralyne Inc., a MEMS foundry based

in Edmonton, Alberta. This research was an extension of work reported by Brendan Ferguson in his thesis [58] in which he fabricated and improved mushroom shaped dry adhesives and later applied them in a robotic pick and place system to transfer dies. He integrated parallel strips of mushroom shaped adhesives into the end effector and used a load-pull and drag-pull technique respectively for picking up and placement of $5 \times 5 \text{ mm}^2$ silicon dies. Since isotropic adhesives were used for this purpose, it would require a reasonably large shear for disengagement after placing which might damage the fibers after a certain number of cycles. Anisotropic adhesives, on the other hand, would be much easier to release and disengagement would require considerably less shear loading of the fibers. Section 1.5 discusses the different approaches researchers have made so far to create synthetic directional adhesives. Though all of these synthetic adhesives showed great promise in terms of directionality, their normal adhesion strength in the absence of shear is either not reported in many cases or they are relatively poor as compared to a non-directional adhesive. Our primary aim in this research was to take advantage of the high adhesion strength demonstrated by mushroom shaped fibers and tailor the fiber caps to induce directionality. The normal adhesion strength of such fibers would ideally be high enough to pick up small dies with a small preload, sustain the load of the dies while transferring, and disengage with minimal shearing or peeling force. A new concept is proposed to induce anisotropy on otherwise isotropic mushroom shaped fibers by deliberately positioning a defect at an edge of the overhanging cap. Chapter 2 discusses in terms of linear beam theory how the introduction of a defect on the top surface of cylindrical fibers can alter the directionality of the fibers, a hypothesis which is confirmed by the finite element analysis and adhesion test results presented in chapter 4. Chapter 3 outlines two

different ways to fabricate a master mold to produce these directional adhesives, one yielding caps with different defect sizes and the other one intended for large scale production of fibers with single cap defect size. Chapter 3 also explains the instrumentation and mechanism for testing the directional and non-directional adhesives. It also includes the recipe to produce conductive dry adhesives from a composite of polyurethane and carbon black particles which is aimed for applications requiring anti-static polymers. Chapter 4 includes analysis and discussion of the adhesion test results of the thermoset polyurethane adhesives including the polyurethane-carbon black composite, relating them to the finite element analysis and analytical studies presented in chapter 2. Chapter 5 introduces thermoplastic elastomers as alternative to the commonly used thermoset polyurethane and PDMS to produce the adhesive fibers. PDMS, polyurethane and SEBS thermoplastic elastomers are characterized in terms of oligomer transfer. Chapter 5 also shows how the thermoplastic elastomers can be processed using thermo-compression molding to make the mushroom shaped adhesive fibers and compares the thermoplastic elastomer adhesives with their polyurethane counterpart in terms of adhesion. The thermo-compression molding process can be easily modified and optimized for large scale manufacturing of dry adhesives which may not be economically feasible with the conventional casting method with thermoset polymers.

Even though our adhesives were meant to be used in a pick and place system for MEMS dies, it could also be used in other applications such as robotic climbing, grasping and tissue adhesives, as mentioned in section 1.6, all of which could benefit from the shear-dependent adhesion displayed by our adhesive fibers.

2. Anisotropic adhesion via cap defects¹

In this chapter, linear beam theory is used to illustrate the stress distribution on a cylindrical fiber tip in contact with a rigid surface and subjected to shearing. This chapter also explains how an infinitesimal crack at the tip edge might affect the adhesion of the fiber and induce anisotropy.

2.1 Stress analysis of cylindrical fiber cap surface using linear beam theory

It has been earlier demonstrated that the peeling strength of a mushroom shaped synthetic dry adhesive is significantly influenced by the amount of overhang of the cap [40]. This in turn led to the development of a directional adhesive variation solely through the use of an offset cap [37], rather than angled fibers. While this solution could result in a highly directional adhesive, the fabrication challenge of aligning relatively transparent layers through a thick layer of photoresist lead to challenges in repeatability across a full wafer. A different fabrication technique, which produced the critical cap feature first, and the underlying fiber naturally via UV exposure [60][61] was much more reliable and flexible with design parameters and this method would be adapted to produce directional dry adhesive fibers. In this work, we demonstrate how the act of deliberately introducing a defect on the overhanging portion of the mushroom shaped caps on dry adhesive fibers can produce anisotropic adhesion. The adhesion strength and the degree of directionality were found to depend on the size

¹ Sections of this chapter are published by the author in [65] and are reproduced with permission.

and location of the defect which acts as a crack initiator. Increasing the defect size decreased the overall adhesion whereas the directionality decreased when the defect was placed closer to the center of the cap, the region of high stress concentration.

Earlier reports suggest that the mushroom shaped fibers are tolerant to tiny defects on the overhanging portion of the cap and are more likely to fail due to crack nucleation at the center of the cap and its subsequent propagation outwards [62]. But in this case the defect is large enough to overcome the compressive force acting on the overhanging portion of the cap during tensile loading of the fiber. Hence stress concentrates at the defect edges resulting in the crack nucleation and propagation towards the center of the cap surface, ultimately causing detachment, similar to the failure mechanism of cylindrical fibers without any overhanging cap [21][63][64].

The phenomena of shear loading of a dry adhesive fiber with an edge defect and the resultant stress distribution can be explained using linear beam theory. For the purpose of modeling, the adhesive fiber can be considered as a vertical cylindrical column fixed at the bottom. The column tip is assumed to be in perfect contact with another flat smooth surface except for an infinitesimal crack located on one edge. It will be assumed that failure of the fiber will occur immediately if the crack experiences a tensile load, but will otherwise be maintaining contact with the flat surface. Should a positive tensile load be applied to the fiber in this case, the crack will fail immediately, but the column can be loaded with a shear load and a counteracting bending moment to create an equilibrium condition as shown in **Figure 2.1(c)**, in which the resultant slope angle at the column tip is zero (maintaining contact with the opposing surface and assuming the surface and fiber base can move relative to one another).

If θ_1 and θ_2 are the slope angle at the column created by shear load and bending moment respectively, then the resultant slope angle due to the counteracting effect of shear load and bending moment can be expressed as θ where

$$\theta = \theta_1 - \theta_2 = 0$$

(9)

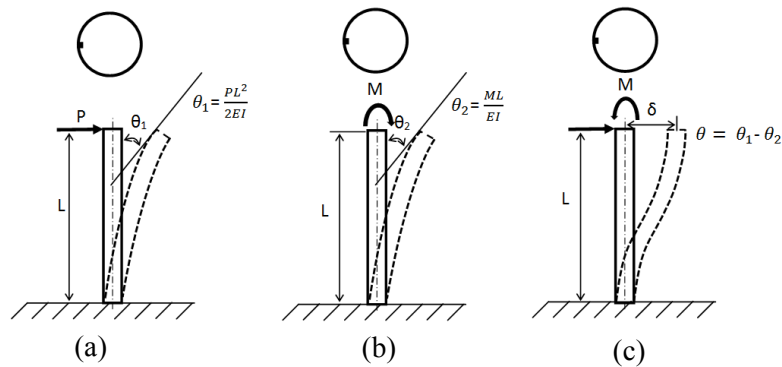


Figure 2.1: Schematic diagrams showing the bending of a beam fixed at one end due to: (a) Shear load at tip; (b) Bending moment at tip and (c) Combination of shear load and bending moment at tip. The zoomed in top views shows infinitesimally small crack at the edge of the columns. The image is published by the author in [65] and is reprinted with permission.

Substituting θ_1 and θ_2 with the respective equations [66] as mentioned in

Figure 2.1(a) and (b),

$$\frac{PL^2}{2EI} - \frac{ML}{EI} = 0$$

$$M = \frac{PL}{2} \quad (10)$$

where M is the bending moment, P is the shear load and I is the moment of Inertia of the beam.

For the boundary condition mentioned above, the shear load can be expressed as [67]

$$P = \frac{12EI}{L^3} \delta$$

where δ is the slippage or displacement of the beam tip.

With this, equation (10) can be rewritten as

$$M = \frac{12EI\delta}{2L^2} = \frac{6EI\delta}{L^2} \quad (11)$$

Now, the stresses on the tip surface for the above mentioned boundary condition can be illustrated pictorially as shown in **Figure 2.2**.

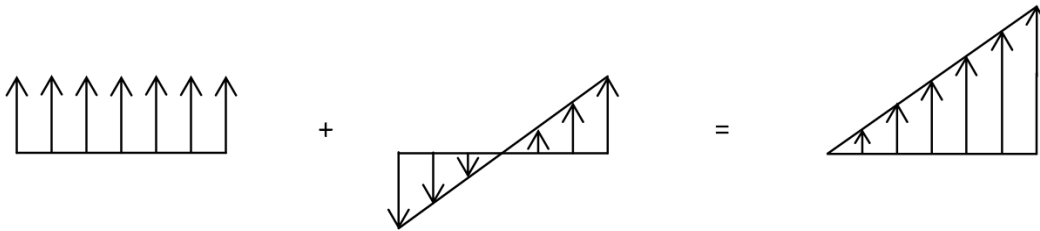


Figure 2.2: Vector diagrams indicating the development of resultant normal stress on top of the surface of a fiber due to the counteracting shear load and bending moment as indicated in **Figure 2.1(c)**. The image is published by the author [65] and is reprinted with permission.

The resultant stress on the column tip can be seen to have a gradient with minimum and maximum values at two extremities. In the actual dry adhesive fiber, positioning the defect at the maximum stress region will result in rapid loss of adhesion by crack propagation.

For the bending of a circular beam, the maximum stress can be expressed as [66]

$$\sigma_{max} = \frac{My_{max}}{I}$$

where σ_{max} and y_{max} are the maximum normal stress and vertical tip displacement respectively.

Substituting y_{max} with $d/2$ and substituting M with the expression in equation (11)

$$\sigma_{max} = \frac{6EI\delta}{L^2} \cdot \frac{d/2}{I} = \frac{3Ed\delta}{L^2} \quad (12)$$

In order to have no tensile stress at one edge, where a minute crack is located

$$\sigma_y - \sigma_{max} \leq 0$$

Substituting σ_y with F_y/A , where F_y is the tensile force and A is the area of the cross-section,

$$\frac{F_y}{A} = \frac{3Ed\delta}{L^2} \quad (13)$$

Vertical displacement of the column tip can be expressed as [67]

$$y = \frac{F_y L}{AE} \quad (14)$$

Combining equation (13) and (14), the vertical displacement, y , can be re-expressed as

$$y = \frac{3d\delta}{L} \quad (15)$$

In this case, the pull-off direction to avoid loading the crack in tension (as defined by the ratio of tangential displacement to axial displacement) is only a function of the geometry of the fiber, and not its modulus. As long as a compressive force is applied to the crack, the crack will not propagate and failure is delayed. A crack extending further from the edge of the fiber requires that a much larger shear displacement be applied or smaller elongation to maintain this compressive condition on the crack. This illustrates the basic theory behind our mechanism to control adhesion strength, but in practice, we do not have small relative displacements, perfectly cylindrical columns or geometries that match Euler beam theory and the crack can maintain a finite tensile load before

failure. For a perfect elastic cylinder in contact with a half space, the stress at pull-off before crack propagation at the edges is estimated to be [63]:

$$\sigma \approx \left(\frac{8E_{eff}\Delta\gamma}{\pi R} \right)^{1/2} \quad (16)$$

Where σ is the applied stress, $E_{eff} = ((1-\nu_f^2)/E_f + (1-\nu_s^2)/E_s)^{-1}$ is the effective modulus, where E_f , E_s , ν_f , and ν_s are the Young's moduli and Poisson's ratio of the fibers and substrate respectively and $\Delta\gamma$ is the work of adhesion between the two surfaces. In the case where the surface modulus is much higher than that of the fiber, $E_{ff} \approx E_f/(1-\nu_f^2)$. In equation 16, R is modeled as if an infinitely large crack surrounds an area of contact of radius R which results in a stress singularity at the edge of the fiber and reduces adhesion from the theoretical maximum due to van der Waals forces. The actual value for this adhesion stress before crack propagation will be different as shape factors, exact frictional conditions at the boundary and loading will all influence the stress concentrations in the fiber [32][64]. Additionally, this equation assumes that the applied stress is a constant value in tension, and through the addition of a bending moment and/or non-cylindrical fiber shapes, this assumption is no longer valid. Once the minimum stress necessary to exceed the adhesion strength is reached anywhere on a fiber, the adhesion will be rapidly lost (assuming a constant load on the fiber tip rather than a constant displacement condition).

In another recent work, Paretkar et al. investigated the buckling and unbuckling of cylindrical adhesive fibers [68]. For a buckled fiber of diameter d , subject to a tensile load T and attached to a substrate in a manner similar to what is shown in **Figure 2.1(c)**, the stress intensity factor at an edge defect of length l is given by [68]

$$K = 1.12 \frac{T}{d^2} \sqrt{\frac{l}{\pi}} \left[0.5 + \frac{4\delta}{d} \frac{\sinh\left(\frac{\sqrt{T}}{2}\right)}{\sqrt{T} \cosh\left(\frac{\sqrt{T}}{2}\right) - 2\sinh\left(\frac{\sqrt{T}}{2}\right)} \right] \quad (17)$$

Where δ is the displacement or slippage of the fiber tip. From equation (17) we can deduce that the stress intensity factor (K) varies as the square root of crack length (l), provided that other parameters remain constant. However, this equation may not be applicable for mushroom shaped fibers as the stress distribution at the cap surface of a mushroom shaped fiber is not always uniform and the tensile load T would vary radially. In addition, the hour-glass shape of our fibers introduces more complexities and makes it difficult to predict its performance by means of analytical methods. Hence we must resort to finite element analysis for more accurate stress analysis of our fibers when subjected to specific loading conditions.

3. Methodologies, fabrication and testing²

In this chapter, the fabrication technologies used to produce the adhesives in this work are described, as are the testing methodologies to determine adhesion characteristics. For the purposes of this work, non-directional adhesives were produced using the basic polymer fabrication process described in [58][60][69]. Anisotropic adhesives were produced using a modification to this basic process developed by the author, which allowed for many varieties of defects to be included on single mold designs. One anisotropic adhesive mold (labeled W1) was initially fabricated using the two-step photolithography process shown in **Figure 3.1**. The mold had three samples of hexagonal arrays of fibers with circular caps of 36 μm diameter and different defect shapes (C1-C4, C5 and C6) and one reportable sample with square arrays of fibers with square caps of 24 μm edge length (S1, S2). The second step of the photolithography (**Figure 3.1b-c**) would allow us to fabricate a predefined defect into the cap surface. Even though only one defect size was designed in the mask for each sample, it turned out that the acrylic mold, on which the SU8 caps were produced, warped slightly during the fabrication process, resulting in an axial run-out of the defects. This run-out error actually was beneficial for running experiments as it resulted in the formation of fiber caps with different defect locations across the width of the substrate. For the purpose of simplicity, the adhesive fibers with the same defect shape but different defect sizes are considered as different samples here even though they are originally from the same sample. The fabrication process is explained in details in the following paragraphs.

² Sections of this chapter are published in [65] and are reproduced from the original article.

3.1 Fabrication of W1 adhesives:

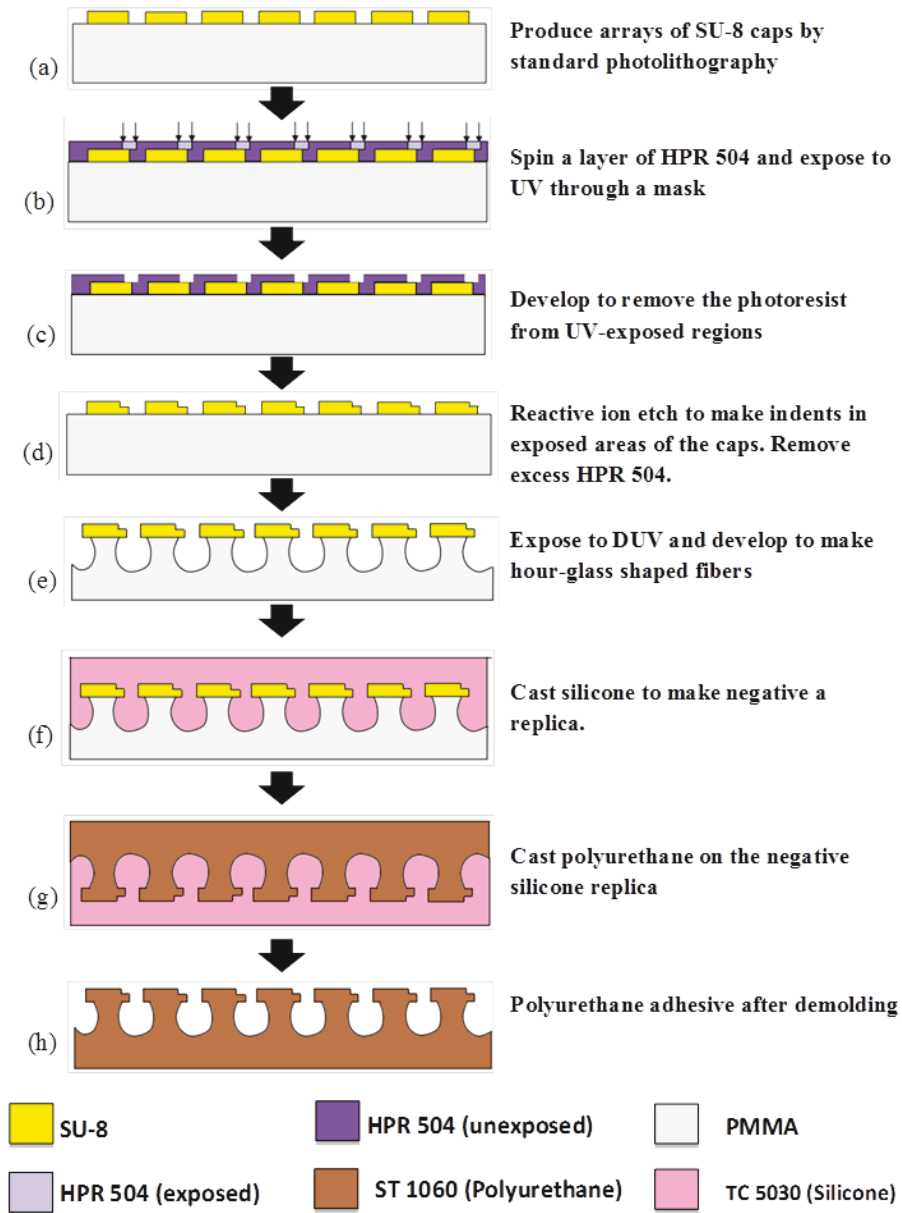


Figure 3.1: Schematic illustration of the fabrication steps to produce the anisotropic adhesive

A 5" x 5" PMMA substrate (OPTIX) was cleaned by rinsing with isopropyl alcohol and de-ionized water followed by drying with a nitrogen jet. SU-8 2002 (Microchem) was spun on the PMMA substrate at 500 rpm for 5 seconds followed by 1000rpm for 40s to achieve a thickness of approximately 2.8 μm . The spin coating was followed by soft baking at 90°C for 3 minutes in an oven to remove solvents. Exposure to a 450 mJ/cm^2 dose of 365 nm UV was then carried out through a mask followed by post exposure baking at 90°C for 20 minutes in an oven. After the post exposure baking, the substrate was developed on a spinner by spinning at 3000 rpm for 40 seconds and rinsing with SU-8 developer and isopropyl alcohol (IPA) consecutively 4 to 5 times while spinning. The SU-8 developer would remove the unexposed SU-8 while the IPA would remove the byproduct of the development reaction. . This produced arrays of SU-8 caps of circular and square shapes of 36 μm diameter and 24 μm edge length respectively (**Figure 3.1a**). A thin layer of HPR 504 (Fujifilm) was then spun on the substrate and baked at 90°C for 3 minutes in an oven. The substrate was then exposed to 25 mJ/cm^2 UV through a second mask to define the shape of the defects (**Figure 3.1b**) followed by developing in Microposit 354 developer (Shipley, MA) for approximately 30 seconds (**Figure 3.1c**). Reactive ion etching was carried out for 3 minutes with the following settings: 100 sccm of O_2 and 5 sccm of CF_4 , 150 W RF power and 125 millitorr chamber pressure, to etch down a defect of approximately 800 nm in the SU-8 layer. The remaining HPR 504 was stripped off by blanket exposing to UV and soaking in MF-319 developer (**Figure 3.1d**). The substrate was then exposed to 126 J/cm^2 of un-collimated 254 nm deep UV (DUV). The SU-8 caps block the DUV while the exposed acrylic regions would have their molecular weight lowered [70], resulting in the formation of PMMA fibers with overhanging caps upon developing in SU-8 developer (**Figure 3.1e**).

TC-5030 (BJB Enterprises) silicone rubber was cast onto the PMMA/SU-8 master mold and cured to make a negative replica (**Figure 3.1f**), followed by casting ST-1060 polyurethane (BJB Enterprises) on the silicone mold (**Figure 3.1g**) and curing. The polyurethane is then demolded, which is the final adhesive sample (**Figure 3.1h**). As mentioned before, the slight warping of the PMMA substrate resulted in the formation of fiber caps with different defect sizes. The samples from W1 mold are shown in **Figure**

3.2.

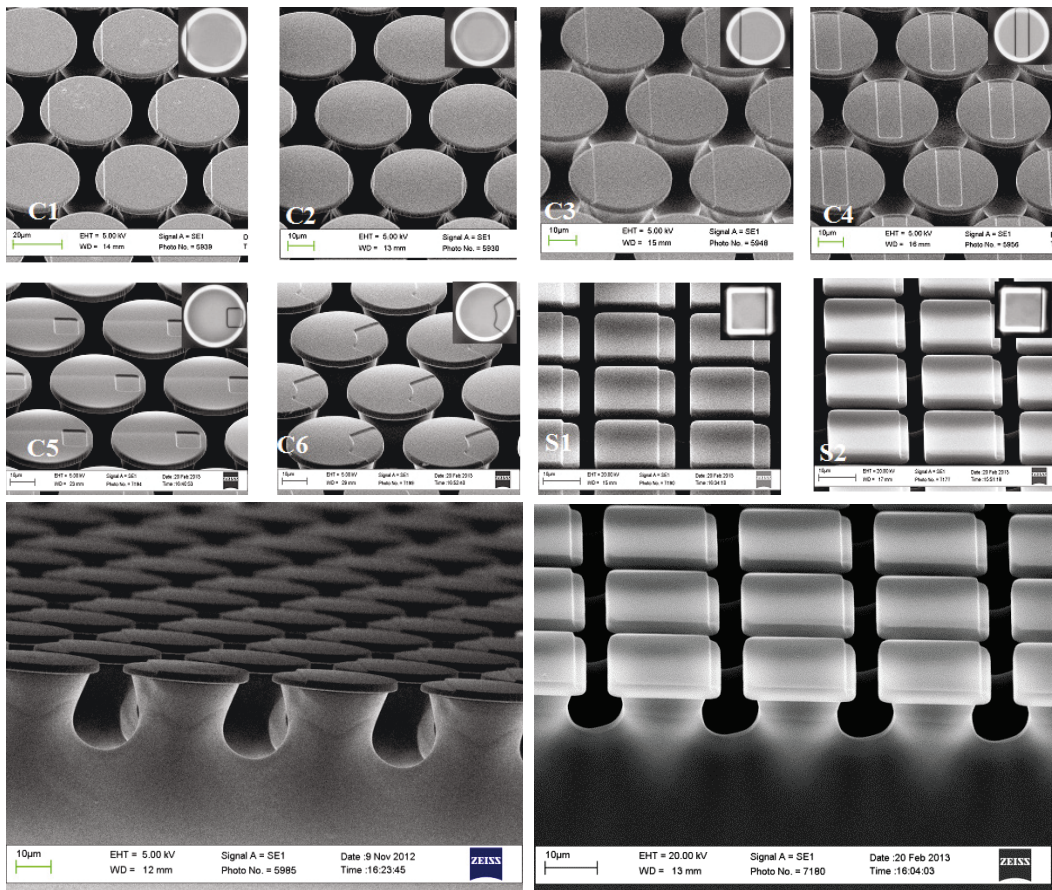
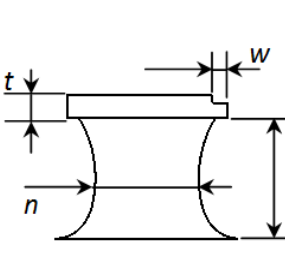


Figure 3.2: SEM images of the eight anisotropic adhesive samples of W1 mold consisting of fibers with circular and square caps and different defect shapes or sizes. C1 – C4 and S1 - S2 has bar shaped defects. C5 and C6 has square and toroid shaped defects respectively. Inset shows the microscopic top views. The last two images show the array of C3 and S1 fibers from the side. The image is published by the author in [65] and is reprinted with permission.

Table 3.1: Dimensions of the different anisotropic adhesive versions of W1 mold as obtained from the SEM images and Labview Vision software. The table is published by the author in [65] and is reprinted with permission.

Sample	C1	C2	C3	C4	C5	C6	S1	S2
Defect width, w (μm)	3.7	1.7	9.5	9.6	9.1	10.8	4.5	2.6
Defect location	Edge	Edges	Edge	Center	Close to the edge	Edge	Edge	Edge



$h \sim 22.8\mu\text{m}$ for C-series and $\sim 17.1\mu\text{m}$ for S-series;
 $t \sim 2.8\mu\text{m}$;
 $n \sim 27.6\mu\text{m}$ for C series and $\sim 14.9\mu\text{m}$ for S-series;
 Defect height ~ 800 nm

3.2 Fabrication of W2 adhesives:

A second mold (labeled W2) was fabricated using the same recipe but with a new set of masks in order to investigate the findings from W1 in more detail. Mold W2 consisted primarily of five samples of circular cap fibers and one sample of square cap fibers. The circular cap fibers had $40\mu\text{m}$ diameter caps and the square cap fiber had caps of $40\mu\text{m}$ edge length. Amongst the five circular cap samples, four of them had a square array arrangement of fibers ($C_{1x} - C_{4x}$) and one had hexagonal arrangement with the same pitch (C_{5x}). Details of different sub-samples from mold W2 are illustrated in **Table 3.2** to **Table 3.4** and **Figure 3.3**. Circular fibers with hexagonal arrangements (C_5) were stubbier ($\sim 19 \mu\text{m}$ height and $\sim 35 \mu\text{m}$ neck diameter) compared to those with square arrangements ($C_1, C_3 C_4$) ($20\text{-}23 \mu\text{m}$ height and $29\text{-}32 \mu\text{m}$ neck diameter). C_2 fibers, even though subjected to the same exposure and development conditions as the rest, were even taller and more slender ($\sim 29 \mu\text{m}$ height and $\sim 22 \mu\text{m}$ neck diameter), which

could be a result of diffraction of DUV light caused by the dotted pillars on the defects. The square fibers were $\sim 20 \mu\text{m}$ tall with $\sim 30 \mu\text{m}$ neck diameter. Bigger caps and predominantly square arrays of fibers (in W2) were fabricated in the mold to allow for easier alignment, something which was significantly more difficult to do with small fibers and hexagonal arrays (in mold W1). The different defect shapes and sizes were tested to determine the best shape and size which would be small enough to produce anisotropic behavior but would not collapse and lose directionality under larger preloads, especially with softer materials.

Table 3.2: Illustration of the defect size and position for C_1 samples

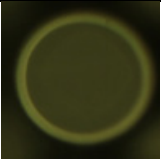
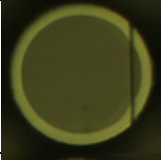
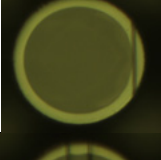
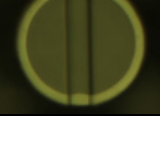
Sample name		Sample picture	Defect Size (μm)
Primary	Secondary		
C_1	C_{11}		No defect
	C_{12}		5.97
	C_{13}		3.5
	C_{14}		7.18

Table 3.3: Illustration of the defect size and position for C₂ and C₃ samples


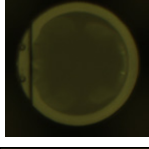
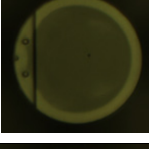

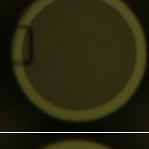
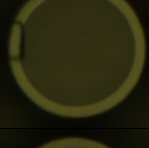
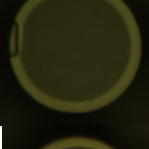

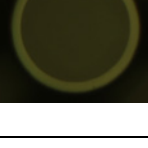







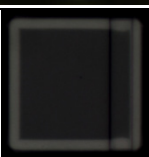

Sample name		Sample Picture	Defect Size
Original	New		
C ₂	C ₂₁		11.13
	C ₂₂		4.72
	C ₂₃		6.98
	C ₂₄		10.96μm
C ₃	C ₃₁		6.19
	C ₃₂		4.37
	C ₃₃		2.81
	C ₃₄		6.88
	C ₃₅		No defect

Table 3.4: Illustration of the defect size and position for C₄, C₅ and S₁ samples

Sample name		Sample picture	Defect Size
Original	New		
C ₄	C ₄₁		No defect
	C ₄₂		10.02
C ₅	C ₅₁		2.25
	C ₅₂		3.77
	C ₅₃		6.51
	C ₅₄		6.86
	C ₅₅		No defect
S ₁	S ₁₁		7.09
	S ₁₂		No defect

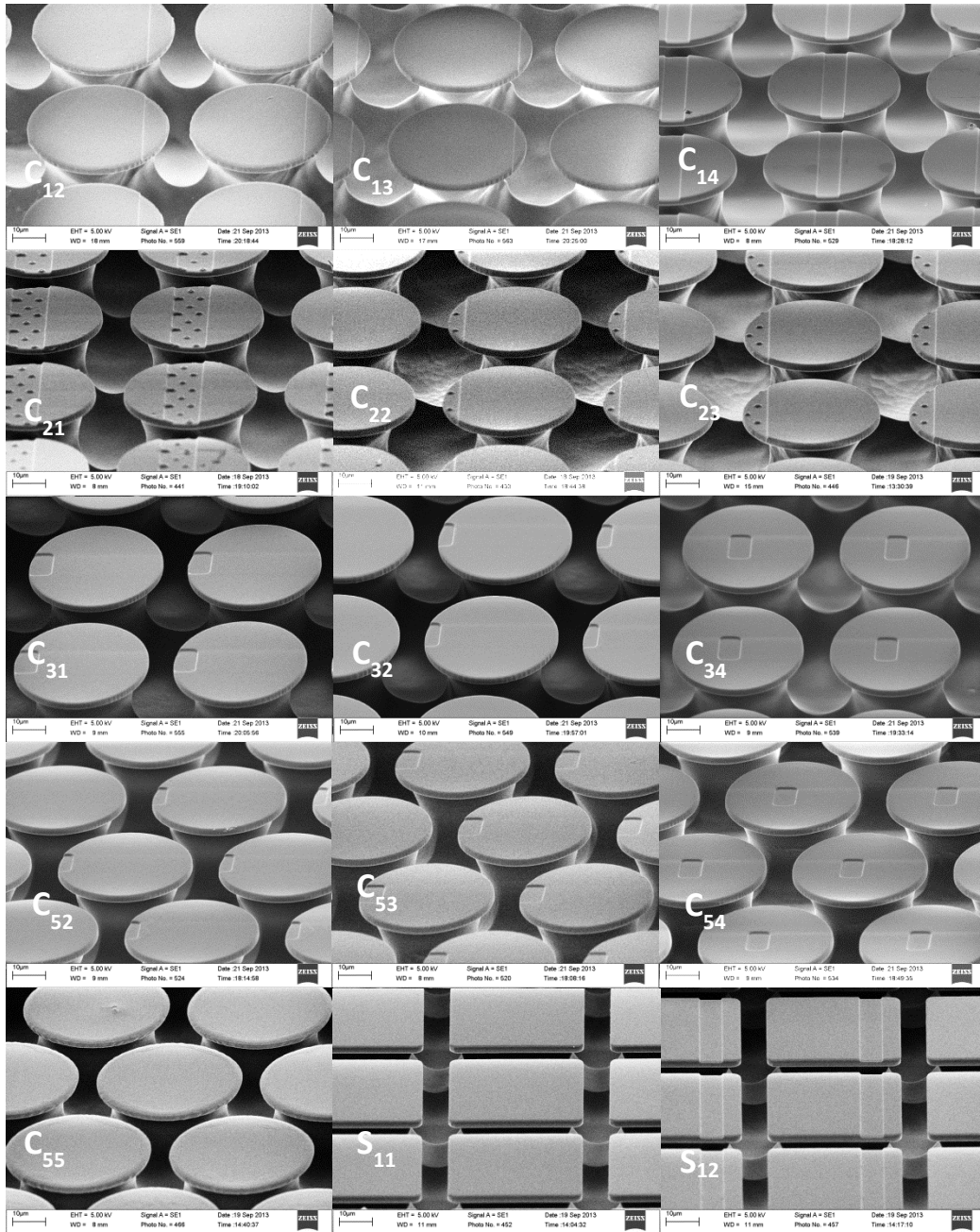


Figure 3.3: SEM images of the different adhesive samples from W2 mold demonstrating the three dimensional appearance of the fiber caps with deliberately produced defects.

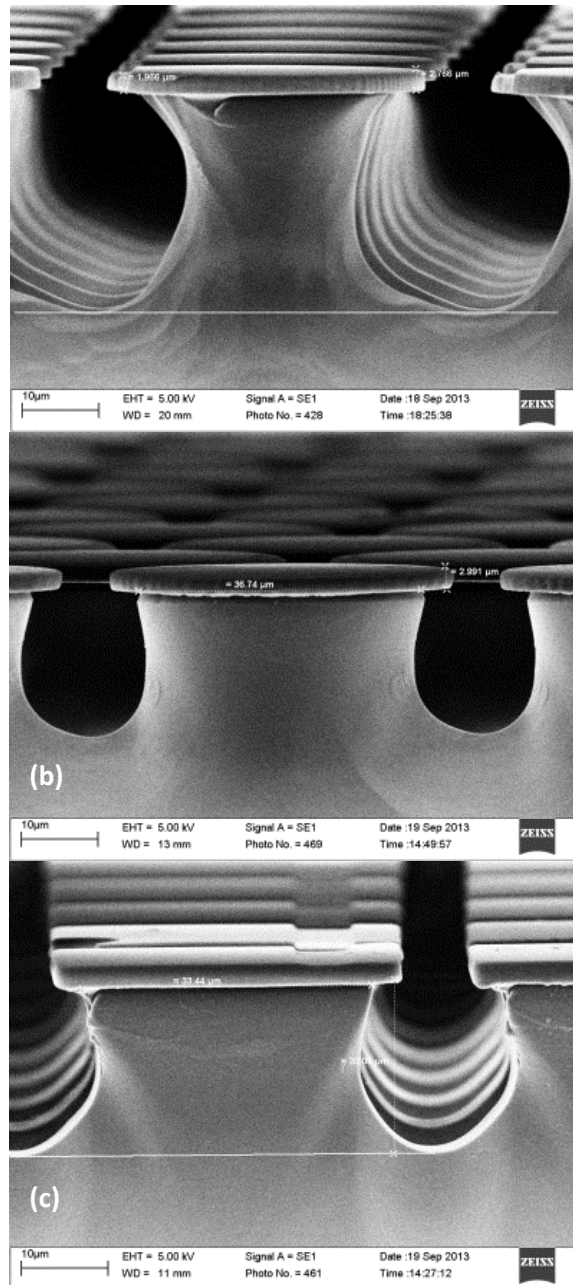


Figure 3.4: SEM images showing the relative fiber dimensions of the (a) square arrayed circular fibers, (b) hexagonal arrayed circular fibers and (c) square arrayed square fibers. Notice how the square arrayed circular fibers were relatively slender as compared to the other two arrangements even though all of them were subject to the same exposure doses and development time. The square array of circular caps during the DUV exposure step of fabrication would allow more light to pass between the caps as compared to the square array of square caps and the hexagonal array of circular caps, resulting in more undercut for the square arrayed fibers with circular caps.

3.3. Fabrication of Hot-embossed anisotropic adhesive:

In order to avoid the run-off error caused by the substrate warping of PMMA, the large scale version of the anisotropic adhesive was fabricated using a hot-embossing technique as outlined in **Figure 3.5** and elaborated as follows.

A 4.5 μm thick layer of SU-8 2005 was spun on a 4 in² clean borofloat glass substrate and prebaked at 90°C for 5 minutes, followed by exposure to 160 mJ/cm² dose of 356nm UV through a mask to produce arrays of square and circular caps upon development in SU-8 developer. The square and circular caps had 40 μm edge length and diameters respectively. A thin layer of HPR 504 was then spun on the SU-8 caps and exposed to 32.7 mW/cm² of 356 nm UV light through a second mask to define the defect shapes on the SU-8 caps, followed by development. Defects approximately 800nm deep were introduced on the caps in the form of indents by reactive ion etching for 3 min with the following settings: 100 sccm of O₂ and 5 sccm of CF₄, 150 W RF power and 125 millitorr chamber pressure. Any residual HPR 504 was removed by blanket exposing to UV and soaking in developer, leaving an array of SU-8 caps on the glass substrate with edge defects, which was the primary mold. No significant run-off error was observed, thanks to the rigidity and flatness of the glass substrate.

A stamp was then created for the subsequent hot-embossing by silanizing the primary mold followed by PDMS (Sylgard 184, Dow Corning) casting and curing, the PDMS being produced by mixing the pre-polymer to catalyst in a 10:1 ratio. A teflon coated flat glass plate was used to make sure the PDMS stamp has uniform thickness.

The PDMS stamp was used in a hot embosser (Jenoptik, HEX02) to emboss the cap structures on a 4.5 μm layer of uncross-linked SU-8 on PMMA substrate. In the hot-

embosser chamber, the PMMA substrate with the un-crosslinked SU-8 was first heated to 65°C to soften the SU-8 and then the stamp was pressed for 5 minutes with 50kN force to emboss the stamp structures onto the softened SU-8. After the embossing, the substrate was cooled to room temperature and then blanket exposed to UV for cross-linking followed by post-exposure baking for 30 minutes at 90°C in a convection oven. This was followed by reactive ion etching for 15 minutes to etch down and leave only SU-8 caps on bare PMMA substrate. The etching parameters used in this case were as follows: 75 sccm of O₂, 59.5 sccm of CF₄, 150W RF power and 125 millitorr chamber pressure. Unfortunately, the RIE used had a very high incidence of micro-masking [71], which increased the surface roughness of the SU-8 significantly compared with the lithographically defined caps. The micro-masking seemed to have been inherent to the RIE as it was present for a variety of etched materials and parameters, although the effect was not prominent in the earlier RIE step (**Figure 3.5d**) likely because of its short duration.

A negative mold was produced by casting TC 5030 silicone (BJB enterprise) which was later used to make the adhesive samples either by casting polyurethane or by using thermo-compression molding of thermoplastics, depending on the requirement. The thermo-compression molding technique is explained in section 5.3.

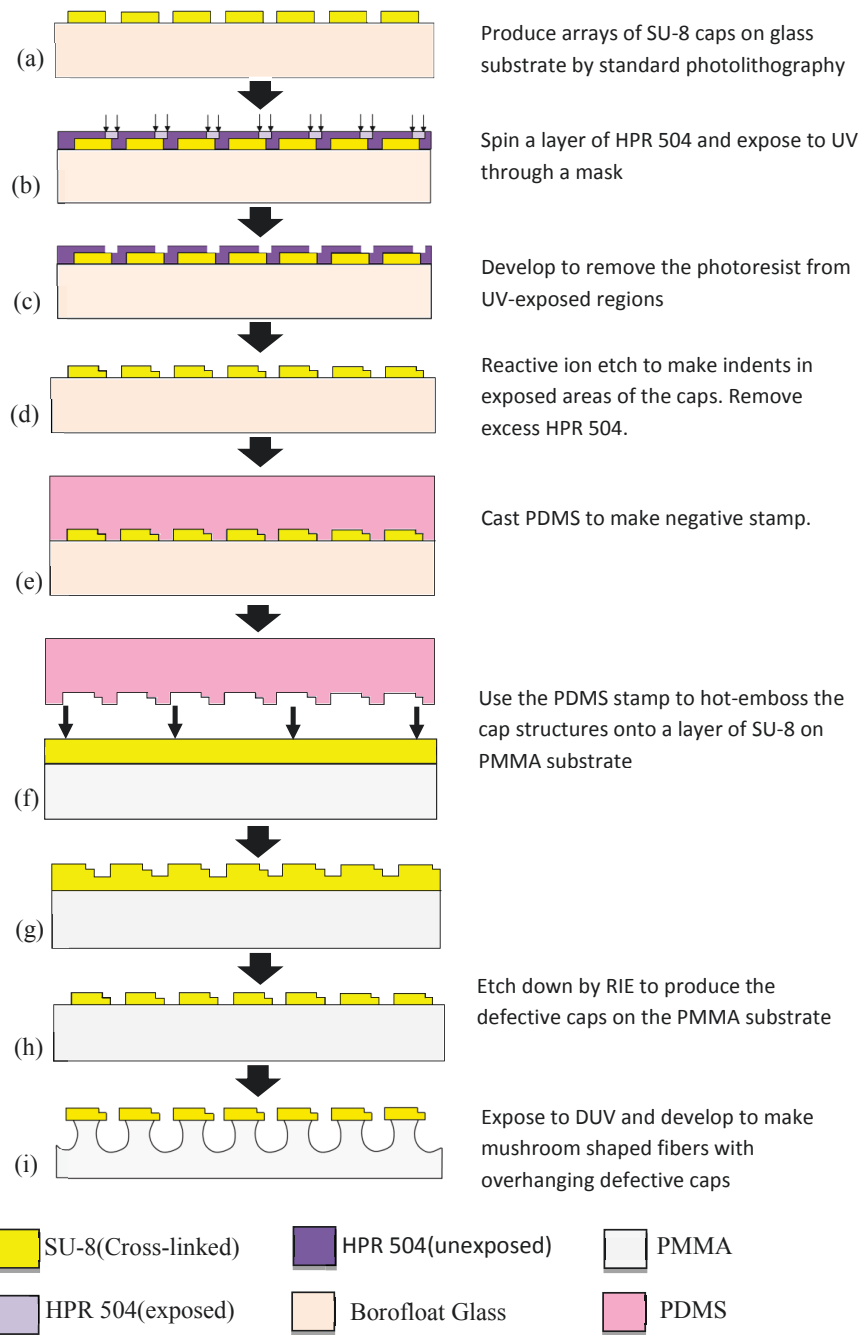


Figure 3.5: Schematics for the fabrication of the hot-embossed anisotropic adhesive mold.

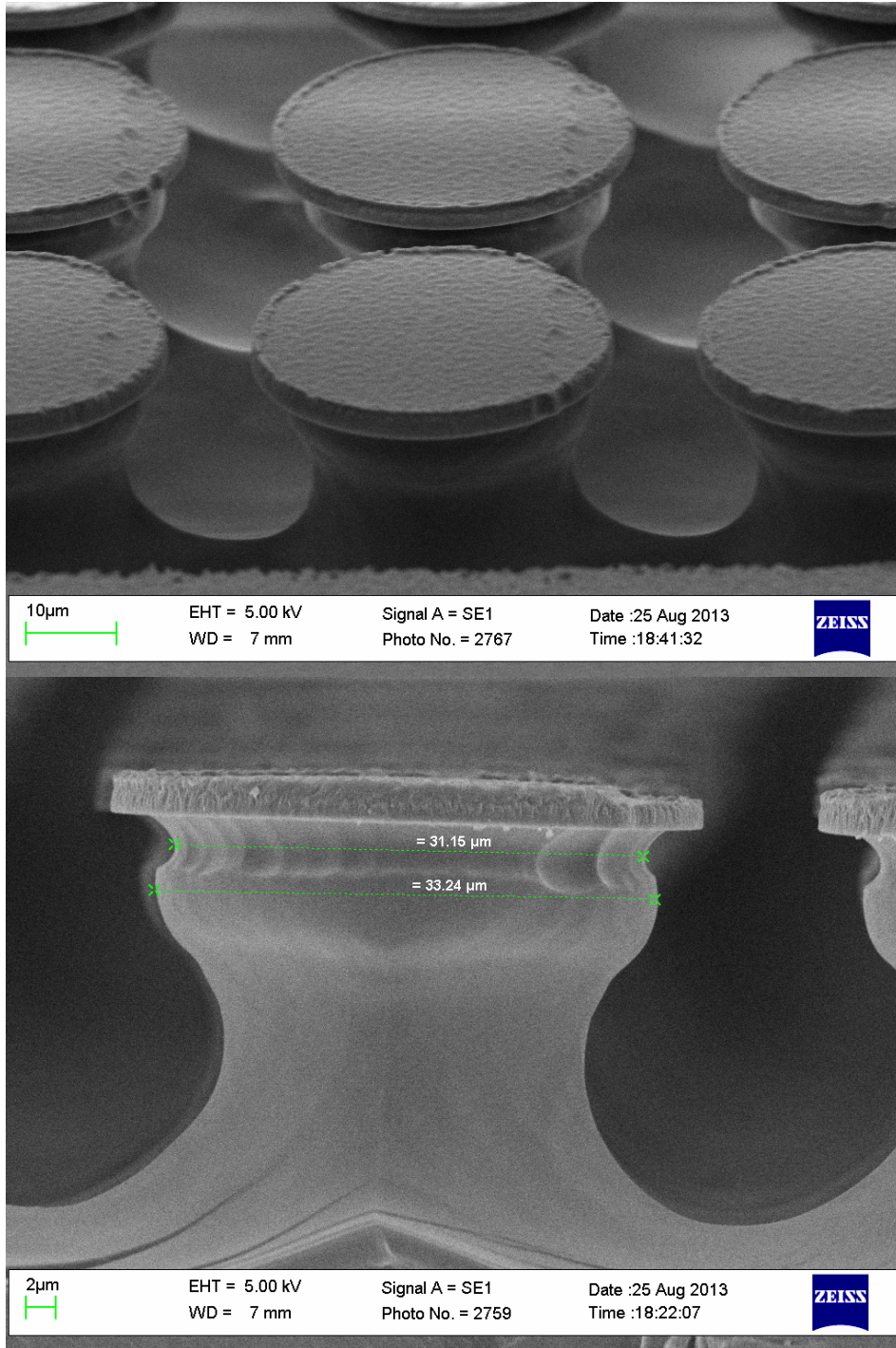


Figure 3.6: SEM images showing the hot-embossed W3 anisotropic adhesive samples. The roughness of the cap surface is a result of the micro-masking effect during the last reactive ion etching step.

3.4. Fabrication of the carbon black composite by compression molding:

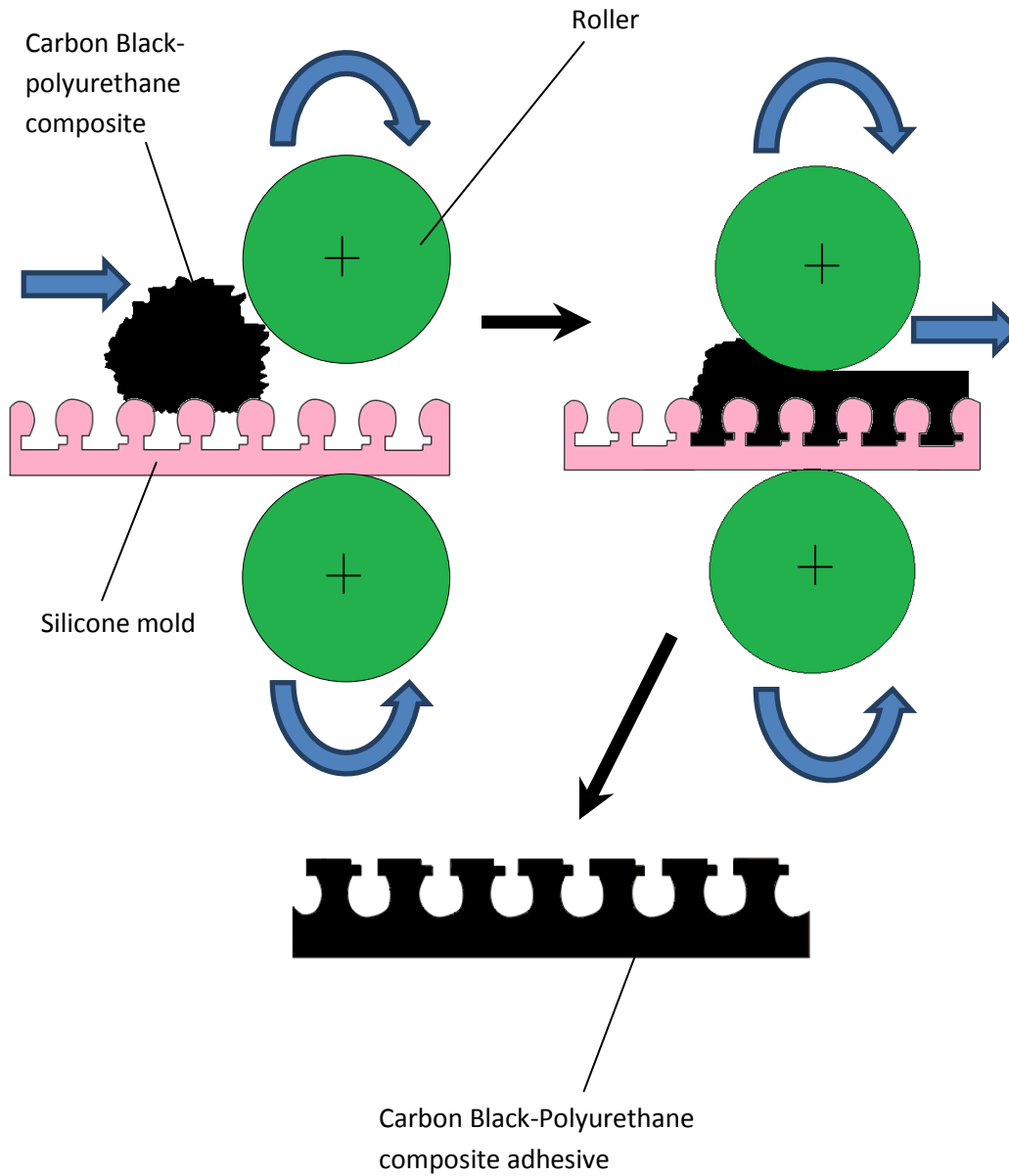


Figure 3.7: Schematics showing the fabrication of the Carbon Black-Polyurethane composite

Polymers, which are generally used to manufacture the dry adhesives, are poor conductors of electricity. This sometimes produces tribocharging, which is a phenomena of static charge build up or transfer due to contact or rubbing of two materials. The development of static charge is of concern in certain applications of dry adhesives, such as MEMS pick-and place [58] as sudden discharge could damage sensitive devices. To address this issue, carbon black fillers were added to polyurethane base to make a composite which is electrically conductive.

Figure 3.7 shows the compression molding of Carbon Black-Polyurethane composite to make the composite adhesives. The composite was created by mixing ST-1060 antistatic polyurethane and the required amount of Carbon black particles (CABOT, Vulcan XC72R, particle size ~50 nm). The ST-1060 antistatic was prepared by mixing the pre-polymer to catalyst in a 2:1 ratio. The carbon black particles were weighed separately in a glove box and then added to the polyurethane in steps, followed by stirring by hand each time. To make the adhesive, a thick drop of uncured composite mixture was poured on a silicone mold, as shown in **Figure 3.8**. The mold was placed on a rigid plastic sheet and put inside a zip-lock bag and then passed through the rollers of a laminator to squeeze the composite material into the mold recesses. The gap between the rollers could be adjusted, depending on the required thickness of the backing layer. The composite adhesive was then cured for a day in room temperature followed by at least 8hrs at 80°C in an oven. In order to demold the adhesives, pure ST-1060-antisatic was cast on top of the carbon black adhesive and then cured before demolding, which embedded the composite adhesive in it, as shown in **Figure 3.9**.

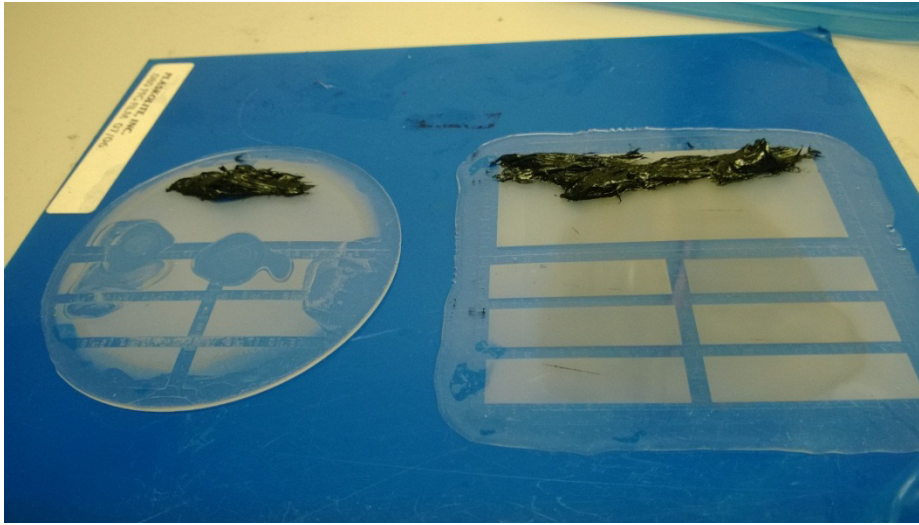


Figure 3.8: Uncured viscous composite molds before passing through the rollers



Figure 3.9: Adhesives made out of composite materials. Picture on the left has the composite adhesive portion embedded in plain polyurethane. Picture on the right shows a composite adhesive sample attached to a rigid backing of acrylic.

Five different samples of the carbon black composite were made with the carbon black weight percentages of 8, 10, 12, 14 and 16%. In addition to the adhesives, rectangular pucks were also prepared to measure the electrical resistivity of each of the samples.

3.5. Adhesion Testing:

The normal adhesion force of the samples was determined by a load drag pull test (LDP) [30] [34] [36] using a custom test system described in detail in [37][61]. The testing process is shown schematically in **Figure 3.10(a)**. The system, as shown in **Figure 3.10(b)**, has a tension/compression load cell (GSO-25, Transducer Techniques) attached to a linear stage (Newport MFA-CC) and connected to a computer via a DAQ. A 6 mm diameter sapphire hemispherical indenter (Edmund Optics NT49-556) is attached to the sensing unit of the load cell. The operation and data acquisition of the testing system is carried out using custom software written in LabVIEW.

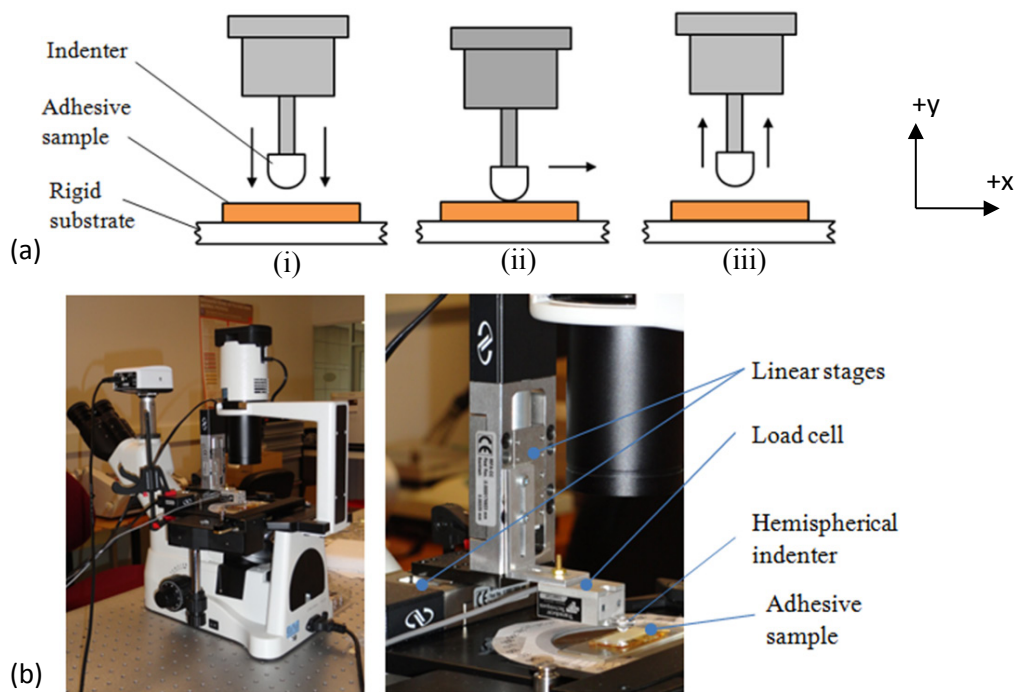


Figure 3.10: (a) Schematic of the adhesion testing process showing (i) Preloading; (ii) Shear displacement in a direction perpendicular to the edge of the defect; and (iii) Pulling-off. (b) The adhesion testing system consisting of two linear stages for two-axis motion, a load cell and a hemispherical indenter. The picture on the right is a zoomed-in view showing the components of the testing system in details. The image is published by the author in [65] and is reprinted with permission.

All velocities of the test system are kept constant at 5 $\mu\text{m/s}$, and the indenter is left in contact with the sample for 3 seconds prior to the application of shear displacement. Shear displacements of -25 μm , -18 μm , -11 μm , -5 μm , 0 μm , 5 μm , 10 μm , 15 μm , 20 μm and 25 μm were applied (these were found to provide more information in the range of greatest shear sensitivity for most adhesives) for an average preload of 1 mN in separate trials. Images of the fibers in contact were recorded to estimate the contact area for these preloads. A circular area of approximately 300 μm in diameter was found for a typical preload. The average temperature and relative humidity in the lab during the trials was 20 $^{\circ}\text{C}$ and 43% respectively.

In summary, this chapter discusses how an existing process to make isotropic adhesive fibers can be modified slightly to render the fibers anisotropic and the challenges associated with this process modification. Also shown in this chapter is the fabrication process to make conductive versions of the adhesives using carbon black-polyurethane composite. The instrumentation and methodology of adhesion testing is described, the result of which is presented in the next chapter.

4. Adhesion characteristics of the polyurethane anisotropic adhesives³

In this chapter, the results of finite element analysis (FEA) on mushroom shaped isotropic/anisotropic fibers are presented to verify the analytical studies in chapter 2. Adhesion test results are also presented to investigate the hypothesis, presented in chapter 2, and the findings from the finite element modeling.

The first sets of anisotropic adhesive were prepared using ST-1060 polyurethane from W1 mold, as outlined in section 3.1. Six adhesive samples with circular caps (36 μm diameter) (C1 –C6) and two adhesive samples with square caps (24 μm edge length) (S1, S2) were initially fabricated. As depicted in **Figure 3.2**, samples C1 to C4 had bar-like defects of different size and positions. Samples C5 and C6 had rectangular and toroid shaped defects respectively. S1 and S2 had bar-like defects of different sizes. Section 3.1 discusses the normal adhesion test results of the W1 polyurethane adhesives in more detail.

Based on the results of the W1 adhesives, a second mold, W2, was designed and fabricated to address the issue of defect size and shapes in more detail and also to allow for a larger scale production of the circular caps with bar-like defects. Refer to section 3.2 for details on the geometry of W2 adhesive samples. Adhesion test results of W2 polyurethane adhesives are presented in section 4.2.

³ Sections of this chapter are published by the author in [65] and [127] and are reproduced from the original articles.

4.1. Finite element analysis of fibers with defective cap

Finite element analysis was carried out using COMSOL 4.3 for a qualitative demonstration of the tensile stress on the fiber and cap when loaded in an axial direction and the redistribution of stress when the tensile load on the fiber is coupled with shear displacement of the cap. The mushroom shaped fiber model was based on SEM measurements of circular fiber fabricated for this work (C1 and C3 from W1 mold). The fibers are 25.6 μm tall with a 3 μm cap overhang. The defect depth was 800 nm for all the three cases shown in **Figure 4.1** while the defect width was 3.7 μm for **Figure 4.1(a)** and **Figure 4.1(c)**, and 9.5 μm for **Figure 4.1(b)**. The cap surface was held in a fixed boundary condition while the displacements were applied to the bottom of the 100 μm backing layer. The fibers in **Figure 4.1(a)** and **Figure 4.1(b)** were only subject to tensile load by means of a vertical displacement of 10 μm , whereas the fiber in **Figure 4.1(c)** was subjected to a 10 μm shear displacement away from the defect in addition to 10 μm vertically.

Since the polyurethane used for manufacturing the fibers is a hyper-elastic material, and to account for the possibility of large deformations as seen in previous reports [45], a hyper-elastic solid mechanics model is necessary to better approximate the stress conditions in the fiber.

Consequently, the analysis was carried out using Mooney-Rivlin hyper-elastic model where the strain energy density function is a linear combination of two invariants of the left Cauchy-Green deformation tensor [72]. The strain energy density function for an incompressible Mooney-Rivlin material is given by [72] [73]:

$$U = C_{10} (\bar{I}_1 - 3) + C_{01} (\bar{I}_2 - 3) \quad (18)$$

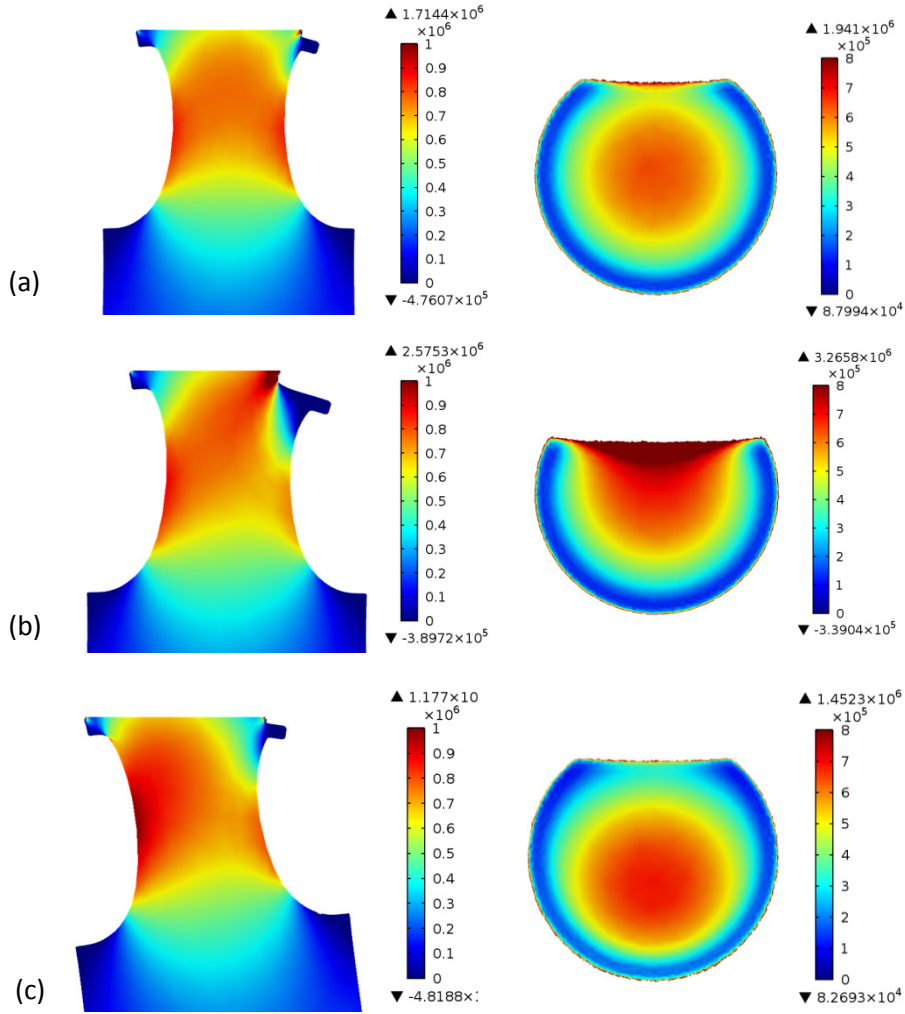


Figure 4.1: Sectional views showing the distribution of First-Piola Kirchhoff stress normal to the cap for a fiber with defective cap in fixed contact with a flat substrate. The fibers are pulled $10\ \mu\text{m}$ in the normal direction with the addition of $10\ \mu\text{m}$ shear displacement for (c). (a) and (c) corresponds to C1 (Figure 3.2) with $3.7\ \mu\text{m}$ defect width; (b) corresponds to C3 (Figure 3.2) with $9.5\ \mu\text{m}$ defect width. It is obvious from figure (a) that the application of tensile load induces a stress concentration at the defect edge which is reduced when the cap is sheared away from the defect(c). Increasing the defect size to $9.5\ \mu\text{m}$ builds up the stress at the defect edge by more than 50 %, as evident in (b). The image is published by the author in [65] and is reprinted with permission.

where C_{10} and C_{01} are empirically determined material constants, reported to be 330 kPa and 360 kPa respectively for ST-1060 polyurethane by Bscheiden et al. [74], \bar{I}_1 and \bar{I}_2 are the first and second invariants of the deviatoric component of the left Cauchy-Green

deformation tensor respectively. Other hyper-elastic material models [73] can also be used if the necessary material constants are known.

The finite element analysis shows that the tensile stress on these fibers is highest towards the center of the fiber when loaded axially (**Figure 4.1a**), but a non-overhanging edge can concentrate forces and initiate peeling. This relatively non-uniform stress distribution in the top surface (even without considering the overhanging cap) is primarily a consequence of the low aspect ratio fiber (fiber height: diameter ≤ 1), and the tapered hour-glass form of the supporting fiber. Probing the stress at the surface of C1, **Figure 4.1(a)** reveals that the stress at the edge of the defect is approximately 1.62 MPa. At the same distance ($\sim 14 \mu\text{m}$) on the opposite side of the cap, the stress was found to be approximately 308 kPa, which shows that the presence of the defect at the cap edge increased the stress level more than 500 % over the normal stress at the same radius. With a larger defect, the edge is closer to the high stress zone at the center. This increases the stress intensity at the defect edge of C3 as shown in **Figure 4.1(b)** with 3.1 MPa vs. 554 kPa for 8.09 μm radius at a defect and non-defect respectively. When a shear displacement is applied on C1 away from the defect, the stress on the cap is redistributed and the central high stress zone shifts away from the defect, thus reducing the stress intensity at the defect edge, as shown in **Figure 4.1(c)** (1.26 MPa vs. 413 kPa). The ratio of stress at the defect edge to that at the other side of the cap decreased to approximately 305 % for this case. Similarly, if the shear displacement is in the opposite direction, the high stress zone would shift towards the defect, making the stress concentration at the edge more pronounced. The practical implication is that for any given fracture strength or work of adhesion, the addition of an offset defect can result in significant adhesion anisotropy.

Stress singularities can be seen at the periphery of the cap because of the sticking friction [64][75][76](modeled as a fixed boundary) imposed on the cap surface, which can also be seen in the finite element analysis of mushroom shaped fibers by Spuskanyuk et al. [64] . These singularities are probably not present in reality as the cap surface is free to slide against the conforming surface and/or allowed to expand or shrink as a result of the tensile and shear load on the fiber. The finite element modeling is only meant to provide a general qualitative understanding of the stress distribution on the fiber and cap as a result of the loading.

4.2 Adhesion test result of W1 polyurethane adhesives:

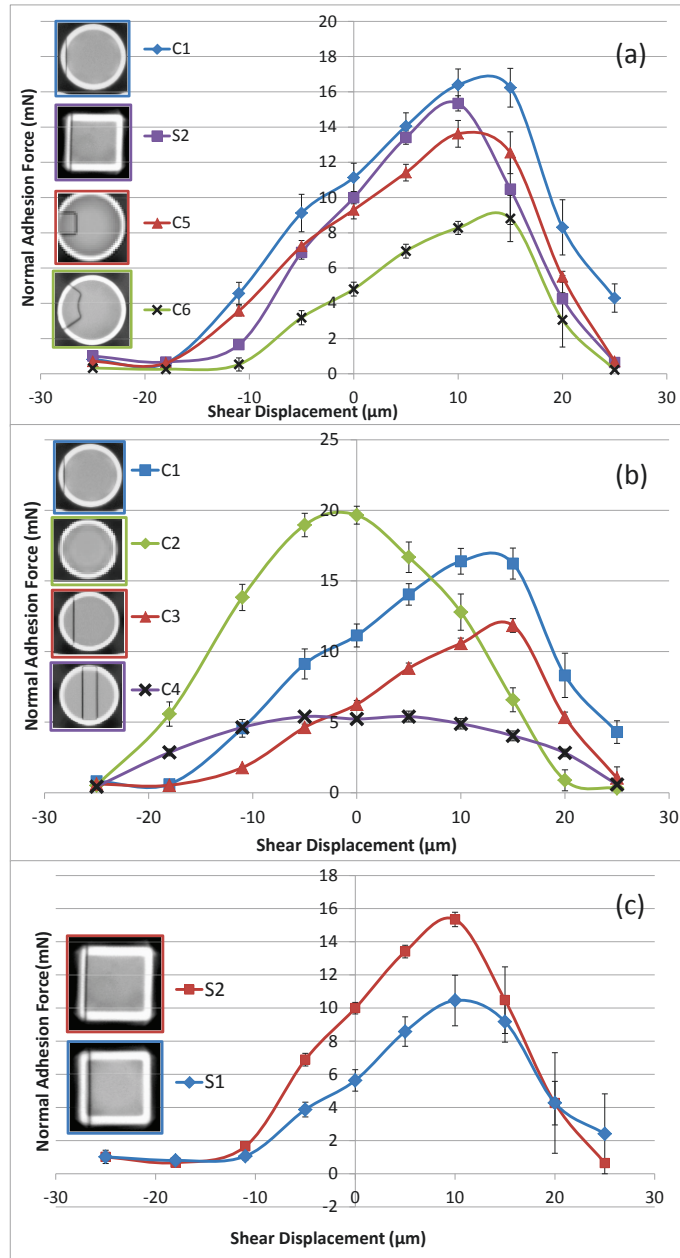


Figure 4.2: Plots of normal adhesion force against shear displacement for adhesive fibers with: (a) Square and circular caps with different defect shapes; (b) Circular caps with bar like defects of different sizes and locations; (c) Square caps with bar like defects of different sizes. C1 and S2, having small bar-like defects at the edge demonstrated the highest anisotropic adhesion. C6, with the torrid defect, demonstrated the least adhesion. The image is published by the author in [65] and is reprinted with permission.

Figure 4.2(a) is a comparison of plots of adhesion force against shear displacement of four different adhesive samples corresponding to four different cap-defect configurations as shown in the insets. The non-symmetrical nature of the graphs proves the fact that the presence of offset defects on the caps induces directionality of adhesion. The fibers with circular caps and bar like defects at an edge (C1) had the highest maximum normal adhesion force of the directional designs as compared to the others in these trials, trailed closely by the fibers with square caps with a similar small defect at an edge (S2). The superior adhesion performance of C1 and S2 as compared to C3, C5 and C6 can be attributed to the positioning and size of the defect. In both C1 and S2, the defect size was small and further away from the high stress zone (the red zone in **Figure 4.1**) as compared to those of C5 and C6 whose defects were much larger and closer to central high stress zone. The larger the defect size, the smaller the total contact area of the cap to the adhering substrate, and thus the adhesion force is lower. Furthermore, being closer to the high stress zone, the stress concentration at the defect edge grows more rapidly during pull-off, as a result of which the crack would form more readily, causing easier detachment.

The adhesion force plot in **Figure 4.2(b)** and **Figure 4.2(c)** serves to verify this explanation, as it demonstrates the effect of size and location of the bar-like defects on circular and square caps respectively on the adhesion force of the fibers. The maximum adhesion force dropped from 16.4 mN in C1 to around 11.8 mN in C3 when the defect size was increased from 3.7 μm to 9.5 μm respectively. Similarly, the maximum adhesion force dropped from 15.3 mN in S2 to 10.5 mN in S1 when the defect size was increased from 2.6 μm to 4.5 μm .

Also, the plot in **Figure 4.2(b)** shows that the small symmetric defects on the overhanging portion of the caps of C2 results in isotropic adhesion, with a maximum adhesion force of 19.7 mN, exceeding that of our best performing anisotropic adhesive, C1. Being even further from the central high stress zone coupled with the tiny size of the defects, the compressive force at the overhanging portion of the cap as a consequence of the tensile loading of the fiber (**Figure 4.1**) was significant enough to prevent the cracks from these tiny defects from propagating, as suggested in earlier reports of Spuskanyuk et al. [64] and Carbone et al. [62] resulting in strong, isotropic adhesion. On the other hand, poor, isotropic adhesion was observed when a relatively large defect was placed at the center of the fibers, C4 (**Figure 4.2b**). The central region of the cap is the most sensitive to defects since it forms the region of high stress upon loading. With a non-defective cap of the mushroom shaped fibers, the crack usually nucleates at the center and propagates outwards [63]. The presence of a large defect at the center of the cap only exacerbates the adhesion loss, resulting in rapid crack formation and propagation until contact is lost. Of note, when the maximum stress at the crack in **Figure 4.1(a)** and **Figure 4.1(b)** is compared to the normal adhesion force of C1 and C3 respectively in the absence of shear, a similar ratio is obtained ($1.62 \text{ MPa}/3.1 \text{ MPa} = 0.52$, $6 \text{ mN}/11 \text{ mN} = 0.54$). Thus, if the crack experiences half the stress for a given axial displacement, and if the work of adhesion between the surfaces is a constant, then the fiber should be able to support double the load before failure. This indicates that despite the unknown absolute work of adhesion between the polyurethane and the indenter tip, or the specific boundary conditions that include slip, the FEM model can predict relative performance of different designs fairly well. The performance of C3, C5 and C6, which all have similar crack lengths (9.5, 9.1 and 10.8 μm respectively) have very

different normal adhesion forces at zero shear ($\sim 6, 9$ and 5 mN respectively). This difference is too large to account for by the simple equation of crack length dependence in equation (17), but can be partially addressed by the reduction of total cap area. Additionally, the perimeter of the defects may also have a strong influence on the likelihood of initial failure, as slight misalignment of shear direction could make a big difference in design C5 (with a notch defect), but C6 (with a toroid defect) would have early failures at a broader range of shear displacement directions. If control over exact displacements is very good (in robotic pick and place for example), then defects similar to, but smaller than, C5 could be the best option to maximize the total anisotropy ratio.

These results are consistent with the linear beam theory example, which predicts that progressively larger shear displacements would be needed to apply a compressive load on a crack that extends in further from the edge of the fiber and fibers with larger cracks will have lower adhesion for any given shear displacement. In principle, theory shows that any defect of depth greater than 10 nm will exhibit negligible adhesion via van der Waals interactions and will act as a stress concentrator [77]. In practice however, we have found that if the defect is too shallow, larger preloads can force the recessed areas of the caps into contact with the other surface, and the anisotropic behavior is lost, making the performance of these materials less predictable. This practical limitation was discovered in early trials with thinner caps, and is not reported extensively in this work, but does pose a practical limitation to this technique. For the 800 nm depths introduced here, the majority of fibers remain with the defect out of contact until finally fiber buckling occurred with increased preloads.

When the adhesives are tested, the results show very good uniformity and long term durability. Tests on a single location of C1 adhesive were run 150 times with shear displacements of -18, 0 and 15 μm respectively for a total of 450 trials in a single location. Negligible reduction in performance was observed, as shown in **Figure 4.3**.

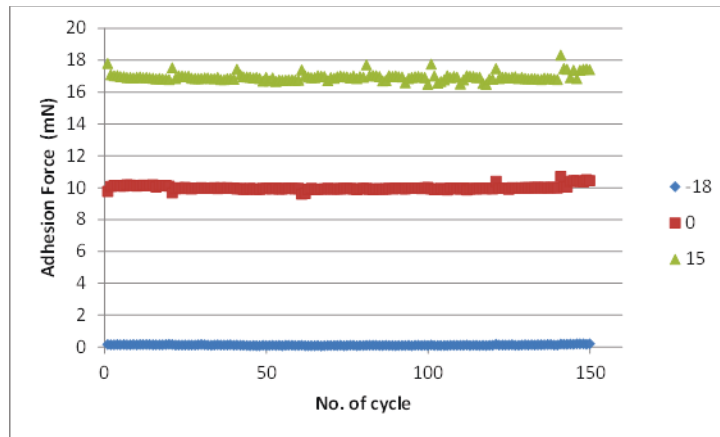


Figure 4.3: Load-drag-pull maximum adhesion force measurements in a single location for C1 adhesive designs. Drag distances are 15, 0 and -18 μm which correspond to maximum, neutral and minimum performance as seen in **Figure 4.2**. The image is published by the author in [65] and is reprinted with permission.

The maximum normal adhesion force for the sample C1 was found to be approximately 250 kPa (measured by the maximum adhesive force divided by the projected area of contact with the hemispherical indenter) with a preferential shear displacement. With the smallest adhesion force of approximately 5 kPa from the same sample, this gives an anisotropic adhesion ratio of around 50:1.

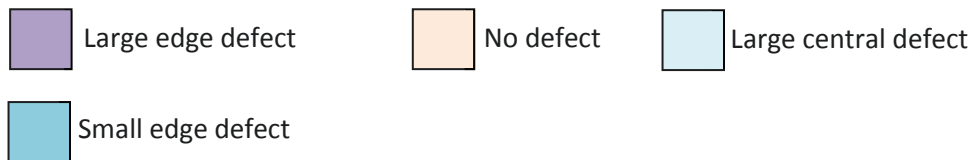
4.3 Adhesion test results of W2 adhesives:

Inspired by these findings on W1 adhesives, a second adhesive mold, W2, was designed and fabricated in order to investigate the effect of defect sizes on the adhesion force and anisotropy in a broader capacity and also to compare the adhesion forces of fibers with different arrangements and cap shapes corresponding to different defect shapes. The maximum adhesion forces of the 22 adhesive sub-samples of W2 are compiled in **Table 4.1**. To facilitate the comparison, a bar graph is added (**Figure 4.4**) in which fibers with similar defect conditions are grouped together.

Figure 4.5 and **Figure 4.6** corroborate what we found earlier with the W1 adhesives, i.e. the larger the defect size, the weaker the adhesion. Interestingly, it can be seen from **Figure 4.5(c)** that the adhesion of C_{33} is almost isotropic with a defect size of $2.8 \mu\text{m}$. The cap overhang being $\sim 4.6 \mu\text{m}$ for the square arrayed circular fibers; we can deduce that the defect width has to be approximately equal or larger than the cap overhang in order to induce anisotropic adhesion, otherwise the resultant compressive load on the overhanging portion of the cap due to tensile load on the fiber would be enough to suppress the defect and prevent the crack from propagating.

Table 4.1: Comparison of the maximum adhesion force of the different adhesive sub-samples with a nominal 1 mN preload

Sample	Defect Size (μm)	Defect location	Max Adhesion (mN)
C ₁₁	no defect	-	18.4
C ₁₂	5.97	edge	12.3
C ₁₃	3.5	edge	16.0
C ₁₄	7.18	middle	4.7
C ₂₁	11.13	middle	4.5
C ₂₂	4.72	edge	17.7
C ₂₃	6.98	edge	13.9
C ₂₄	10.96	edge	10.6
C ₃₁	6.19	edge	13.8
C ₃₂	4.374	edge	13.7
C ₃₃	2.81	edge	19.1
C ₃₄	6.88	middle	8.4
C ₃₅	no defect	-	18.8
C ₄₁	no defect	-	18.6
C ₄₂	10.02	edge	12.8
C ₅₁	2.25	edge	16.9
C ₅₂	3.77	edge	15.2
C ₅₃	6.51	edge	12.9
C ₅₄	6.86	middle	7.9
C ₅₅	no defect	-	17.9
S1 A1	7.09	edge	8.6
S1 A9	no defect	-	17.2



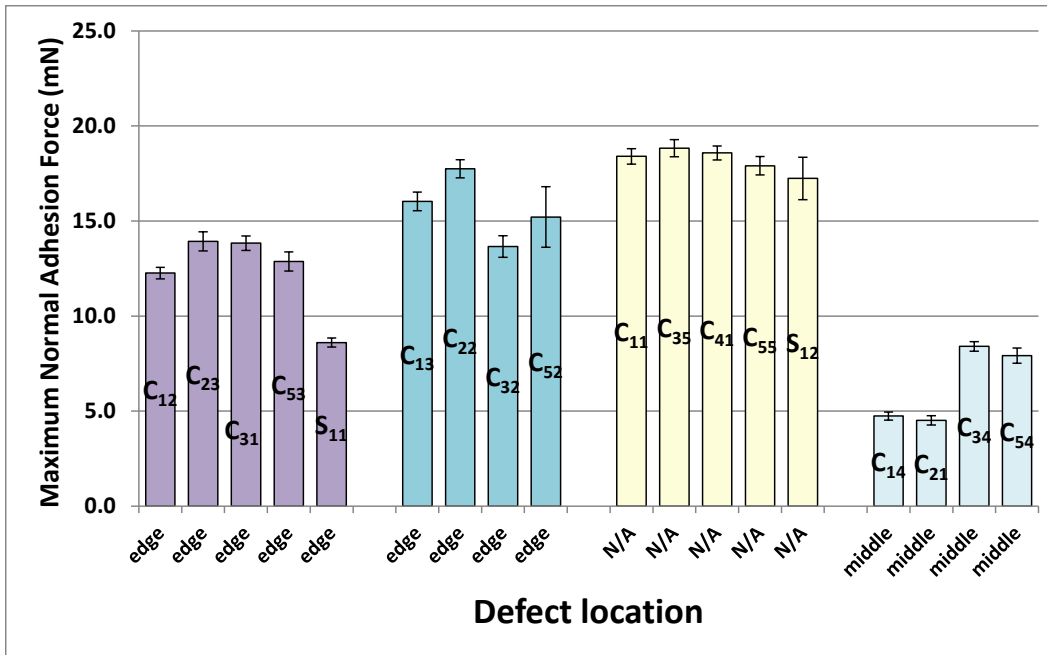


Figure 4.4: Bar graph comparing the maximum adhesion forces of fibers as mentioned in Table 5. Bars corresponding to fibers with similar defect sizes are grouped together. The coloring scheme is the same as in **Table 4.1**. Each sample was tested 9 times and the mean and standard deviation was calculated and plotted.

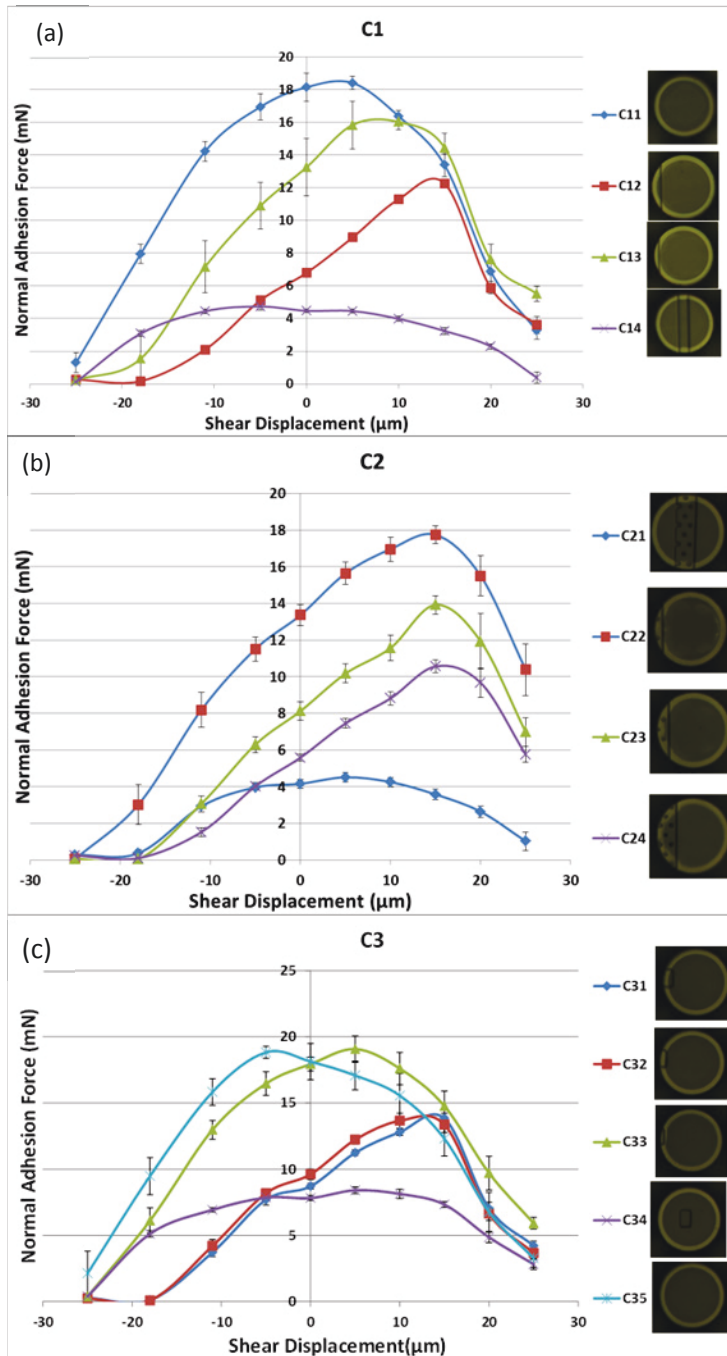


Figure 4.5: Plots of normal adhesion force vs shear displacement for samples with (a) bar-like defects; (b) bar with dimple defects and (c) rectangular defects. Inset shows defect shapes and relative size differences for each of the samples corresponding to the graphs

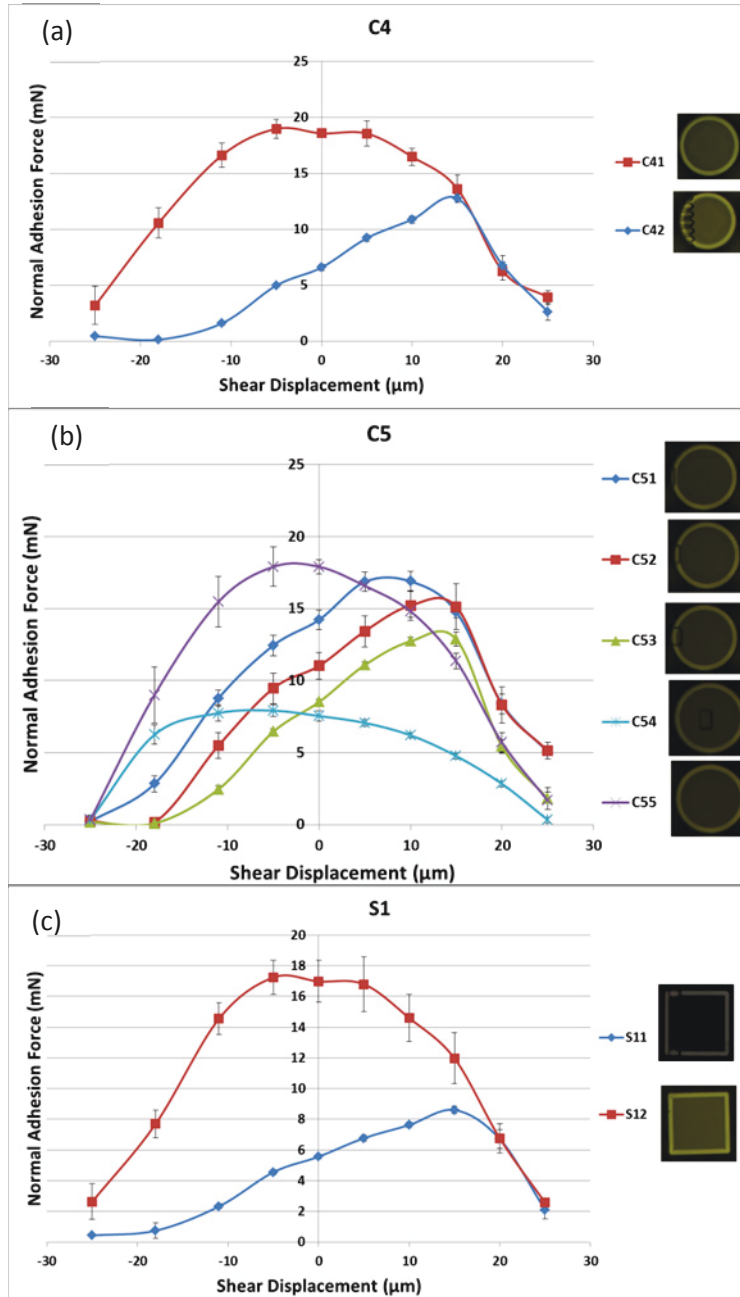


Figure 4.6: Plots of normal adhesion force vs shear displacement for samples with (a) finger-patterned defects; (b) rectangular defects and (c) bar-like defects. Inset shows defect shapes and relative size differences for each of the samples corresponding to the graphs. Please note that the C5 samples had hexagonal arrays of fibers with rectangular cap defects which is not to be confused with C3 samples which had square arrays of fibers with similar cap defects.

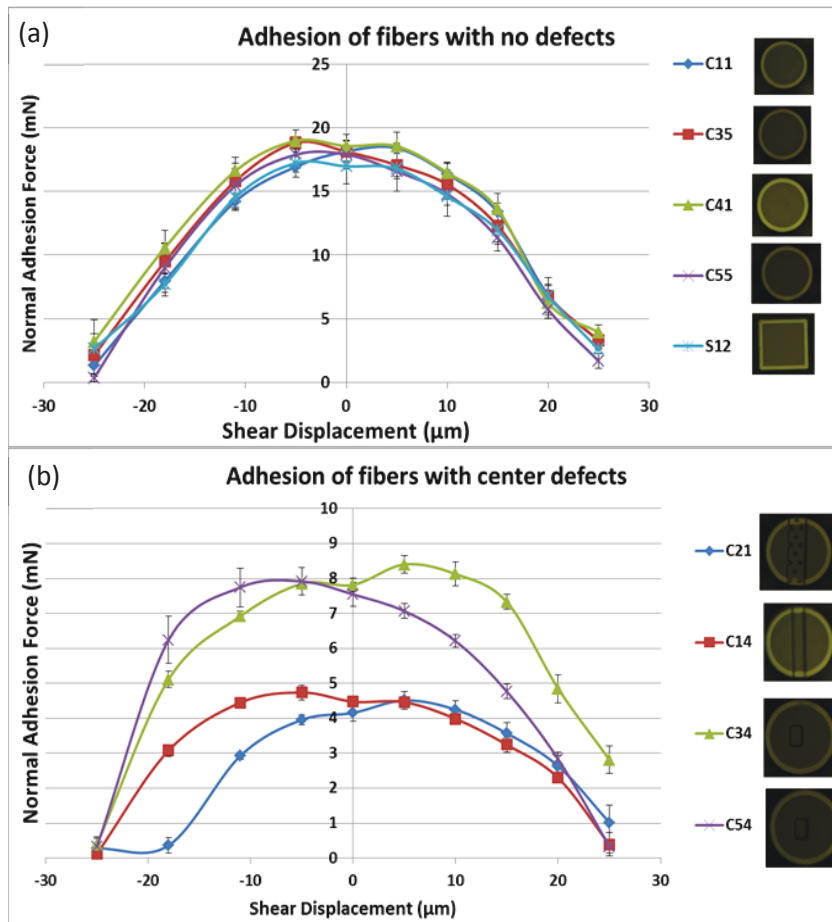


Figure 4.7: Comparison of adhesion forces for samples with (a) no cap defects; and (b) central cap defects.

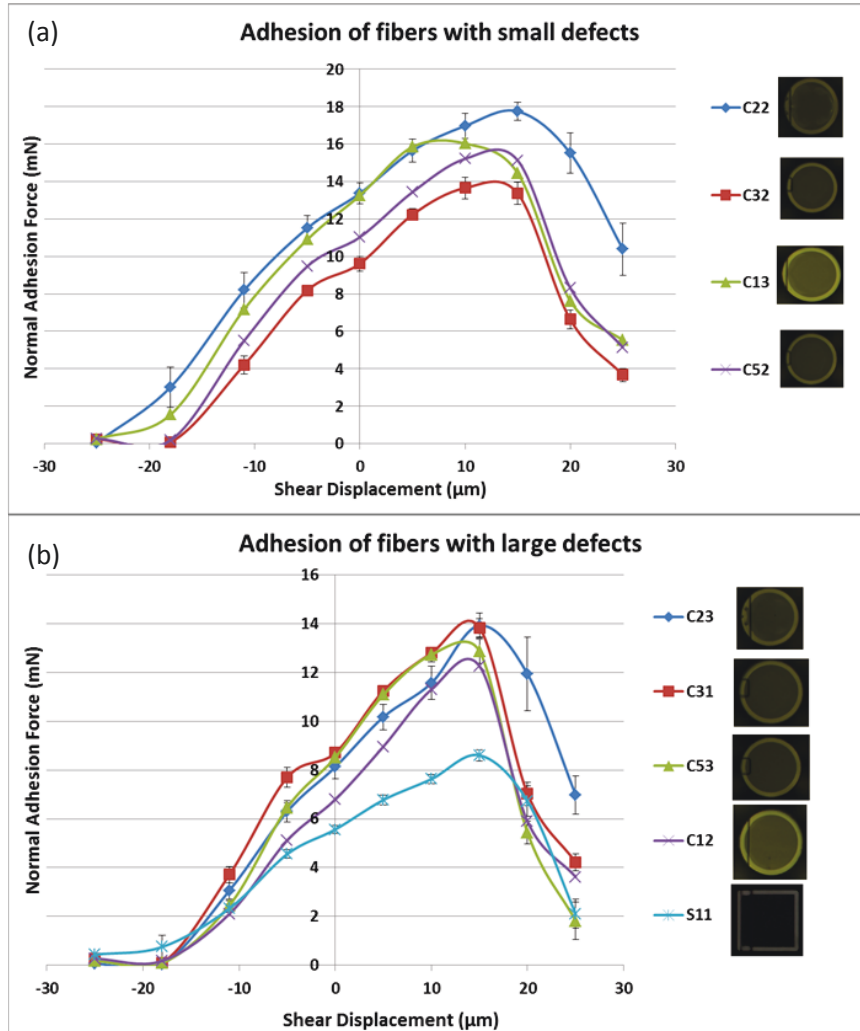


Figure 4.8: Comparison of adhesion forces for samples with (a) small defects of similar widths and (b) large defects of similar widths.

The non-defective fibers, shown in **Figure 4.7(a)**, demonstrated that the adhesives performed similarly, even though the fibers in C₅₅ and S₁₂ are lower in aspect ratio than the rest, with C₅₅ being lowest aspect ratio. Even though the center to center distance between the adjacent fiber caps for all the three configurations (square array of circular fibers, hexagonal array of circular fibers and square array of square fibers) are same (50 μm), the hexagonal packing of the circular caps would allow less uncollimated DUV to pass through between the caps during the fabrication step in **Figure 3.1(e)** as compared

to the square array arrangement of circular caps because of the relatively denser arrangement of the hexagonal pack.

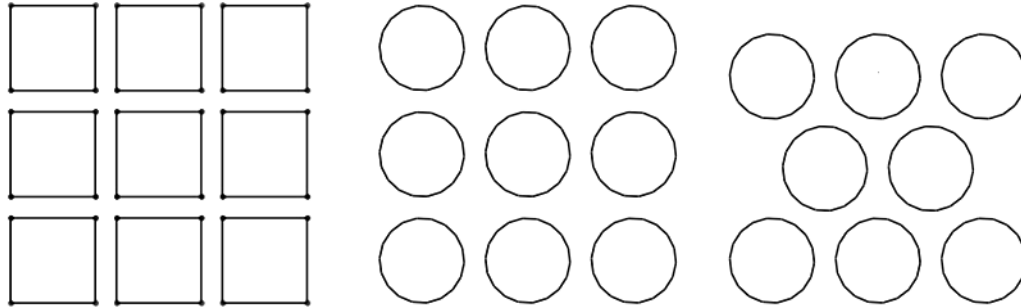


Figure 4.9: Comparison of the three fiber/cap arrangements showing the relative spacing between the caps. The square array of the circular caps apparently has the most spacing between the caps, resulting in more undercuts for the square arrayed circular fibers from uncollimated exposure as compared to the other two arrangements.

Comparing the adhesion of the mushroom fibers with central defects, as shown in **Figure 4.7(b)**, we can see that the adhesion is stronger with spot rectangular defects at the center (C_{34} and C_{54}) as compared to the bar-like defects which run across the cap surface (C_{21} and C_{14}). This can be attributed to the larger contact area between the cap and the attaching surface for the rectangular defects as compared to the bar-like defects, resulting in relatively prolonged adhesion before the crack finally initiates at the center and propagates to cause detachment. However, despite the bar-defect being approximately 3 times the size as the rectangular one, its strength is only halved.

Figure 4.8(a) and (b) compares the adhesion force of fibers with small and relatively large cap defects respectively. For the small defect group, the defect width spans from around $3.5 \mu\text{m}$ to around $4.7 \mu\text{m}$. These defect sizes were enough to induce anisotropy in all the samples, demonstrated by the asymmetric nature of the graphs. Quite interestingly, the fibers with bar-like defects with dimples (C_{22}) looks like it

outperformed the ones without dimples (C_{13}) but variability was so high that this may not be a real effect. The maximum normal adhesion force of C_{22} was 17.75 mN at a shear displacement of 15 μm which is very close to the maximum normal adhesion force of similar fibers without any defect (~ 18.4 mN at zero shear displacement for C_{11}). The dimples in C_{22} and C_{23} were originally designed to prevent the recessed surface from contacting the attaching surface at larger preload, thus retaining anisotropy. But it somehow improved the overall adhesion as well. The bar-like defects with no dimples performed best amongst the remaining samples.

The fibers with larger dimpled bar defects (C_{23}) demonstrated better adhesion amongst its peers as well, shown in **Figure 4.8(b)** and **Figure 4.4**. With the exception of fibers with square caps (S_{11}), other samples with similar defect size but different defect shapes showed comparable adhesion in this case.

4.4 Adhesion tests at higher preloads:

A series of tests were conducted on C_{13} samples with similar test parameters but at progressively higher preloads to determine if the fibers retained anisotropy in adhesion at larger preloads. The results, plotted in **Figure 4.10**, demonstrate that the fibers adhesion do retain directionality at larger preloads which indicates that the defect depth of 800 nm was large enough to ensure no-contact between the recessed surface of the cap and the attaching surface.

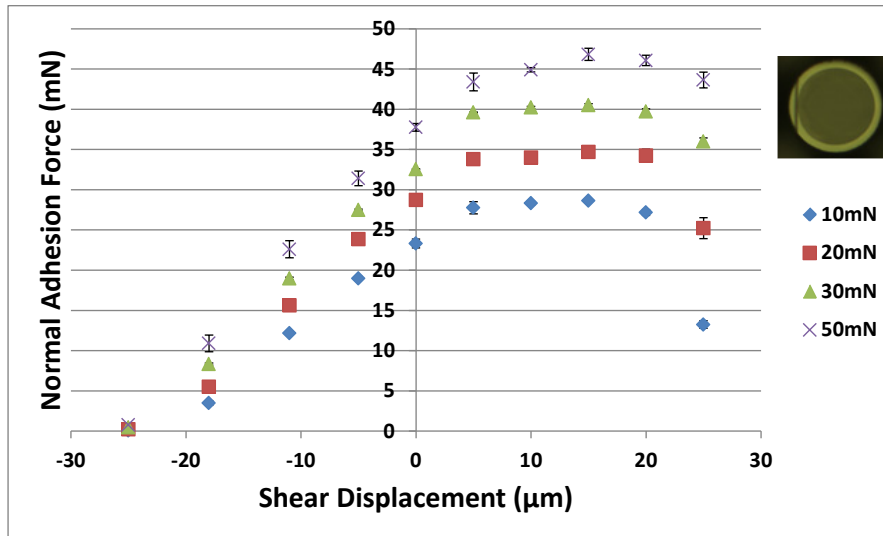


Figure 4.10: Adhesion test results of C₁₃ polyurethane samples at larger preloads

Based on the results presented, several key findings can be summarized:

- Adhesion anisotropy for mushroom shaped fibers can be achieved through the use of offset defects that concentrate stress on one side of the fibers
- Bigger defect lengths (towards fiber center) produce lower adhesion in the absence of shear
- Larger defect perimeters for similar crack lengths result in lower adhesion forces
- Notch type defects may be better than toroidal defects for larger adhesion forces, but are likely more sensitive to peeling/shear directions.
- High aspect ratio fibers will need larger displacements but lower forces to achieve best adhesion in the presence of shear with this fabrication technique.
- The exact location and size of the defect has huge impact on the performance of adhesive designs, so alignment and ease of manufacturing is extremely important.

- Relative performance of fiber designs can be roughly predicted by the relative stress at the defect edge for similar materials and loading conditions.

4.5 Adhesion Force of the Hot-embossed W3 adhesives

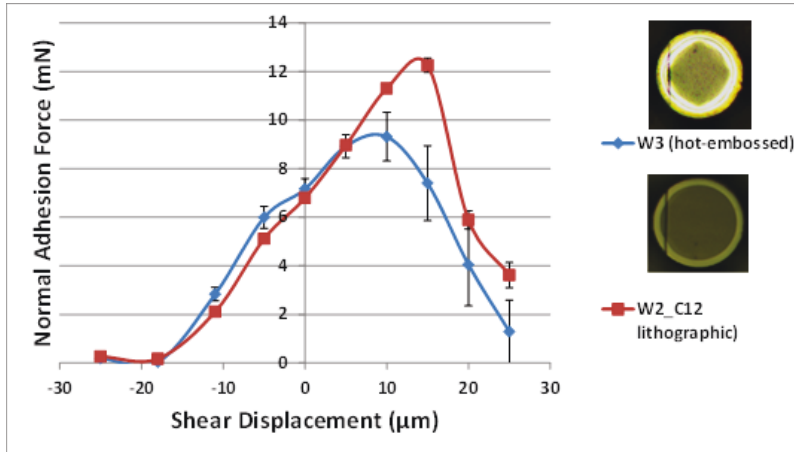


Figure 4.11: Normal adhesion force vs shear displacement plot for the polyurethane W3 adhesives

Figure 4.11 shows the adhesion force against various shear displacements for the hot-embossed anisotropic adhesive mold replicated in polyurethane. It also compares the adhesion force with the photolithographically produced fibers with similar defect type and size, i.e. C₁₂ of W2 mold (5.97 μm for C₁₂ vs 5.88 μm for W3). For fibers with very rough caps, as shown in **Figure 3.6**, the adhesion force values are unexpectedly good with comparable adhesion at zero shear. This indicates that the concept of hot embossing to make the large scale versions of the adhesives is still very promising, although some modifications to the procedure is necessary in order to avoid the roughening of the cap surface. If the roughening can be eliminated, the adhesion force would almost certainly go up to match the values corresponding to C₁₂, shown in this

figure and also in **Table 4.1**. As such, the basic concept of an all-embossed mold may be developed in the future to scale up the size of anisotropic molds while maintaining consistent adhesive performance.

4.6 Carbon Black-polyurethane composite adhesives.

Carbon black-polyurethane composite adhesives were prepared by adding a specific amount of carbon black to the antistatic ST-1060 polyurethane in steps followed by thorough mixing by hand. Carbon blacks with 4 %, 8 %, 10 %, 12 %, 14 % and 16 % by weight had been added to separate ST-1060 antistatic samples. Adhesive samples were made using the compression molding technique described in Section 3.4 and demonstrated in **Figure 3.7**. Some pucks were also made from the composite using a squeegee technique in order to test the conductivity of the samples. The resistance of the pucks was measured using a 2-point probe resistance meter (Model 152P-2P, Trek Inc.). **Figure 4.12** shows a plot of the log mean resistance against the carbon black concentrations demonstrating the roughly linear relations between the logarithmic values of the mean resistance of the pucks and the carbon black concentrations. In other words, increasing the carbon black concentration increased the conductivity of the samples exponentially for the concentration range tested. However, the standard deviation for the resistance data was also very high, resulting from the poor dispersion of carbon black particles due to hand mixing. Use of a proper mixing tool such as a 3-roll mill is highly recommended for future sample preparation.

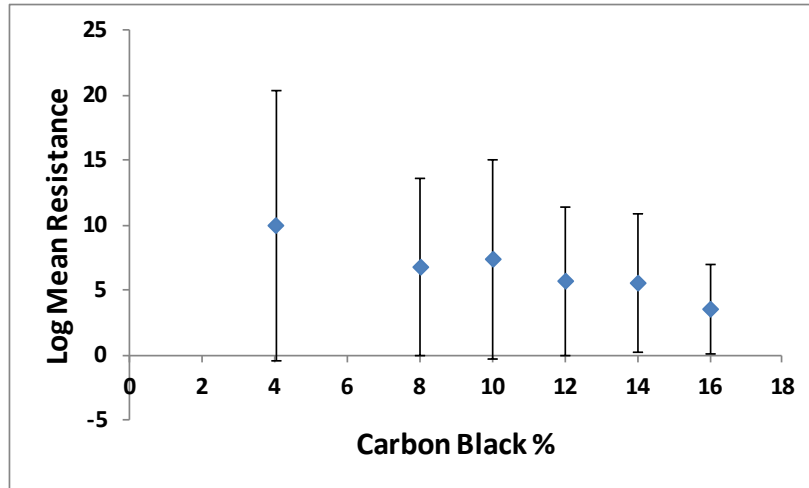


Figure 4.12: Graph showing the log mean resistance values for different carbon black concentrations.

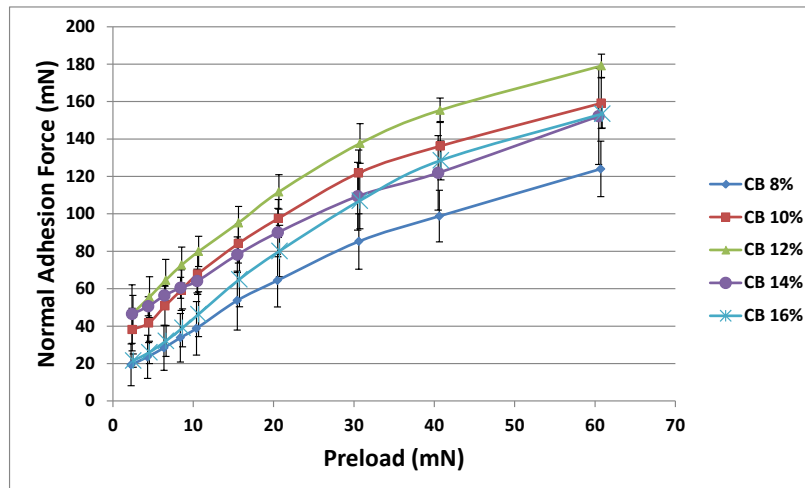


Figure 4.13: Comparison of adhesion forces of carbon black samples made out of CII mold [58]. The isotropic (non-defective) fibers are $\sim 25 \mu\text{m}$ tall, $\sim 24 \mu\text{m}$ cap diameter with $\sim 3 \mu\text{m}$ overhang and $\sim 2 \mu\text{m}$ cap thickness.

Figure 4.13 compares the normal adhesion forces of the different carbon black-polyurethane composite samples at different preloads. It appears that the mean normal adhesion force increased slightly with the increase in carbon black concentration up to 12 % by weight of carbon black and then the adhesion dropped with further increase of

carbon black content. Since the addition of carbon black particles increases the stiffness of the fibers, which itself is a factor on which the adhesion depends, this result suggests that the stiffness of the particular type of fibers reach an optimum level with respect to adhesion at 12 % by weight of carbon black.

Figure 4.14 shows the adhesion force plot of an anisotropic carbon black composite with 16 % CB of C₁₃ type. Even though the adhesion force is approximately 25 % less for the carbon black composite, it still demonstrated similar anisotropy. Perhaps with a softer polymer matrix, the adhesion force might increase to the level of ST-1060 polyurethane.

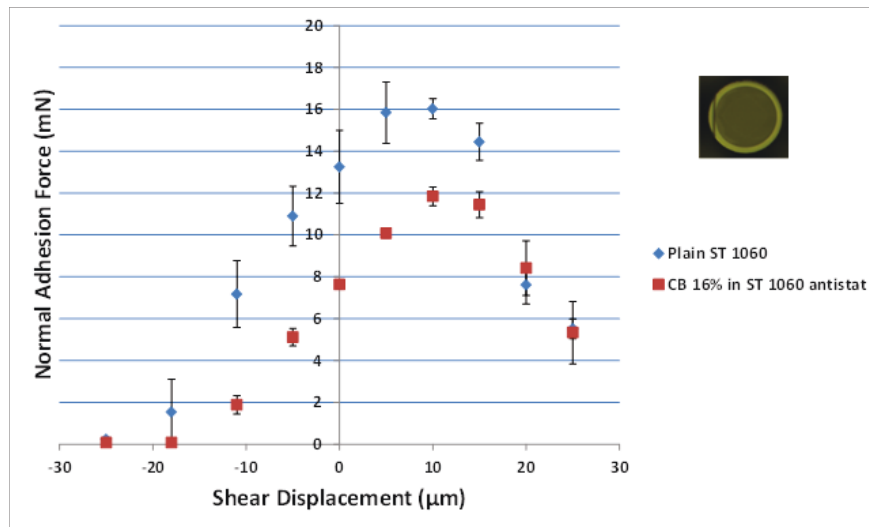


Figure 4.14: Comparison of adhesion between 16 % carbon black-polyurethane composite adhesives and pure polyurethane adhesives made from C₁₃ sample of W2 mold.

To conclude, adhesion test results are presented and analyzed for samples produced by conventional photolithography as well as with hot-embossing. The adhesion test results

confirm our general predictions from the finite element analysis about the performance of the directional and non-directional fibers. In both cases, the introduction of a deliberate defect to one side of the fiber resulted in predictably directional adhesion force. The embossing trials were complicated by the much rougher top surface of the caps, but maintained directionality through the original designed defect. Improvements to hot-embossing techniques should produce reliable and uniform directional adhesives for large scale peel tests. In addition, a recipe for the fabrication of polyurethane-carbon black composite fibers is outlined for anti-static applications such as MEMS pick and place. 12 % carbon black by weight apparently yielded better results in terms of conductivity and adhesion strength of fibers.

5. Thermoplastic elastomer as the structural material for dry adhesives⁴

Traditionally, synthetic dry adhesives are mainly made out of polyurethane or PDMS [78] mainly because of their softness (43-Shore A for PDMS and 60 Shore A for polyurethane) providing good compliance for the fibers, and good replication fidelity. In addition, polyurethane has a high tensile strength (~6 MPa [79]) and good tearing strength (~21 kN/m [80]) making the fibers reasonably resistant to tearing. This chapter discusses the prospect of these materials in terms of oligomer transfer. Additionally, SEBS thermoplastic elastomer is introduced for the first time as a structural material for dry adhesives and it is demonstrated to be capable of similar performance to ST-1060 while being less likely to transfer oligomers to other surfaces. A preliminary examination of the effect of oligomer transfer on wire-bonding yields is also investigated in this chapter.

5.1 Background

Contamination of the surface of a MEMS device and microelectronic chips due to particle transfer is undesirable [81] as the particles might affect the operation of the circuitry of the microelectronic devices and might also interfere with the motion of the moving parts of a MEMS device. Careful study on the material transfer is therefore necessary whenever a process involves physical contact between a handling device and a MEMS die or microelectronic chip. During MEMS packaging in laboratories or small-

⁴ Sections of this chapter are published in [126] and [128] and are reproduced or adapted from the original articles.

scale prototyping, the devices are usually handled and transferred manually using tweezers, vacuum tips, etc. These devices can potentially be transferred during packaging using end effectors employing gecko inspired dry adhesive [58] as well as using micro-transfer printing[54, 82-84], both of which largely employ polymers to make the attaching devices or stamps. Although polymers such as polypropylene [31], polyvinylsiloxane [49] and poly(urethane acrylate) [32] have been used before to make the dry adhesives, polyurethane and PDMS remained the material of choice for these adhesives because of their performance [34][40][52][61][85-92] and relative ease of manufacturing using soft lithographic techniques [93].

The pick and place process would involve the dry adhesive coated end-effector to be in contact with a portion of the die for a certain period of time as a result of which there might be some transfer of oligomers (low molecular weight compounds consisting of a few monomer units) from the polymer adhesive to the die. Also, manufacturing of these adhesives often involves the casting of the adhesive material (polyurethane, for instance) on a secondary negative mold made of silicone, for example [60][94], which opens up the possibility of some oligomer transfer from the silicone mold into the polyurethane adhesive and eventually into the contacting die.

Transfer of oligomers due to contact is thought to take place because of molecular interactions, electrostatic forces, etc. [81] and might depend on factors such as contact time, contact pressure, curing and or pretreatment of the stamp, etc. Yang et al. [95] reported that the oligomer transfer during micro-contact printing depends on surface energy of the contacting surface as well, with more tendencies to transfer to hydrophilic surfaces as compared to hydrophobic ones. Wigenus et al. reported that the transfer of

PDMS oligomers increased with the increase of contact time [96]. Similar results were obtained by Yunus et al. [97] although in both of these works, the upper limit of contact time reported was ≥ 1000 min which is much larger than the usual contact time involved in pick-and-place applications (a few seconds). The amount of oligomers transferred did not vary too much within a minute period in either of these reports, which is the upper limit of contact time in our work, as outlined in **Table 5.1**.

This work investigates the oligomer transfer due to contact from PDMS, polyurethane rubber and SEBS thermoplastic elastomer (Styrene-Ethylene/Butylene-Styrene) puck onto the surfaces of gold-coated silicon dies. Additionally, any transfer of oligomer from the intermediate PDMS mold to the final polyurethane or SEBS sample upon casting is also investigated.

Transfer of low molecular weight PDMS fragments during contact has been widely reported, mostly in the case of micro-contact printing where PDMS was used as the stamp material [95][97-106]. Nandini et al. [107] investigated the contamination of silicon using certain other polymer materials (UHMWPE, Teflon, KEL-F, PMMA, Nylon 66, PEEK). However, there is little study, if any, involving the transfer of oligomers from polyurethane stamps, which is also a commonly used material for the dry adhesives.

Trimbach et al. claimed in their article [108] that Kraton SEBS does not transfer oligomers during micro-contact printing unlike their PDMS counterparts, but they did not present any experimental evidence to back their claim. Hence this study is conducted to investigate the transfer from polyurethane, Kraton and PDMS in order to determine the suitability of these materials for dry adhesives in terms of surface contamination, which might be critical for pick and place applications. The SEBS Kraton

was investigated because of its potential as an alternative to the thermosetting PDMS and polyurethane which, despite having good mechanical properties, has the disadvantage of long processing times, high base material cost. On the other hand, the SEBS thermoplastic elastomers can be processed very rapidly using thermo-compression molding, are cheaper and scalable, all of which is favorable for large scale manufacturing.

Previous studies to investigate the surface contamination from contact used processes/tools like X-ray Photoelectron Spectroscopy XPS [98][101][103][109], Infrared reflection-absorption spectroscopy (IRAS) [102], Time-of-flight Secondary Ion Mass Spectroscopy (ToF-SIMS) [100][110], Fourier Transform Infrared Spectroscopy FT-IR [98][109], Atomic Force Microscopy AFM [96][98][111], optical micrographs [107], and Scanning Electron Micrographs SEM [107]. In this work we used high resolution XPS analysis to investigate the transfer of the materials from the puck to the gold-coated silicon die. We also investigated any successive transfer of PDMS oligomers via an intermediate means (polyurethane or Kraton SEBS in this case).

Figure 5.1 shows the molecular structure of the three polymer materials that we tested for oligomer transfer. The silicon dies were coated with 50 nm gold layer in order to make the test surface free of silicon atoms, which would interfere in the identification of PDMS oligomers. Since nitrogen atoms are present in the polyurethane structure but not SEBS or PDMS, N 1s electrons were used as the identification element of polyurethane. Kraton SEBS has only hydrogen and carbon in its molecular structure (**Figure 5.1c**), so C 1s electrons could be used to identify the presence of Kraton, as XPS is not suitable for identification of hydrogen electrons. Since there is a possibility of

adsorption of hydrocarbon from the atmosphere by the die, and thus affecting the XPS analysis of SEBS-contact samples, the results were compared with that of a control die which was kept in a similar condition as the other dies except it did not undergo any contact with any of the polymers. Si 2s electrons were used to identify the presence of PDMS oligomers.

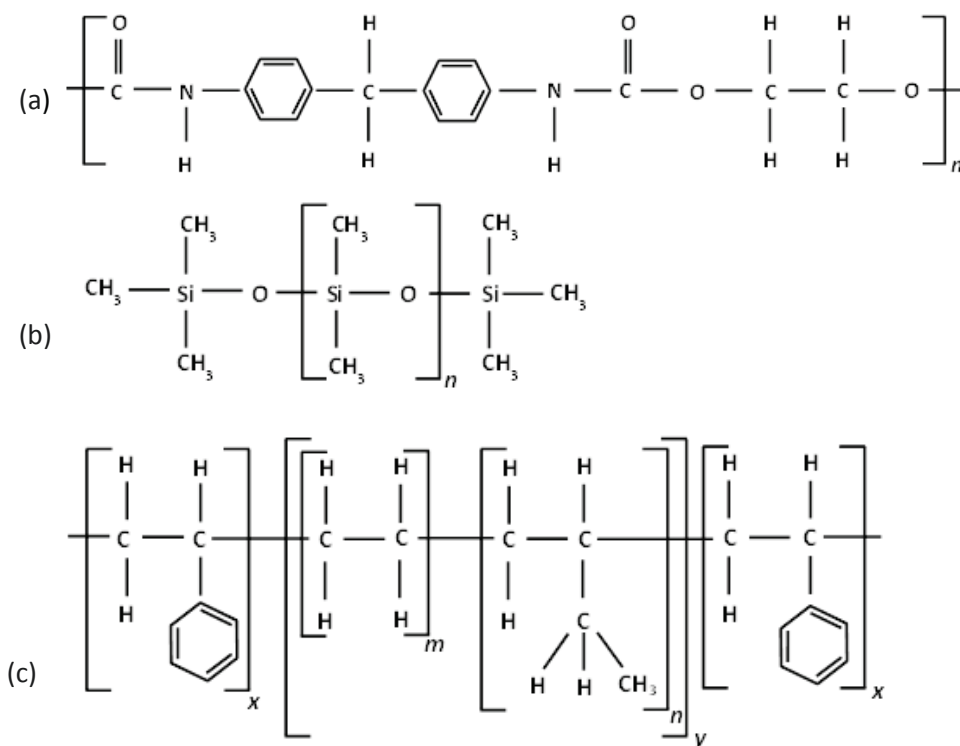


Figure 5.1: Molecular structures of (a) Polyurethane; (b) PDMS and (c) Poly(styrene-ethylene/butylene-styrene) (SEBS). The image is published by the author in [128] and is reprinted with permission.

5.2. Surface analysis using X-Ray Photoelectron spectroscopy (XPS):

X-ray photoelectron spectroscopy (XPS), also known as electron spectroscopy for chemical analysis (ESCA) is the most widely used surface characterization method [112].

Other commonly used surface analysis techniques are Auger Electron Spectroscopy

(AES), Secondary Ion Mass Spectroscopy (SIMS), Infrared Spectroscopy, Atomic Force Microscopy (AFM), Scanning Electron Microscopy (SEM), etc. The primary components of an XPS system are the vacuum system, X-ray source, electron energy analyzer, and the data analysis system, shown in **Figure 5.2**.

In XPS, the target material surface is irradiated with an X-ray beam. The high energy photons from the X-ray beam interact with the core orbital electrons at the surface of the exposed material, exciting the electrons and eventually leading to their emissions. Provided the threshold frequency of photoemission is exceeded, the number of electrons emitted is proportional to the intensity of illumination. The emitted photoelectrons are guided by an electron lens into a hemispherical energy analyzer. An electrostatic field in the hemispherical analyzer causes the photoelectrons to deflect. The deflection of the electrons depends on their energies and only those with a certain range of energies pass successfully from the entrance to the exit of the analyzer. The magnitude of this electron energy range depends on pass energy, the size of the entrance slits and the angle with which the electrons enter the analyzer. This range is usually ~10 % of the pass energy [113]. A multichannel detector plate then counts the number of electrons leaving the analyzer at each energy level.

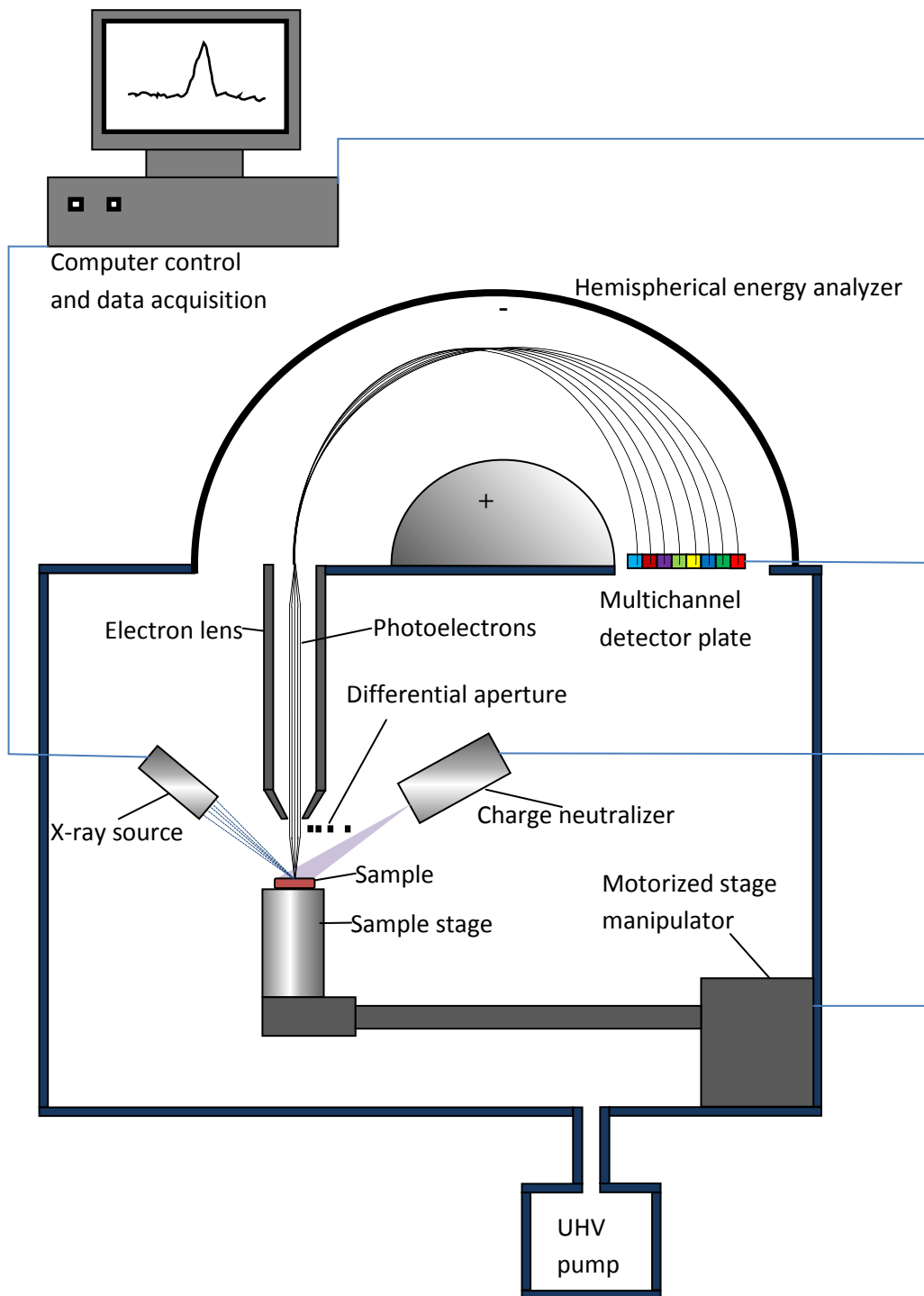


Figure 5.2: Schematic diagram of an X-ray photoelectron spectrometer showing its key components.

The binding energies of each electron, E_B , is given by

$$E_B = h\nu - KE \quad (18)$$

Where $h = 6.626 \times 10^{-34}$ J s [114] is the Planck's constant and ν is the frequency of the X-ray. The product $h\nu$ is the energy of the X-ray source and KE is the kinetic energy of the photoelectron measured by the multichannel detector. The binding energy is a function of the type of atom and its environment. Determining the value of the binding energy thus gives us information about the photo-emitting atom. The computer processor acquires the data from the XPS and displays the spectrum consisting of peaks corresponding to the different types of element present in the outer 10nm of the sample surface. The area under the peaks gives us an estimation of the amount of each element present. The percentage of each element can be determined by measuring the area under the peak and correcting them for instrumental factors.

The atomic concentration, n_i of an element i is given by

$$n_i = \frac{I_{ij}/S_i}{\sum I_i/S_i} \quad (19)$$

Where I_{ij} is the peak area of the peak j from element i , S_i is the relative sensitivity factor (RSF) of the core level j of element i .

Charge neutralizer is sometimes used while analyzing samples which are poor conductors of electricity. To avoid the build-up of positive charge due to emission of photoelectrons, the sample is flooded with low energy (<20eV) electrons.

5.2.1. XPS parameters used in the surface contamination tests:

The XPS measurements were performed on ULTRA XPS spectrometer (Kratos Analytical) at the Alberta Centre for Surface Engineering and Science (ACSES), University of Alberta. The base pressure in the analytical chamber was lower than 3×10^{-8} Pa. Monochromatic Al K α source ($h\nu = 1486.6$ eV) was used at a power of 210 W. The analysis spot was 400×700 μm . The resolution of the instrument is 0.55 eV for Ag 3d and 0.70 eV for Au 4f peaks.

The survey scans were collected for binding energy spanning from 1100 eV to 0 with analyzer pass energy of 160 eV and a step of 0.4 eV. For the high-resolution spectra the pass-energy was 20 eV with a step of 0.1 eV. Charge neutralization was not required. Vision-2 instrument software was applied to process the data. All spectra were calibrated for C1s binding energy position at 284.8 eV.

5.2.2. Sample preparation

SEBS and polyurethane pucks were made by casting on separate silanized borofloat glass substrates as well as on separate plain PDMS surfaces followed by curing or drying, mimicking a common practice of casting a polymer on a negative PDMS template to produce micro-structured adhesive fibers. The PDMS pucks were produced by casting on two separate silanized borofloat glass substrate followed by degassing and curing at 80°C in an oven for two hours. A few circular dots of PDMS were also produced in a separate section of one of the substrate.

An SEBS solution was previously prepared by adding 5 g of solid Kraton G1657 pellets (Kraton Performance Polymers Inc.) to 75 ml of hexane followed by stirring on a

magnetic stirrer. The SEBS solution was cast multiple times on the PDMS surface, in the form of arrays of dots (~10 mm diameter), to produce a layer of a few hundred micrometers thick after the hexane evaporated. This eliminated the majority of the dust that would otherwise be present on the pellets of neat resin and was otherwise not feasible to remove. The polyurethane puck was made of ST-1060 (BJB Enterprises), a thermoset elastomer commonly used to produce dry adhesives [34][61][115][116] which was prepared by mixing the two components to the manufacturers recommended ratio followed by degassing, and casting on the second PDMS puck, also in the form of arrays of dots, followed by curing at room temperature for at least 48 hrs.

Several gold-coated silicon dies were cleaned by dipping into a piranha solution (3 part H_2SO_4 (96 %) and 1 part H_2O_2 (30 %)) for 15 minutes followed by rinsing with DI water and drying with nitrogen. The PDMS, polyurethane and SEBS pucks were then brought separately into contact with the surface of gold-coated silicon dies for durations of 5, 15 and 60 seconds as outlined in **Table 5.1**. All the samples were prepared within an hour of the cleaning in a cleanroom environment and left sealed in containers before mounting on the XPS stage. For applications like MEMS pick-and-place, these adhesives would be expected to be in contact for relatively short times and therefore these contact periods were felt to be representative of our expected applications.

Table 5.1: Material, conditions and durations of contact of the polymer pucks with the dies. The table is published by the author in [128] and is reproduced with permission.

	Sample no.	Contact material/condition	Contact time(s)
	1	Control wafer (no contact)	0
Case 1	2	Plain Polyurethane	5
	3	Plain Polyurethane	15
	4	Plain Polyurethane	60
Case 2	5	Polyurethane cast on PDMS	5
	6	Polyurethane cast on PDMS	15
	7	Polyurethane cast on PDMS	60
Case 3	8	Plain Kraton G1657	5
	9	Plain Kraton G1657	15
	10	Plain Kraton G1657	60
Case 4	11	Kraton G1657 cast on PDMS	5
	12	Kraton G1657 cast on PDMS	15
	13	Kraton G1657 cast on PDMS	60
Case 5	14	Plain PDMS	5

5.2.3 XPS Results:

Preliminary data analysis and atomic compositions were calculated using Casa XPS Software. The compositions were calculated using Scofield sensitivity factors. The high resolution XPS spectrum data points were then exported into Microsoft Excel 2010 and the graphs are plotted as shown in **Figure 5.3** to **Figure 5.6**.

Table 5.2: Binding energies and relative sensitivity factors of the relevant electrons [117]. The table is published by the author in [128] and is reproduced with permission.

Element	Binding Energy (eV)	Relative sensitivity factors
Si 2s	149	0.955
C 1s	284	1.00
N 1s	399	1.8
O 1s	532	2.93
Au 4f 7/2	83	9.58

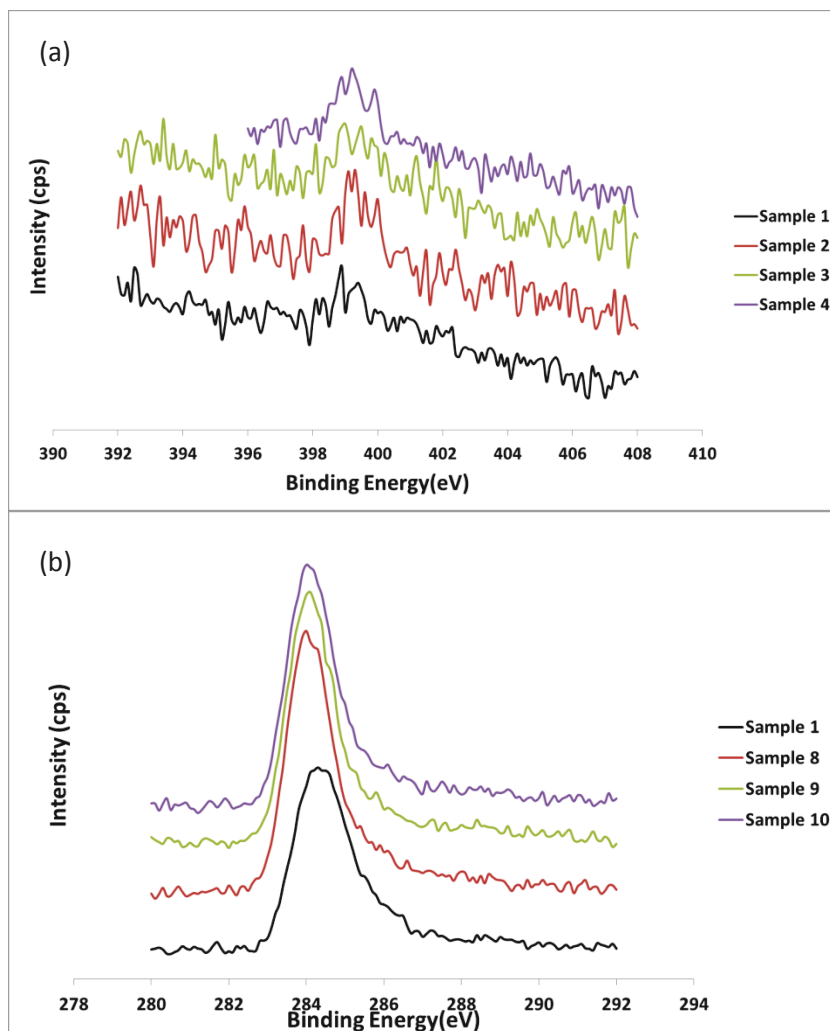


Figure 5.3: High resolution XPS spectra comparing control sample with (a) case 1 samples showing N 1s peaks; (b) case 3 samples showing C 1s peaks. Some of the spectrums are deliberately offset in the y-axis for clarity.

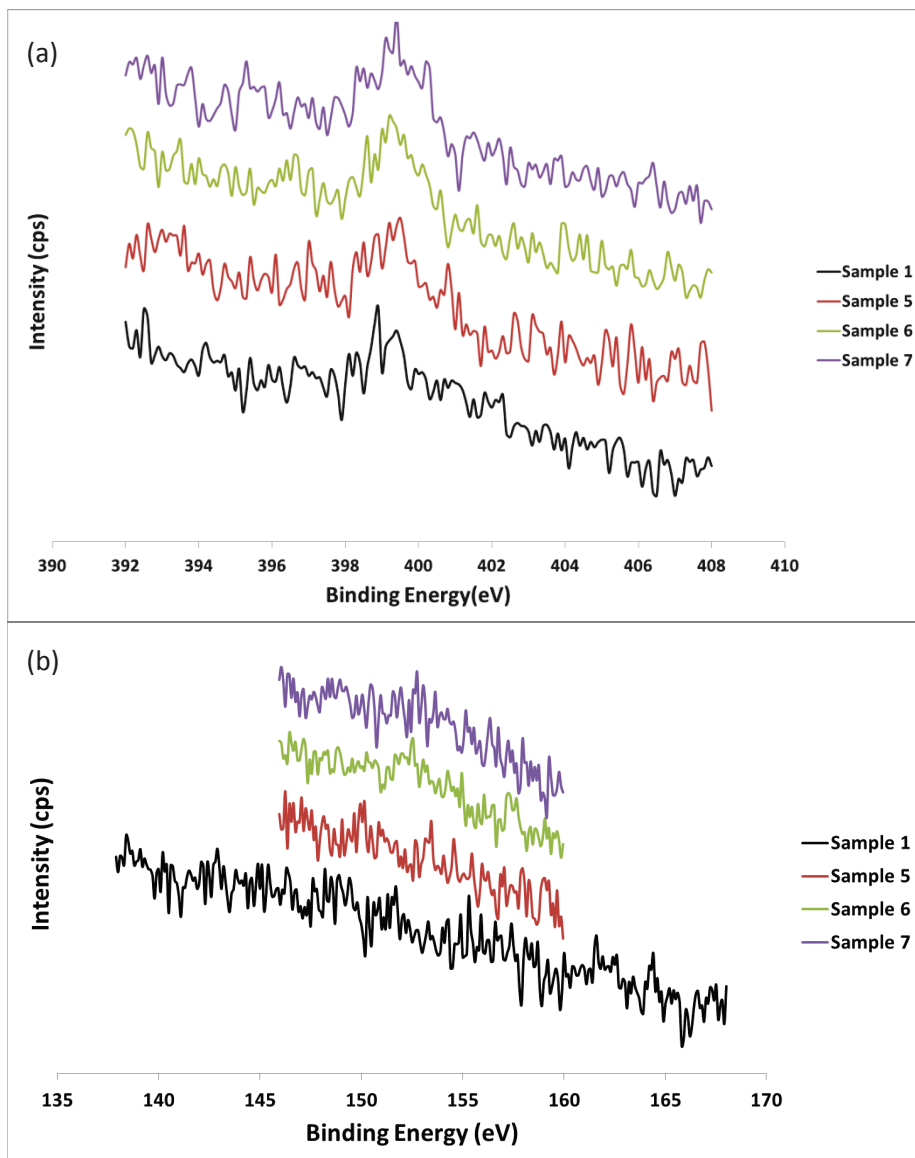


Figure 5.4: High resolution XPS spectra comparing control sample with (a) case 2 samples showing N 1s peaks; (b) case 2 samples showing Si 2s peaks. Some of the spectrums are deliberately offset in the y-direction for clarity.

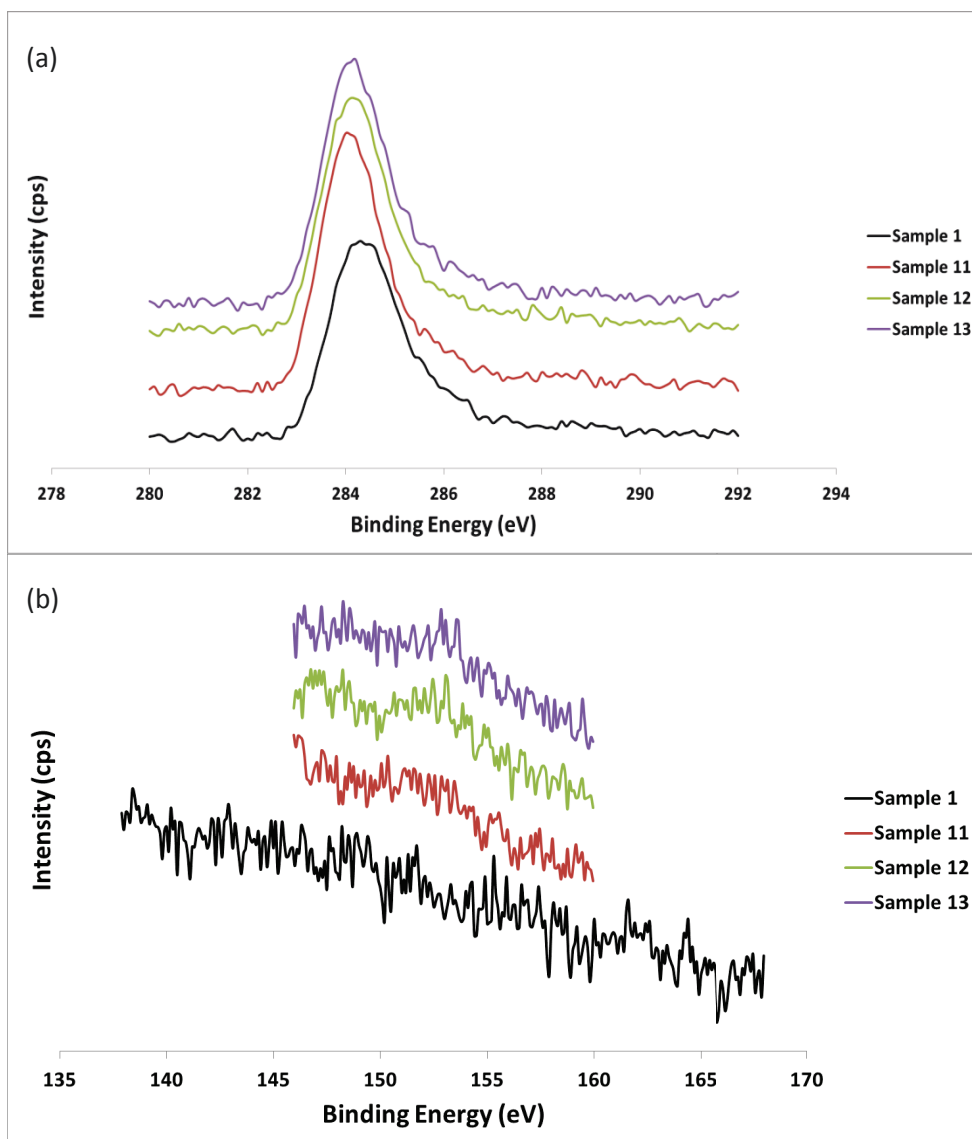


Figure 5.5: High resolution XPS spectra comparing control sample with (a) case 4 samples showing C 1s peaks; (b) case 4 samples showing Si 2s peaks. Some of the spectrums are deliberately offset in the y-direction for clarity.

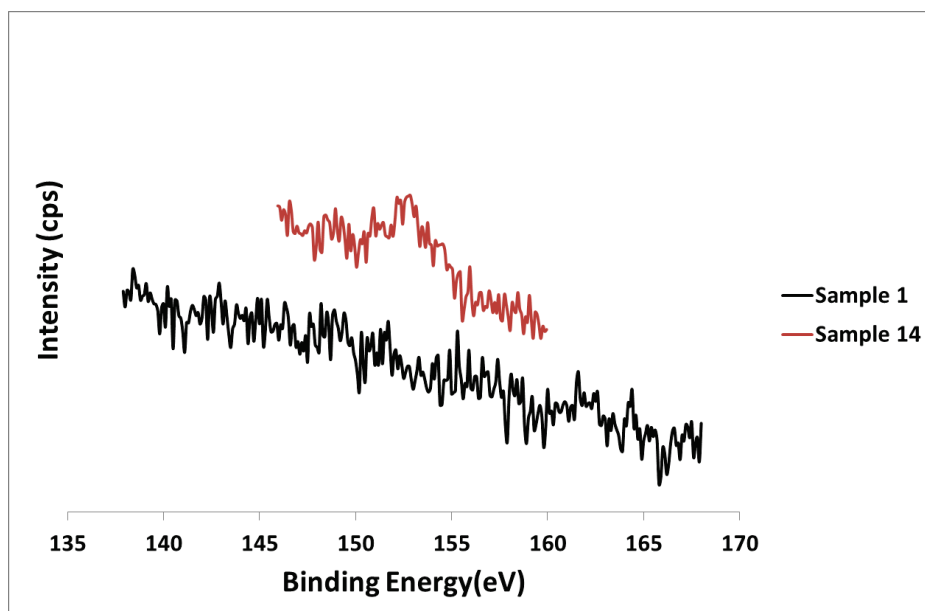


Figure 5.6: High resolution XPS spectra for comparing the control sample with case 5 sample showing Si 2s peaks.

The binding energies of the relevant photoelectrons are given in **Table 5.2**. From **Figure 5.3(a)**, which compares the N 1s spectra of case 1 samples with that of the control sample, we can see that the peaks at 399 eV for the case 1 samples are a little more pronounced than that corresponding to the control sample, suggesting that the case 1 samples have a higher N 1s content. This is verified by the atomic composition calculation in **Table 5.3**, where N 1s concentration was found to have increased slightly from 0.5% in control sample to 1.6%, 1.3% and 1.8% in samples 2, 3 and 4 respectively. The decrease of the background Au 4f % from the control sample to the case 1 samples and a simultaneous increase in N1s content is suggestive of a possible polyurethane oligomer transfer from the puck to the die surface during contact. A similar trend of increase in N 1s concentration and decrease in Au 4f concentration can be observed for case 2 samples, corroborating our findings above.

Table 5.3: Atomic composition calculated from high resolution XPS spectrum. The table is published by the author in [128] and is reproduced with permission.

Case	Sample	Atomic Composition (%)				
		N 1s	C 1s	O 1s	Si 2s	Au 4f
<i>Control</i>	1	0.5	23.8	5.2	~0.0	70.5
1	2	1.6	23.1	4.6	~0.0	70.7
	3	1.3	24.8	6.5	~0.0	67.4
	4	1.8	24.0	6.1	~0.1	68.1
2	5	2.5	24.1	4.4	0.6	68.4
	6	1.8	25.6	5.8	2.0	64.8
	7	2.2	24.9	7.1	1.5	64.3
3	8	~0.0	25.4	5.0	~0.0	69.6
	9	0.1	25.0	4.0	~0.0	70.9
	10	~0.0	25.3	2.7	~0.0	71.9
4	11	0.6	25.0	4.7	2.6	67.2
	12	0.7	23.6	5.5	3.0	67.2
	13	0.7	26.8	4.7	1.0	66.8
5	14	0.4	24.9	7.0	3.2	64.5

Interestingly, there is a slight increase in Si 2s concentration for sample 6 and 7 as compared to negligible amount in control sample, as shown in **Table 5.3**, suggesting that some oligomers might have made its way from the PDMS mold to the dies via the polyurethane puck. The slight bulging of the spectrum at 153 eV in **Figure 5.4(b)** for case 2 samples supports the suggestion. This cross contamination of PDMS from an original mold will also be a possible concern for any adhesives manufactured with soft-lithography techniques, but would potentially be solvable via some surface cleaning of adhesives prior to use. In these measurements, sources of error can include variations in transfer across a single sample and the introduction of operator judgment in measuring the peaks, along with inherent noise within the signal. The composition percentages can generally be considered accurate within 10 %.

Regarding the case 3 SEBS samples, it can be seen that the O 1s concentration dropped amid a slight increase of C1s concentration, which suggests that there might be some SEBS oligomer transfer as well, which consists of only carbon and hydrogen. If the original carbon and oxygen content is primarily adsorbed CO₂ then it is possible that some of this is displaced by the SEBS, although the gold concentration remains so close to the original control sample that it is possible that there is negligible transfer. Similar to **Figure 5.4(b)**, the Si 2s peaks for samples 11, 12 and 13 in **Figure 5.5(b)** also shows that some PDMS oligomers might have made its way into the die via the intermediate SEBS puck. The increase in Si 2s atomic concentration for samples 11 and 12 in Table 3 corroborates this observation.

Referring to **Figure 5.6** and atomic composition values in **Table 5.3**, we can see that there is an obvious Si 2s peak in the XPS spectra for sample 14. The concentration of Si 2s increased from negligible amount in the control sample to 3.2 % in sample 14, indicating possible oligomer transfers from PDMS puck to the gold-coated die surface, as are expected without significant modification to the silicone [18][19].

In all the cases, there is little evidence of significant variation in the amount of material transferred at different contact duration which agrees with previous reports [17][28] where the amount of oligomer transfer increased significantly only at large duration of contact (>>1 min) and not within a minute period which was the range of duration of contact in our work. Given the general levels of composition and adsorbed carbon on even the control sample, it is apparent that the amount of material transferred from the SEBS onto the gold surfaces is very small and if it is in its pure form without any surface contamination from PDMS, easily appears to have the least rate of transfer of the

materials tested. Multiple contacts of the SEBS sample with a clean surface should mostly deplete this supply of surface oligomers and reduce the possibility of transfer with future use. From this we can conclude that SEBS thermoplastic elastomers would be an acceptable choice as a low or minimally contaminating thermoplastic candidate in comparison to curable polyurethane or silicone rubbers.

5.3 Wire-bonding test:

One of the potential effects of oligomer transfer onto the dies is that they might disrupt the wire bonding process if present in sufficient quantities. To investigate this issue, a PDMS puck, which was found to be the worst in terms of oligomer transfer in the section 5.2, was left into contact with a clean gold coated silicon die for 1 minute (longer than the contact period for case 5 in **Table 5.1**) and the die was subjected to wire bonding trials, as shown in **Figure 5.7**.

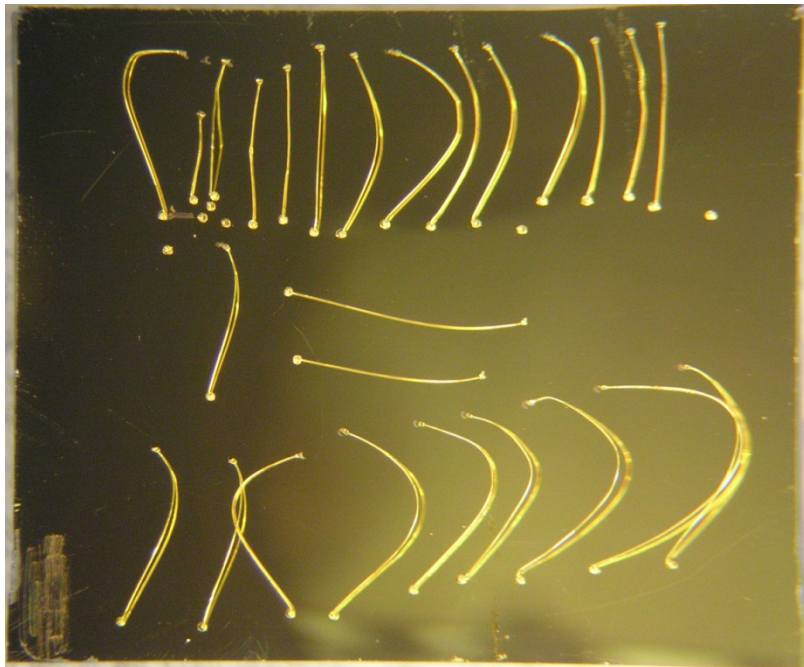


Figure 5.7: Gold coated silicon die with 26 wire bonds. The bare ball joints with no wires were due to tip blockage which is due to the aging tip and not a bond failure.

600 W power and 300 millisecond bond time was used for the trials. These parameters could be optimized based on the bond pad and wire material if necessary for better yields.

26 trials of wire bonding were conducted on the die and there was no apparent bond failure. A few visible gold balls on the die with no wires were a result of tip failure (blockage due to repeated bonding), and not a bonding issue. Even if those are considered as bonding failures, the success rate is around 81 % which is very promising. This implies that even the amount of oligomer transfer from PDMS is not large enough to cause any apparent wire bonding issue. However, because there was no other infrastructure on campus to detect other modes of bond failure (specifically shear force or normal force pull-off trials), it should be further pursued with better equipped packaging companies with standard wirebonding equipment and previously optimized equipment and parameters to conclusively demonstrate reliability. If that can be done for the PDMS adhesive material, then it is unlikely that any of the other polymers used in this work will be a significant source of wirebonding failures.

5.4. Fabrication of SEBS thermoplastic elastomer adhesive samples by thermo-compression molding

Although the material transfer of SEBS was found to be very small, it would still not be an acceptable material for use if it didn't have comparable adhesion properties (such as adhesion strength, long term durability and directionality) to those of the thermoset rubbers with identical microstructures. Of great importance to application in MEMS pick and place is high normal adhesion strength when pulled directly off of a substrate

(to remove MEMS die or devices from tape or substrates), and the ability to demonstrate directional behavior (for easy release) when structured with a particular defect to make them more vulnerable to peeling when loaded with a shear force. The manufacturing and testing of these particular adhesive variations is described below.

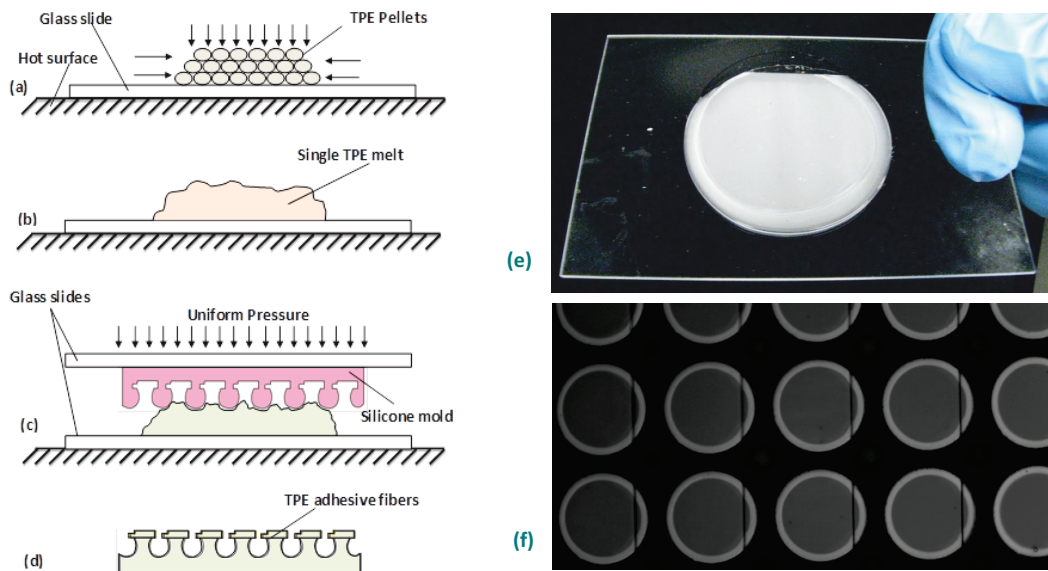


Figure 5.8: Schematic diagram showing the fabrication of thermoplastic elastomer (TPE) adhesives by thermo-compression molding. (a)-(b) SEBS pellets are melted together under light pressure to form a melt, (c) a silicone rubber mold is placed on the melt a pressed down slowly until the desired force is applied, (d) after approximately 30 seconds to fill the mold, the silicone, SEBS and glass slide are removed from the hotplate and cooled before the silicone is demolded, (e) macro scale view of an SEBS adhesive sample, (f) microscopic image showing arrays of anisotropic adhesive fibers made of SEBS. The image is published by the author in [128] and is reproduced by permission.

Isotropic and anisotropic adhesive samples were fabricated out of Kraton SEBS by thermo-compression molding, shown in **Figure 5.8**, and their performance is compared with a polyurethane version manufactured from ST-1060. In this case, another version

of Kraton SEBS (G1645) was used that had a lower shore A hardness (~Shore A 35). The softer G1645 was qualitatively stickier than G1657 even in its unstructured form, but it did require more force or time to flow into molds at elevated temperatures as indicated by the lower melt-flow rate in **Table 5.4**. Such factors are ultimately necessary to consider in the trade-off between easy manufacturability and final adhesive performance because fibers with undesired defects will be much worse even if structural properties are more attractive. While other Kraton varieties were tested, not all were sufficiently flow-able at the temperatures and forces used to manufacture the adhesives in this work and are not reported here.

A negative template, made by casting silicone (TC-5030, BJB Enterprises) on a rigid mold in a process described elsewhere [65], was used as the master here. The template consists of the negative of both isotropic and anisotropic mushroom shaped fibers. The polyurethane versions of the adhesive fibers were manufactured by mixing ST-1060 polyurethane pre-polymer (BJB Enterprises, CA, USA) with the catalyst on a 100:55 ratio and casting on the silicone mold followed by degassing, curing at room temperature for at least 8 hours and post-cure baking for another 8 hours at 80 °C in an oven. The thermoplastic elastomer versions were made by a hot embossing/thermo-compression molding process, shown in **Figure 5.8**. Kraton G1657 and G1645 were obtained from Kraton Performance Polymers Inc. (Texas, USA). The relevant material properties are outlined in **Table 5.4**. Some recently reported work [118] suggests that viscoelastic components of material properties strongly influence adhesion behavior if a material is tested at a temperature at close proximity to its glass transition temperature T_g . There is no reported glass transition temperature for ST-1060 in the literature that we can find, but in the case of SEBS, the lower of the two distinct T_g values is that of the

ethylene-butylene and is typically listed as approximately -42 °C on company datasheets [119] or even lower in specific instances [120]. Our measurements occurred at 22 ± 1 °C and would likely be outside the temperature range found to be significant in the work of Lakhera et al. [118].

Table 5.4: Select material properties of ST-1060 polyurethane [80], Kraton G1645 [121], and Kraton G1657 [122]. The table is published by the author in [128] and is reproduced with permission.

Properties	ST-1060	Kraton G1657	Kraton G1645
Melt flow at 230 °C (g/10 min)	N/A	22	2-4.5
Hardness, Shore A	60	47	35
Tensile Strength (psi)	900	3400	1500
Elongation at Break (%)	590	750	>600
Modulus of elasticity at 300 % (psi)	560	350	N/A
Glass transition temperature, T_g	N/A	~-42 °C [119]	N/A

The Kraton G1657 and G1645 come in the form of pellets, slightly dusted to prevent sticking. A number of pellets were placed together on a microscope glass slide (**Figure 5.8a**) on a hot plate at 200 °C and squeezed to form a single melt (**Figure 5.8b**). The silicone master was placed on top of the melt at the desired location. This separate silicone mold was never used for polyurethane to prevent any undesirable contamination or toxic breakdown of polyurethanes. On top of the master and aligned with the Kraton SEBS melt, another pre-heated glass slide was placed and a cylindrical iron mass (~5 kg) was used as a load to squeeze the melt into the mold to form the mushroom shaped fibers (**Figure 5.8c**). The load was left on for a minute to allow for complete filling and removed afterwards. The glass/Kraton/silicone was then removed from the hotplate and placed on a metal surface at room temperature to cool down. The silicone master was then peeled off the Kraton SEBS, leaving the thermoplastic

adhesives on the bottom glass slide. The Kraton SEBS backing layer had low adhesion to the glass and could also be peeled off if desired (**Figure 5.8d**).

The fibers fabricated here were mushroom shaped with circular caps of 40 μm diameter and 2.8 μm thickness. The cap overhang was ~ 3.2 μm and the fibers were around 20 μm tall. Both isotropic and anisotropic mushroom shaped fibers were made using polyurethane and two versions of Kraton SEBS thermoplastic elastomers. The anisotropic fibers were produced based on a concept and technique described in [65], i.e. placement of a defect deliberately at the edge of the cap surface makes the adhesion of the fibers directional. Two different defect shapes, rectangular (C_{31} , **Figure 3.3**) and bar-like (C_{12} , **Figure 3.3**), are investigated in this report. In addition, caps with central defects (C_{14} and C_{34} , **Figure 3.3**), which is the worst case scenario for mushroom shaped fibers [75], were also fabricated to compare the vulnerability to defects for each materials. The defects were 800 nm deep for all cases, ~ 6 μm wide for C_2 and C_4 and ~ 7 μm wide for C_3 and C_5 . Due to SEM imaging difficulties of the Kraton SEBS polymers directly (due to the overhanging caps curling up after gold deposition from the stress mismatch), the images in **Figure 3.3** are of polystyrene replicas of the fibers, produced using identical times, temperatures and weights as the Kraton SEBS samples. Optical images revealed no significant dimensional differences between these and the Kraton SEBS versions, so these are used to demonstrate the basic fiber shapes.

5.5. Performance comparison between Kraton SEBS and polyurethane adhesives:

C₁ and C₃ adhesive samples were made out of both Kraton G1645 and G1657 and tested using the same parameters as described in Section 3.5 and compared with the ST-1060 polyurethane versions in **Figure 5.9** to **Figure 5.11**.

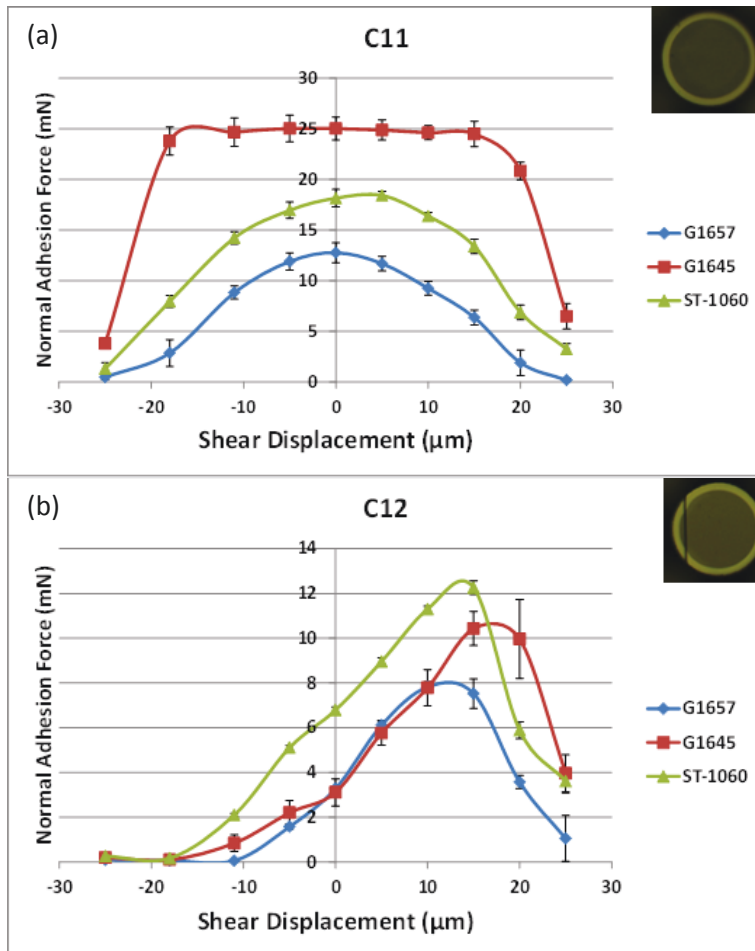


Figure 5.9: Normal adhesion force against shear displacement compared between (a) C₁₁ and (b) C₁₂ samples made with different materials: Kraton G1657, Kraton G1645 and ST-1060 polyurethane.

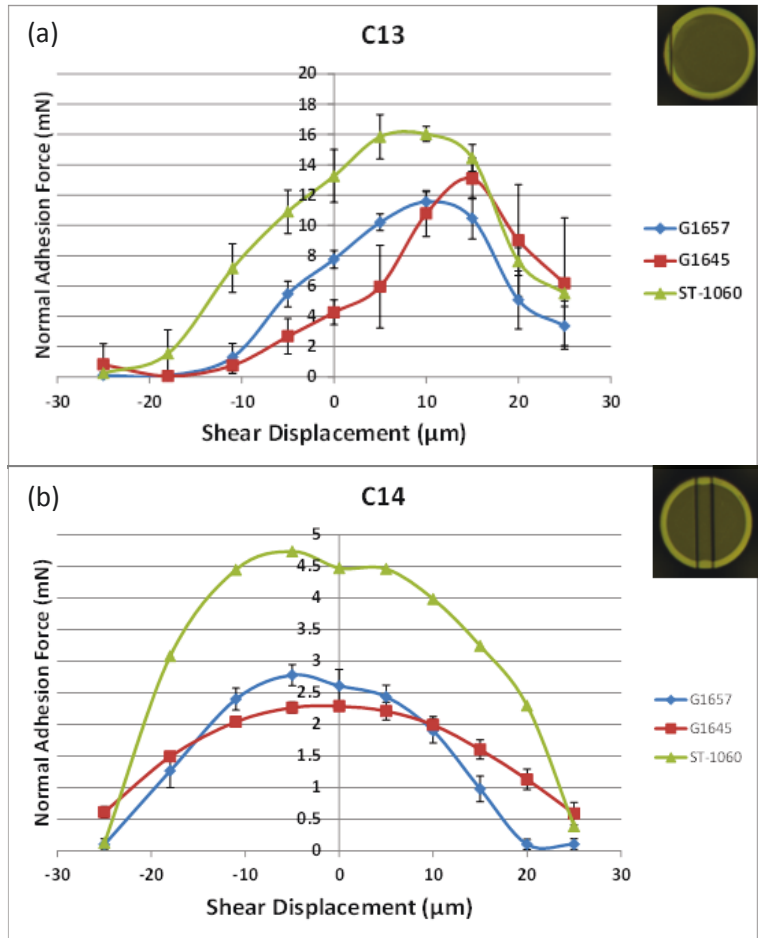


Figure 5.10: Normal adhesion force against shear displacement compared between (a) C₁₃ and (b) C₁₄ samples made with different materials: Kraton G1657, Kraton G1645 and ST-1060 polyurethane.

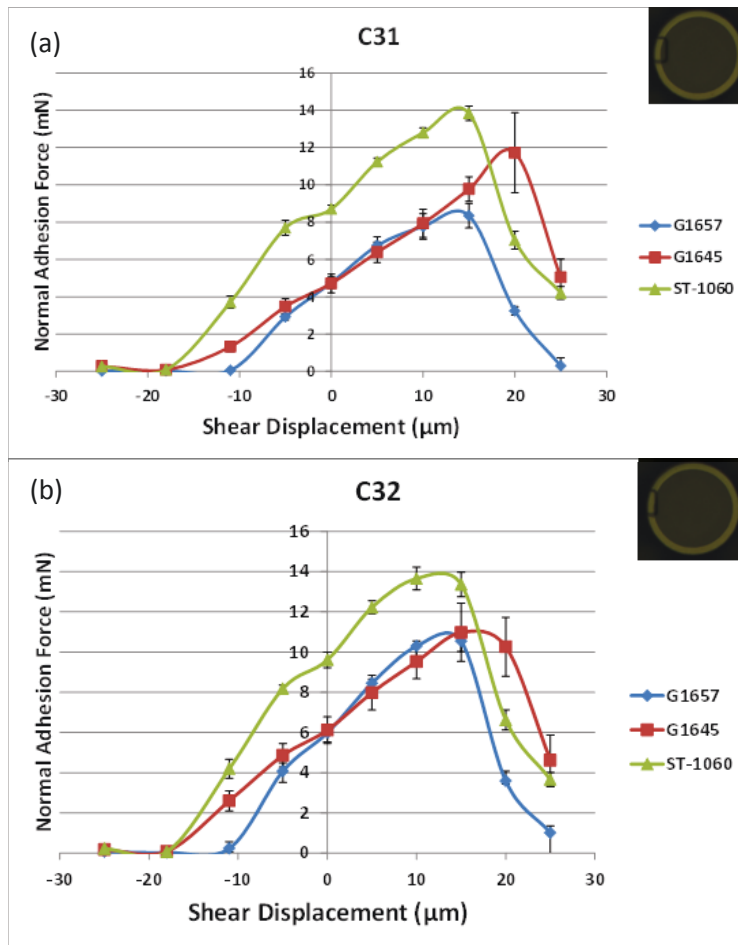


Figure 5.11: Normal adhesion force against shear displacement compared between (a) C₃₁ and (b) C₃₂ samples made with different materials: Kraton G1657, Kraton G1645 and ST-1060 polyurethane.

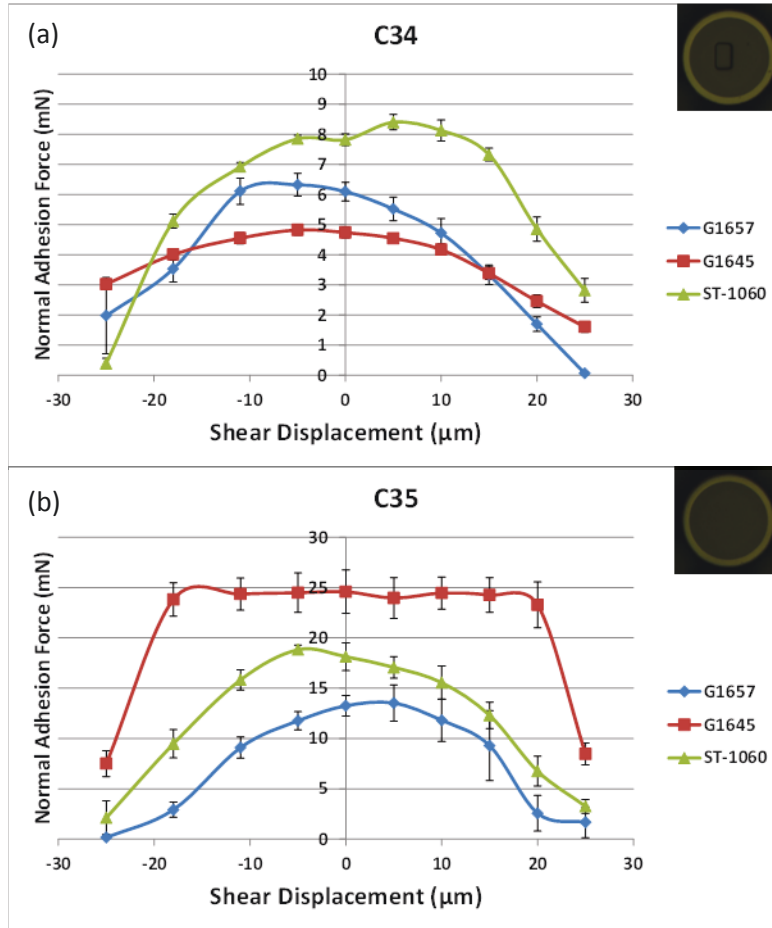


Figure 5.12: Normal adhesion force against shear displacement compared between (a) C_{34} and (b) C_{35} samples made with different materials: Kraton G1657, Kraton G1645 and ST-1060 polyurethane.

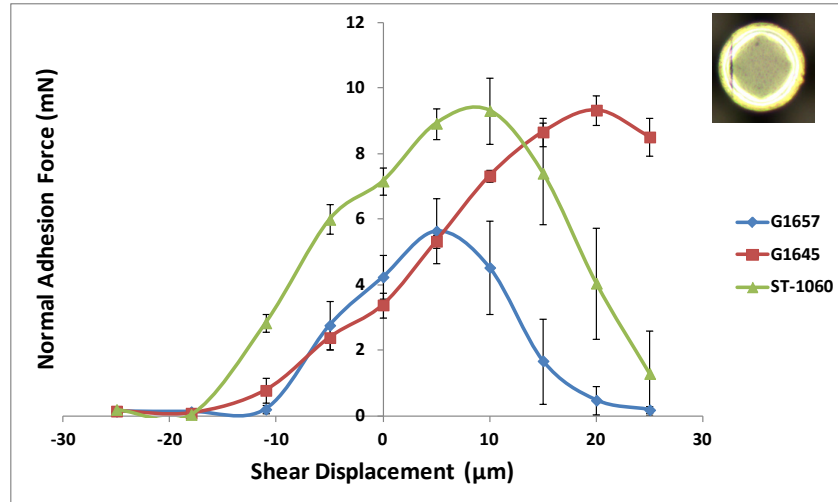


Figure 5.13: Normal adhesion force vs. shear displacement of the hot-embossed W3 adhesive prepared with different materials.

From **Figure 5.9(a)** and **Figure 5.12(b)**, it can be observed that Kraton G1645 isotropic adhesives performed better than that of Kraton G1657 or ST-1060 Polyurethane. Interestingly, the G1645 fibers did not show any significant decline in the adhesion up to a 15 μm shear displacement in either direction, which is not very common for isotropic adhesives, whereas Kraton G1657 and ST-1060 showed a more noticeable decline in adhesion when sheared to either side. It is possible that the softer backing layer aided in reducing the shear sensitivity in this case because if it shifted over, there would be lower stress concentrations in the fibers themselves. In case of the directional fibers, for bar-like defects (C_{12} in **Figure 5.9b** and C_{13} in **Figure 5.10a**) and rectangular defects (C_{31} in **Figure 5.11d**), ST-1060 fibers displayed the greatest maximum adhesion, trailed closely by the G1645 fibers. As expected, the caps with rectangular edge defects showed stronger adhesion than the caps with bar-like defects for all structural materials. The area of the non-contacting defect surface is less for the rectangular defects as compared

to the bar-like defects, resulting in more contact area and consequently stronger adhesion. Kraton G1657 fibers showed the least adhesion in both cases.

The Kraton G1645 fibers seemed to be more susceptible to cap defects, shown by a greater decline in the maximum adhesion force in the presence of a defect (~80 % reduction in adhesion from C_{11} to C_{34} , as compared to ~55 % reduction for ST-1060 and ~50 % reduction for G1657).

The adhesion results in **Figure 5.13** comparing the hot-embossed W3 adhesives shows that the Kraton G1645 sticks almost the same amount as their ST-1060 counterparts, but with much greater anisotropy. These observations clearly demonstrate that Kraton G1645 is the material of choice here if thermoplastics are used for the mass manufacture of these adhesives.

5.5.1. Durability comparison between Kraton and polyurethane samples

One aspect of these materials that will be vital for understanding their long term performance is how much the adhesion may change over time. Many other investigations into this phenomenon have shown that pristine samples will frequently lose a large portion of their initial adhesion force with repeated preloads [123-125]. Many times, this is attributed to fiber collapse, fiber contamination (via dirt/dust) or oligomer transfer. For our trials, fiber collapse is much less of an issue due to the low aspect ratio, dust is minimal in the test environment, and oligomers are unlikely to transfer given our results in section 5.2.

The C_2 versions of the Kraton SEBS and polyurethane adhesives were tested for 500 cycles with three different shear displacements corresponding to minimum adhesion,

adhesion at zero shear, and maximum adhesion in order to determine and compare the useful life cycle of the adhesives. Trials were cycled with 50 displacements at each shear distance (to produce a high, medium and low adhesion force) and repeated ten times. These show that multiple displacements in a single direction can influence the subsequent behavior of trials in the opposite direction if enough elongation or plastic deformation occurs. There was approximately 1 minute of time between each data point. The results are plotted in **Figure 5.14**. The Kraton G1657 showed less stable adhesion behavior immediately after the shear displacements change direction. In the case of the ST-1060 and the G1645, there is a noticeable repeating pattern every 50 cycles in **Figure 5.14** (a-c), which was the number the test system was setup to do before repeating. The cause is likely some plastic deformation of the fibers in a specific direction, which then gets reversed over several cycles once the shear displacement is reversed. Given that the adhesion tests were all designed to be the exact same location, then the likelihood of any particulate contamination, or tests on defective areas are mostly ruled out as the cause of the variable adhesion. The G1657 adhesive shows the most variation across the trials, with first an increase and then a decrease in the strongest pull direction during the cyclic loading in **Figure 5.14** (b). It was also the only sample that significantly changed adhesion in pure normal loads and in the weak direction, so the hypothesis on this one was that the position of the fibers may have been altered through more severe plastic deformation as the trials continued or altered material properties, resulting in very different adhesion values for all levels of shear displacement. For all materials, if shearing in a single direction is consistent, performance rapidly reaches a plateau and we no longer see the cycle dependent performance. Fortunately, as thermoplastics, G1657 and G1645 may be blended to

provide an excellent mix of material properties in future, or compounded with fillers to provide even better material performance. Based on the raw resins however, the G1645 seems to be the superior choice for long term use.

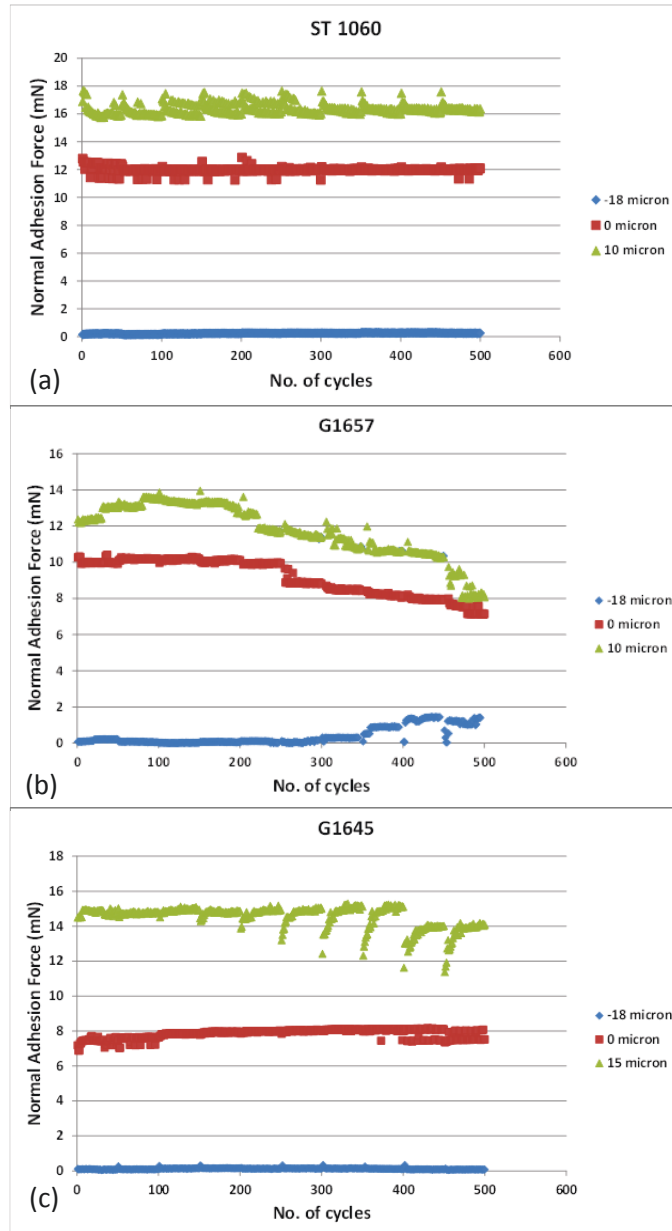


Figure 5.14: Comparison of the durability of the Kraton and polyurethane adhesives of the C₁₃ type: (a)-(c) durability tests with 10 cycles of 50 high-medium-low adhesion trials. The image is published by the author in [128] and is reproduced with permission.

5.5.2: Real time test data:

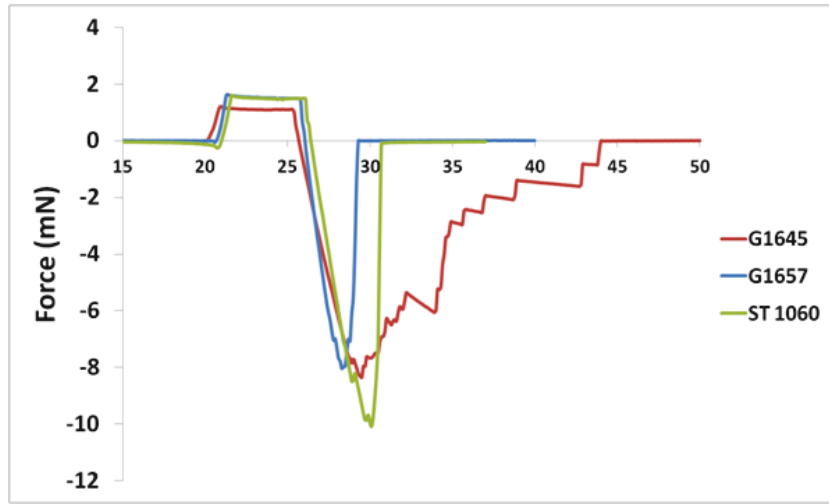


Figure 5.15: Preload (+ve force) and pull-off (-ve force) vs. time for single trials of directional adhesives at a shear displacement of 10 μm away from the defect. The image is published in [126] and is reprinted with permission.

Figure 5.15 shows the consecutive preload and pull-off events for the polyurethane and Kraton adhesives at a shear displacement of 10 μm away from the defect (in the “strong” direction). Despite yielding smaller maximum adhesion for a given preload/drag distance, the thermoplastic elastomers would often show much greater tenacity for individual fibers than ST-1060, resulting in longer pull-off events with stepped detachments. These effects were particularly more pronounced for the G1645 samples, which were the softest material and more naturally “tacky”. The area under the pull-off graph, in **Figure 5.15**, for Kraton G1645 is much larger than that of ST-1060, which means that the adhesion energy or work of adhesion is higher, even though the maximum pull-off force is slightly lower for Kraton G1645 as compared to ST-1060.

Kraton G1657 and G1645 has similar polystyrene content (12.3-14.3 % for G1657 [122] and 11.5-13.5 % for G1645 [121]), so the inherent surface energy should be similar for

both materials. Hence the large difference in adhesion performance could probably be attributed to the difference in viscoelastic properties. To test the difference in apparent work of adhesion between the two SEBS materials, a methodology similar to what presented in Lakhera et al. [118] is followed: Preload-Pull off tests are carried out on smooth, unstructured surfaces of both materials. The results, plotted in **Figure 5.16**, shows that both Kraton G1657 and G1645 show viscoelastic relaxing during the 3 second hold time of the preload. According to Lakhera et al. [118], if viscoelastic effects are presented, the apparent of effective work of adhesion is given by:

$$W_{a, \text{eff}} = \frac{2P}{3\pi R^*} \quad (20)$$

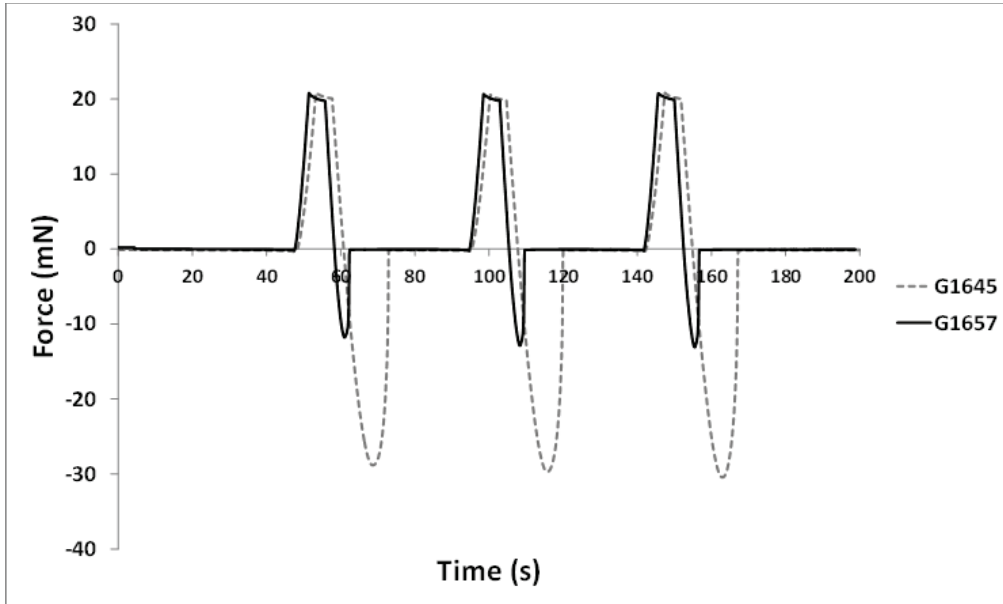


Figure 5.16: Preload (+ve force) and pull-off (-ve force) vs. time graph from three consecutive adhesion test trials on smooth, unstructured SEBS (Kraton G1645 and G1657) samples. Probe velocity was $5 \mu\text{m/s}$ and the hold time at preload of 20 mN was 3 s.

where P is the experimental pull-off force and R^* is the effective contact radius.

Assuming the contact radius is the same during for both Kraton G1645 and G1657 trials, the ratio of effective work of adhesion between G1645 and G1657 samples is essentially

the ratio of experimental pull-off force, which means the effective work of adhesion of G1645 is approximately 2.5 times ($\sim 30/12$) that of G1657.

5.6 Conductive thermoplastic elastomers:

Attempts have been made to fabricate the dry adhesives with conductive thermoplastic elastomers (Dryflex C3 6068, Elastope) using thermo-compression molding, as shown in **Figure 5.17**.

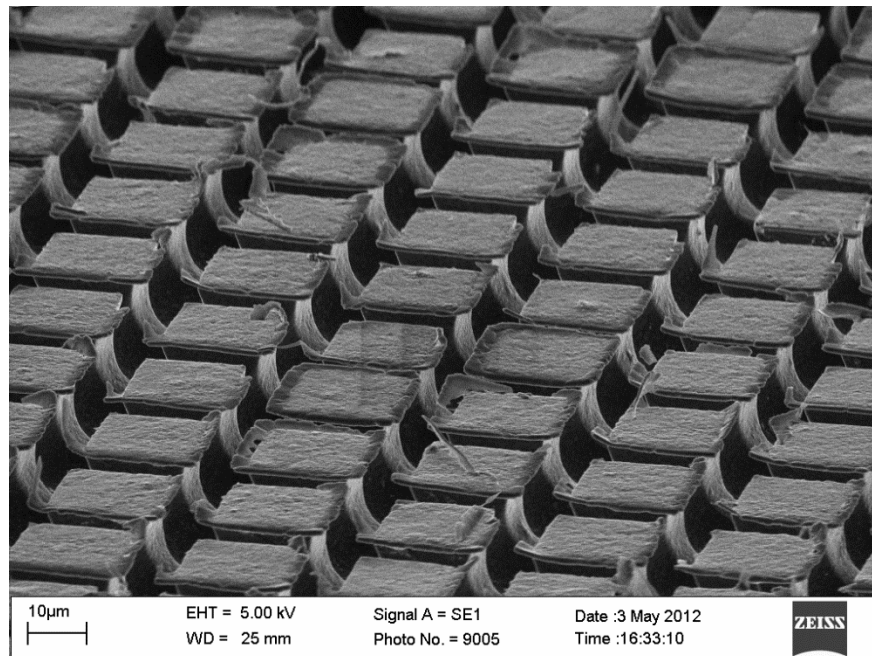


Figure 5.17: Dryflex fibers showing incomplete cap filling and rough cap surfaces. The dryflex material has carbon black fillers in the thermoplastic elastomer matrix.

Upon hot-embossing, the dryflex material left residues and it was very difficult to produce fibers with smooth surfaces, as shown in **Figure 5.17**. A mixture of Kraton G1657 and Dryflex C3 6068 produced better results in terms of fiber surface roughness,

as shown in **Figure 5.18**, but the uniformity in carbon black concentration was not good, shown by random white spots. A thermoplastic compounder is likely required to properly mix two thermoplastic elastomer variations in order to achieve uniformity in properties of the mixture product.

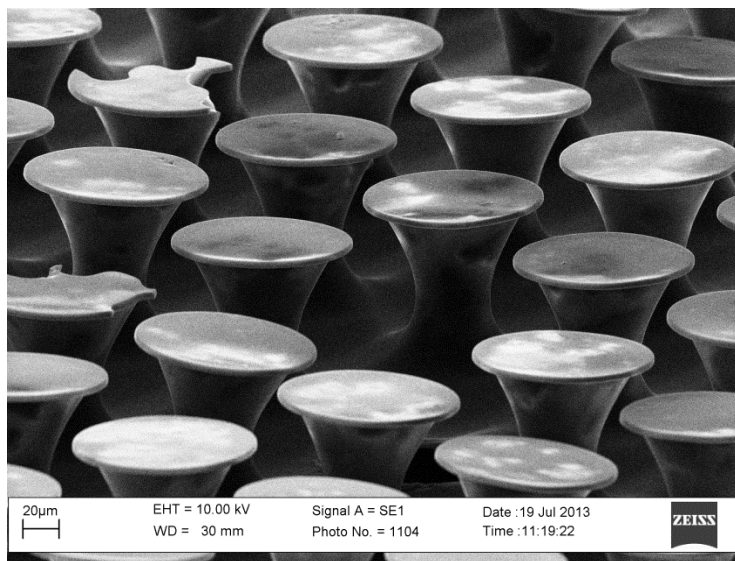


Figure 5.18: Mushroom shaped fibers made from a mixture of Kraton G1657 and Dryflex C3 6068. The white spots are due to non-uniform concentration of carbon black particles in the mixture.

To summarize, this chapter demonstrated the manufacturing of mushroom shaped adhesive fibers by thermo-compression molding using Kraton SEBS elastomers, a process which takes significantly less time compared to the conventional casting method using thermoset polymers. Surface contamination experiments using X-ray Photoelectron Spectroscopy reveals that Kraton G1657 elastomers transfer minimal amount of oligomers due to contact. Subsequent adhesion testing also shows that a softer version of Kraton (G1645) demonstrates adhesion similar to the polyurethane versions in case of anisotropic fibers and superior in the case of isotropic. With the

added advantage of significantly less base material cost and their non-toxic nature, the thermoplastic elastomers have the potential to be a viable alternative to the thermoset PDMS and polyurethane as an adhesive material. The Kraton SEBS elastomers could be blended with a conductive thermoplastic elastomer using a compounder to produce adhesive fibers with anti-static properties as desirable for large-scale MEMS pick and place, but the concept of simple thermo-compression molding has been demonstrated for multiple thermoplastic materials in this work.

Conclusion

This thesis has focused on two major aspects of developing a controllable adhesive for MEMS pick and place; a simple mechanism by which to fabricate anisotropic dry adhesives through the use of cap defects, and the first investigation of an entirely new class of thermoplastic elastomers for their effectiveness as a structural layer for dry adhesives. For the first part of the thesis, linear beam theory is used for the first time to demonstrate how a defect on the cap surface could produce variable shear-dependent adhesion behavior of the fibers, thus resulting in anisotropy in adhesion. The normal adhesion strength of the fabricated directional adhesives was found to be lower than any non-defective designs, but, when loaded in shear, our best performing adhesives achieve similar maximum normal adhesion strengths to non-defective designs, while maintaining anisotropy. Because this method can be completed on a cap before the production of the rest of the fiber, it represents a significant improvement in the ease of manufacturing and produces significant normal adhesion strength even in the absence of shear loads. Having proven the concept of the deliberate defect, a hot embossing technique was devised for large-scale production of anisotropic adhesives which avoids substrate warping and run-off error issues prevalent with plastic substrates. This will ultimately permit large-scale manufacturing of well-defined anisotropic fibers, but will need further work in future to either eliminate micromasking effects, or preferably avoid RIE entirely through a combined embossing and photo curing process during cap definition.

For the second part of the thesis, SEBS thermoplastic elastomers were introduced and investigated for the first time as a structural material for the mushroom shaped

adhesive fibers. A variation of SEBS thermoplastic elastomer along with PDMS and polyurethane was characterized in terms of oligomer transfer using X-ray Photoelectron Spectroscopy. For both polyurethane thermosetting rubbers and SEBS thermoplastic elastomers, this thesis presents the first investigation on relative oligomer transfer onto a representative bond pad material (gold). Both polyurethane and PDMS appear to transfer oligomers upon contact with a gold-coated surface, with PDMS transferring relatively more than the polyurethane. The SEBS thermoplastic elastomer version tested was found to be less likely to transfer its own oligomers compared to PDMS and polyurethane, and cross contamination with PDMS oligomers has been observed for the case of both polyurethane and the SEBS thermoplastic elastomer. However, even the relatively high contaminating PDMS did not seem to affect initial thermosonic ball bonding yields, thus rendering these materials suitable for integration of dry adhesives into MEMS pick and place systems. A simple and scalable thermo-compression molding system was used to fabricate mushroom shaped fibers directly from a silicone rubber mold in a few minutes, rather than hours. Two variations of thermoplastic elastomer dry adhesives were compared with a thermoset polyurethane counterpart, with one of them showing comparable or better performance in both isotropic and anisotropic performance. With the advantage of faster processing time, lower base material cost, insignificant oligomer transfer, and scalability, the thermo-compression molding of thermoplastic elastomers is a viable technique for the mass production of these mushroom shaped dry adhesives and a suitable alternative to the conventional soft lithographic techniques with thermoset elastomers.

This work has resulted in contributions to two conference articles and two journal publications published or accepted for publication. The adhesives themselves are

capable of being integrated with a variety of end effector tools, and earlier samples of non-directional designs have been provided to collaborators for use in silicon wafer handling. In future, blending different thermoplastics together with fillers will ideally produce thermoplastic dry adhesives with strong adhesion, reliable manufacturing and more durable long term performance. Once best material composition is determined, work can begin on large-scale manufacturing of these directional, gecko inspired adhesives.

Future Works

Future works would include:

- Modifying our adhesion test system to perform direct shear or friction measurement on the isotropic and anisotropic adhesives
- Modify the hot-embossing technique for producing large scale anisotropic adhesive samples to mitigate the surface roughening issue
- Use the ultrasonic bonder or an injection mold to facilitate the fabrication of thermoplastic elastomer adhesives on a larger size and in less time.
- Characterize other variations of commercially available thermoplastic elastomers such as polyolefin blends (TPOs), elastomeric conductive composites, thermoplastic polyurethanes, etc. in producing the dry adhesives with a particular focus on long term durability and lower hysteresis in load-unloading curves.

List of Publications

Journal

- W. B. Khaled and D. Sameoto. Fabrication and characterization of thermoplastic elastomer dry adhesives with high strength and low contamination. *ACS Appl. Mater. Interfaces* 2014. Available: <http://dx.doi.org/10.1021/am500616a>
- W. B. Khaled and D. Sameoto. Anisotropic dry adhesive via cap defects. *Bioinspiration & Biomimetics*, **8**(4), 044002, 2013. Available: <http://stacks.iop.org/1748-3190/8/i=4/a=044002>.

Conference

- W. B. Khaled and D. Sameoto. Manufacture of mushroom shaped dry adhesives by thermo-compression molding of thermoplastic elastomers. *Proceedings of the Annual Meeting of the Adhesion Society*, 2014. Available at: http://www.adhesionsociety.org/wp-content/uploads/2014_Annual-Meeting/Abstracts/Khaled_2014_Extended_Abstract.pdf
- W. B. Khaled and D. Sameoto. The Deliberate Defect: A Facile Method for Mass Manufacture of Anisotropic Dry Adhesives. *Proceedings of the Annual Meeting of the Adhesion Society*, 2013. Available at: https://www.adhesionsociety.org/wp-content/uploads/2013-Annual-Meeting-Abstracts/Khaled_The_2013.pdf

Bibliography

- [1] K. Autumn. Properties, principles, and parameters of the gecko adhesive system. *Biological Adhesives*, Springer, Berlin, 225-256. 2006. Available: http://dx.doi.org/10.1007/978-3-540-31049-5_12.
- [2] K. Autumn, M. Sitti, Y. A. Liang, A. M. Peattie, W. R. Hansen, S. Sponberg, T. W. Kenny, R. Fearing, J. N. Israelachvili and R. J. Full, "Evidence for van der Waals adhesion in gecko setae," *Proceedings of the National Academy of Sciences*, **99**, 12252-12256, September 17, 2002.
- [3] G. Huber, H. Mantz, R. Spolenak, K. Mecke, K. Jacobs, S. N. Gorb and E. Arzt. Evidence for capillarity contributions to gecko adhesion from single spatula nanomechanical measurements. *Proceedings of the National Academy of Sciences of the United States of America*. **102**(45), 16293-16296, 2005. Available: <http://www.pnas.org/content/102/45/16293.abstract>.
- [4] W. Sun, P. Neuzil, T. S. Kustandi, S. Oh and V. D. Samper. The nature of the gecko lizard adhesive force. *Biophysics Journal*, **89**(2), L14-L17, 2005.
- [5] P. H. Niewiarowski, S. Lopez, L. Ge, E. Hagan and A. Dhinojwala. Sticky gecko feet: The role of temperature and humidity. *PLoS ONE*, **3**(5), 2192, 2008. Available: <http://dx.plos.org/10.1371/journal.pone.0002192>.
- [6] J. B. Puthoff, M. S. Prowse, M. Wilkinson and K. Autumn. Changes in materials properties explain the effects of humidity on gecko adhesion. *The Journal of Experimental Biology*, **213**(21), 3699-3704, 2010.
- [7] M. S. Prowse, M. Wilkinson, J. B. Puthoff, G. Mayer and K. Autumn. Effects of humidity on the mechanical properties of gecko setae. *Acta Biomaterialia*, **7**(2), 733-738. 2011.
- [8] J. N. Israelachvili. *Intermolecular and Surface Forces*, 3rd edition, Elsevier, 2011.
- [9] J. Kwak and T. Kim. A review of adhesion and friction models for gecko feet. *International Journal of Precision Engineering and Manufacturing*, **11**(1), 171-186. 2010. Available: <http://dx.doi.org/10.1007/s12541-010-0020-5>.
- [10] R. S. Bradley. LXXIX. the cohesive force between solid surfaces and the surface energy of solids. *Philosophical Magazine Series 7*, **13**(86), 853-862. 1932. Available: <http://www.tandfonline.com/doi/abs/10.1080/14786449209461990>.
- [11] H. Hertz. On the contact of elastic solids. *J.Reine Angew.Math*, **92**(156-171), 110. 1881.

- [12] K. L. Johnson, K. Kendall and A. D. Roberts. Surface energy and the contact of elastic solids. *Proceedings of the Royal Society of London. A. Mathematical and Physical Sciences*, **324**(1558), 301-313. 1971.
- [13] D. Tabor. Surface forces and surface interactions. *Journal of Colloid Interface Science*, **58**(1), 2-13. 1977.
- [14] V. M. Muller, V. S. Yushchenko and B. V. Derjaguin. On the influence of molecular forces on the deformation of an elastic sphere and its sticking to a rigid plane. *Journal of Colloid Interface Science*, **77**(1), 91-101. 1980.
- [15] B. V. Derjaguin, V. M. Muller and Y. P. Toporov. Effect of contact deformations on the adhesion of particles. *Journal of Colloid Interface Science*, **53**(2), 314-326. 1975.
- [16] D. Maugis. Adhesion of spheres: The JKR-DMT transition using a dugdale model. *Journal of Colloid Interface Science*, **150**(1), 243-269, 1992.
- [17] Y. - Zhao, L. S. Wang and T. X. Yu. Mechanics of adhesion in MEMS—a review. *Journal of Adhesion Science and Technology*, **17**(4), 519-546. 2003. Available: <http://dx.doi.org/10.1163/15685610360554393>.
- [18] R. Spolenak, S. Gorb, H. Gao and E. Arzt. Effects of contact shape on the scaling of biological attachments. *Proceedings of the Royal Society A: Mathematical, Physical and Engineering Science*, **461**(2054), 305-319. 2005.
- [19] K. Kendall. The adhesion and surface energy of elastic solids. *Journal of Physics D: Applied Physics*, **4**(8), 1186, 1971. Available: <http://stacks.iop.org/0022-3727/4/i=8/a=320>.
- [20] M. Kamperman, E. Kroner, A. Del Campo, R. M. McMeeking and E. Arzt. Functional adhesive surfaces with "gecko" effect: The concept of contact splitting. *Advanced Engineering Materials*, **12**(5), 335-348, 2010. Available: <http://dx.doi.org/10.1002/adem.201000104>.
- [21] H. Gao, X. Wang, H. Yao, S. Gorb and E. Arzt. Mechanics of hierarchical adhesion structures of geckos. *Mechanics of Materials*, **37**(2-3), 275-285, 2005. Available: <http://dx.doi.org/10.1016/j.mechmat.2004.03.008>.
- [22] K. Kendall. Thin-film peeling-the elastic term. *Journal of Physics D: Applied Physics*, **8**(13), 1449, 1975. Available: <http://stacks.iop.org/0022-3727/8/i=13/a=005>.
- [23] K. Autumn. Gecko adhesion: Structure, function, and applications. *MRS Bulltin*, **32**(6), 473-478, 2007.
- [24] K. Jin, Y. Tian, J. S. Erickson, J. Puthoff, K. Autumn and N. S. Pesika. Design and fabrication of Gecko-inspired adhesives. *Langmuir*, **28**, 5737-5742, 2012.

- [25] K. Autumn and W. Hansen. Ultrahydrophobicity indicates a non-adhesive default state in gecko setae. *Journal of Comparative Physiology A*, **192**(11), 1205-1212, 2006. Available: <http://dx.doi.org/10.1007/s00359-006-0149-y>.
- [26] N. W. Rizzo, K. H. Gardner, D. J. Walls, N. M. Keiper-Hrynko, T. S. Ganzke and D. L. Hallahan. *Journal of the Royal Society Interface*, **3**(8), 441-451, 2006.
- [27] B. Zhao, N. Pesika, H. Zeng, Z. Wei, Y. Chen, K. Autumn, K. Turner and J. Israelachvili. Role of tilted adhesion fibrils (setae) in the adhesion and locomotion of gecko-like systems. *The Journal of Physical Chemistry B*, **113**(12), 3615-3621, 2009. Available: <http://dx.doi.org/10.1021/jp806079d>.
- [28] K. Autumn, Y. A. Liang, S. T. Hsieh, W. Zesch, W. P. Chan, T. W. Kenny, R. Fearing and R. J. Full. Adhesive force of a single gecko foot-hair. *Nature*, **405**(6787), 681-685, 2000. Available: <http://dx.doi.org/10.1038/35015073>.
- [29] B. Zhao, N. Pesika, K. Rosenberg, Y. Tian, H. Zeng, P. McGuiggan, K. Autumn and J. Israelachvili. Adhesion and friction force coupling of gecko setal arrays: implications for structured adhesive surfaces. *Langmuir*, **24**(4), 1517-1524, 2008. Available: <http://dx.doi.org/10.1021/la702126k>.
- [30] K. Autumn, A. Dittmore, D. Santos, M. Spenko and M. Cutkosky. Frictional adhesion: A new angle on gecko attachment. *Journal of Experimental Biology*, **209**(18), 3569-3579, 2006.
- [31] J. Lee, R. S. Fearing and K. Komvopoulos. Directional adhesion of gecko-inspired angled microfiber arrays. *Applied Physics Letters*, **93**(19), 191910, 2008. Available: <http://dx.doi.org/10.1063/1.3006334>.
- [32] H. E. Jeong, J. Lee, H. N. Kim, S. H. Moon and K. Y. Suh. A nontransferring dry adhesive with hierarchical polymer nanohairs. *Proceedings of the National Academy of Sciences*, **106**(14), 5639-5644, 2009. Available: <http://www.pnas.org/content/106/14/5639.abstract>.
- [33] M. K. Kwak, H. E. Jeong, W. G. Bae, H. Jung and K. Y. Suh. Anisotropic adhesion properties of triangular-tip-shaped micropillars. *Small*, **7**(16), 2296-2300, 2011. Available: <http://dx.doi.org/10.1002/sml.201100455>.
- [34] M. P. Murphy, B. Aksak and M. Sitti. Gecko-inspired directional and controllable adhesion. *Small*, **5**(2), 170-175, 2009. Available: <http://dx.doi.org/10.1002/sml.200801161>.
- [35] S. Kim, M. Spenko, S. Trujillo, B. Heyneman, D. Santos and M. R. Cutkosky. Smooth vertical surface climbing with directional adhesion. *IEEE Transactions on Robotics*, **24**(1), 65-74, 2008. Available: <http://dx.doi.org/10.1109/TRO.2007.909786>.

- [36] J. Tamelier, S. Chary and K. L. Turner, "Vertical anisotropic microfibers for a gecko-inspired adhesive," *Langmuir*, **28**, 8746-8752, 2012.
- [37] D. Sameoto, H. Sharif, J. P. Díaz Téllez, B. Ferguson and C. Menon. Nonangled anisotropic elastomeric dry adhesives with tailorable normal adhesion strength and high directionality. *Journal of Adhesion Science and Technology*, **28**(3-4), 1-13, 2012. Available: <http://dx.doi.org/10.1080/01694243.2012.693809>.
- [38] M. Moon, T. Cha, K. Lee, A. Vaziri and H. Kim. Tilted janus polymer pillars. *Soft Matter*, **6**(16), 3924-3929, 2010. Available: <http://dx.doi.org/10.1039/c0sm00126k>.
- [39] M. Zhou, K. Liu, J. Wan, X. Li, K. Jiang, H. Zeng, X. Zhang, Y. Meng, S. Wen, H. Zhu and Y. Tian. Anisotropic interfacial friction of inclined multiwall carbon nanotube array surface. *Carbon*, **50**(15), 5372-5379, 2012. Available: <http://www.sciencedirect.com/science/article/pii/S000862231200601X>.
- [40] D. Sameoto and C. Menon. Direct molding of dry adhesives with anisotropic peel strength using an offset lift-off photoresist mold, *Journal of Micromechanics and Microengineering*, **19**(11), 115026, 2009.
- [41] P. L. Dickrell, S. B. Sinnott, D. W. Hahn, N. R. Raravikar, L. S. Schadler, P. M. Ajayan and W. G. Sawyer. Frictional anisotropy of oriented carbon nanotube surfaces. *Tribology Letters*, **18**(1), 59-62, 2005. Available: <http://dx.doi.org/10.1007/s11249-004-1752-0>.
- [42] L. Ge, S. Sethi, L. Ci, P. M. Ajayan and A. Dhinojwala. Carbon nanotube-based synthetic gecko tapes. *Proceedings of the National Academy of Sciences*, **104**(26), 10792-10795. 2007.
- [43] R. T. Pack, J. L. Christopher Jr. and K. Kawamura. A rubber-tuator-based structure-climbing inspection robot. *Proceedings of IEEE International Conference on Robotics and Automation*, 1997.
- [44] T. Yano, T. Suwa, M. Murakami and T. Yamamoto. Development of a semi self-contained wall climbing robot with scanning type suction cups. *Proceedings of the IEEE/RSJ International Conference on Intelligent Robots and Systems*, 1997.
- [45] A. Nagakubo and S. Hirose. Walking and running of the quadruped wall-climbing robot. *Proceedings of IEEE International Conference on Robotics and Automation*, 1994 .
- [46] G. La Rosa, M. Messina, G. Muscato and R. Sinatra. A low-cost lightweight climbing robot for the inspection of vertical surfaces. *Mechatronics*, **12**(1), 71-96, 2002.
- [47] J. Zhu, D. Sun and S. Tso. Development of a tracked climbing robot. *Journal of Intelligent and Robotic Systems*, **35**(4), 427-443, 2002. Available: <http://dx.doi.org/10.1023/A%3A1022383216233>.

- [48] A. Parness, T. Hilgendorf, P. Daniel, M. Frost, V. White and B. Kennedy. Controllable ON-OFF adhesion for earth orbit grappling applications. *Proceedings of IEEE Aerospace Conference*, 2013.
- [49] K. Daltorio, S. Gorb, A. Peressadko, A. Horchler, R. Ritzmann and R. Quinn. "A robot that climbs walls using micro-structured polymer feet," *Proceedings of the 8th International Conference on Climbing and Walking Robots and the Support Technologies for Mobile Machines*, 2006. Available: http://dx.doi.org/10.1007/3-540-26415-9_15.
- [50] E. W. Hawkes, E. V. Eason, A. T. Asbeck and M. R. Cutkosky. The gecko's toe: Scaling directional adhesives for climbing applications. *IEEE Xplore*, **18**(2), 2012. Available: <http://dx.doi.org/10.1109/TMECH.2012.2209672>.
- [51] C. Menon, M. Murphy and M. Sitti. Gecko inspired surface climbing robots. *Proceedings of IEEE International Conference on Robotics and Biomimetics*, 2004.
- [52] B. Aksak, M. P. Murphy and M. Sitti. Gecko inspired micro-fibrillar adhesives for wall climbing robots on micro/nanoscale rough surfaces. *Proceedings of IEEE International Conference on Robotics and Automation*, 2008.
- [53] M. Henrey, J. Krahn, A. Ahmed, K. Wormnes and C. Menon. Climbing with structured dry adhesives: sticky robots for scaling smooth vertical surfaces, *Proceedings of ASTRA 13*, 2013.
- [54] Y. Menguc, S. Y. Yang, S. Kim, J. A. Rogers and M. Sitti. Gecko-inspired controllable adhesive structures applied to micromanipulation. *Advanced Functional Materials*, **22**(6), pp. 1246-1254. 2012. Available: <http://dx.doi.org/10.1002/adfm.201101783>.
- [55] A. Carlson, H. Kim-Lee, J. Wu, P. Elvikis, H. Cheng, A. Kovalsky, S. Elgan, Q. Yu, P. M. Ferreira, Y. Huang, K. T. Turner and J. A. Rogers. Shear-enhanced adhesiveless transfer printing for use in deterministic materials assembly. *Applied Physics Letters*, **98**(26), 2011. Available: <http://dx.doi.org/10.1063/1.3605558>.
- [56] S. Kim, J. Wu, A. Carlson, S. H. Jin, A. Kovalsky, P. Glass, Z. Liu, N. Ahmed, S. L. Elgan, W. Chen, P. M. Ferreira, M. Sitti, Y. Huang and J. A. Rogers. Microstructured elastomeric surfaces with reversible adhesion and examples of their use in deterministic assembly by transfer printing. *Proceedings of the National Academy of Sciences*, **107**(40), 17095-17100, 2010.
- [57] S. Y. Yang, A. Carlson, H. Cheng, Q. Yu, N. Ahmed, J. Wu, S. Kim, M. Sitti, P. M. Ferreira, Y. Huang and J. A. Rogers. Elastomer surfaces with directionally dependent adhesion strength and their use in transfer printing with continuous roll-to-roll applications. *Advanced Materials*, **24**(16), 2117-2122. 2012. Available: <http://dx.doi.org/10.1002/adma.201104975>.
- [58] Ferguson, B. J. Improved Gecko Inspired Dry Adhesives Applied to the Packaging of MEMS. MSc Thesis, University of Alberta, Edmonton, Canada, 2013..

- [59] M. K. Kwak, H. Jeong and K. Y. Suh. Rational design and enhanced biocompatibility of a dry adhesive medical skin patch. *Adv Mater* 23(34), pp. 3949-3953, 2011. Available: <http://dx.doi.org/10.1002/adma.201101694>.
- [60] D. Sameoto and C. Menon, Deep UV patterning of acrylic masters for molding biomimetic dry adhesives, *Journal of Micromechanics and Microengineering*, **20**, 115037, 2010.
- [61] D. Sameoto and B. Ferguson. Robust large-area synthetic dry adhesives. *Journal of Adhesion Science and Technology*, **28**(3-4), 1-17, 2012. Available: <http://dx.doi.org/10.1080/01694243.2012.693802>.
- [62] G. Carbone, E. Pierro and S. N. Gorb. Origin of the superior adhesive performance of mushroom-shaped microstructured surfaces. *Soft Matter*, **7**(12), 5545-5552, 2010.
- [63] G. Carbone and E. Pierro. A review of adhesion mechanisms of mushroom-shaped microstructured adhesives. *Meccanica*, **48**(8), 1819-1833, 2013. Available: <http://dx.doi.org/10.1007/s11012-013-9724-9>.
- [64] A. V. Spuskanyuk, R. M. McMeeking, V. S. Deshpande and E. Arzt. The effect of shape on the adhesion of fibrillar surfaces. *Acta Biomaterialia*, **4**(6), 1669-1676, 2008. Available: <http://www.sciencedirect.com/science/article/pii/S1742706108001645>.
- [65] Walid Bin Khaled and Dan Sameoto. Anisotropic dry adhesive via cap defects. *Bioinspiration & Biomimetics*, **8**(4), 044002, 2013. Available: <http://stacks.iop.org/1748-3190/8/i=4/a=044002>.
- [66] Juvinall R C and Marshek K M, *Fundamentals of Machine Component Design*. New York: Wiley, 1991.
- [67] Thomson W T and Dahleh M D, *Theory of Vibrations with Application*. New Jersey: Prentice Hall, 1998.
- [68] D. Paretkar, M. Kamperman, D. Martina, J. Zhao, C. Creton, A. Lindner, A. Jagota, R. McMeeking and E. Arzt. Preload-responsive adhesion: Effects of aspect ratio, tip shape and alignment. *Journal of the Royal Society Interface*, **10**(83), 2013. Available: <http://dx.doi.org/10.1098/rsif.2013.0171>.
- [69] D. Sameoto. Dry adhesives for MEMS assembly, manipulation and integration: Progress and challenges. *Proceedings of 5th International Symposium on Dielectrics for Nanosystems: Materials Science, Processing, Reliability and Manufacturing*, 2012. Available: <http://dx.doi.org/10.1149/1.3700916>.
- [70] M Haiducu and M Rahbar and I G Foulds and R W Johnstone and D Sameoto and M. Parameswaran. Deep-UV patterning of commercial grade PMMA for low-cost, large-scale microfluidics. *Journal of Micromechanics and Microengineering*, **18**(11), 115029, 2008. Available: <http://stacks.iop.org/0960-1317/18/i=11/a=115029>.

- [71] D. Sameoto, Y. Li and C. Menon. Micromask generation for polymer morphology control: Nanohair fabrication for synthetic dry adhesives. *Proceedings of 3rd International Conference on Smart Materials, Structures and Systems - Smart Materials and Micro/Nanosystems*, 2008.
- [72] B. Kim, S. Lee, J. Lee, S. Cho, H. Park, S. Yeom and S. Park. A comparison among neo-hookean model, mooney-rivlin model, and ogden model for chloroprene rubber. *International Journal of Precision Engineering and Manufacturing*, **13**(5), pp. 759-764, 2012. Available: <http://dx.doi.org/10.1007/s12541-012-0099-y>.
- [73] A. Ali, M. Hosseini and B. B. Sahari. A review of constitutive models for rubber-like materials. *American Journal of Engineering and Applied Sciences*, **3**(1), 232-9, 2010. Available: <http://dx.doi.org/10.3844/ajeassp.2010.232.239>.
- [74] Bscheiden B, Ferguson B and Sameoto D, Hyperelastic simulation for accurate prediction of gecko inspired dry adhesive deformed shape and stress distribution prior to detachment, *Proceedings of the Annual Meeting of the Adhesion Society*, 2013.
- [75] G. Carbone, E. Pierro and S. N. Gorb. Origin of the superior adhesive performance of mushroom-shaped microstructured surfaces. *Soft Matter*, **7**(12), 5545-5552, 2011. Available: <http://dx.doi.org/10.1039/C0SM01482F>.
- [76] Spuskanyuk, A.V.; McMeeking, R.M.; Deshpande, V.S.; Arzt, E. The effect of shape on the adhesion of fibrillar adhesives; *Acta Biomaterialia*, **4**(6), 1669-1676, 2008.
- [77] H. Gao and H. Yao. Shape insensitive optimal adhesion of nanoscale fibrillar structures. *Proceedings of the National Academy of Sciences of the United States of America*, **101**(21), 7851-7856. 2004.
- [78] D. Sameoto and C. Menon, "Recent advances in the fabrication and adhesion testing of biomimetic dry adhesives," *Smart Materials and Structure*, **19**(10), 2010.
- [79] B. Aksak, M. P. Murphy and M. Sitti. Adhesion of biologically inspired vertical and angled polymer microfiber arrays. *Langmuir*, **23**(6), 3322-3332, 2007. Available: <http://dx.doi.org/10.1021/la062697t>.
- [80] BJB Enterprises. ST-1060 A/B Data Sheet. <http://www.bjbenterprises.com/pdf/ST-1060.pdf>; Date accessed: March 23 2014.
- [81] M. B. Ranade. Adhesion and removal of fine particles on surfaces. *Aerosol Science and Technology*, **7**(2), 161-176. 1987.
- [82] S. Kim, A. Carlson, H. Cheng, S. Lee, Jung-Ki Park, Y. Huang and J. A. Rogers. Enhanced adhesion with pedestal-shaped elastomeric stamps for transfer printing. *Applied Physics Letters*, **100**(17), 171909, 2012. Available: <http://dx.doi.org/10.1063/1.4706257>.

- [83] A. Carlson, H. Kim-Lee, J. Wu, P. Elvikis, H. Cheng, A. Kovalsky, S. Elgan, Q. Yu, P. M. Ferreira, Y. Huang, K. T. Turner and J. A. Rogers. Shear-enhanced adhesiveless transfer printing for use in deterministic materials assembly. *Applied Physics Letters*, **98**(26), 2011. Available: <http://dx.doi.org/10.1063/1.3605558>.
- [84] D. Sameoto. Dry adhesives for MEMS assembly, manipulation and integration: Progress and challenges. *Proceedings of 5th International Symposium on Dielectrics for Nanosystems: Materials Science, Processing, Reliability and Manufacturing*, 2012. Available: <http://dx.doi.org/10.1149/1.3700916>.
- [85] D. Sameoto and C. Menon; A low-cost, high-yield fabrication method for producing optimized biomimetic dry adhesives, *J Micromech Microengineering*, **19**, 115002, 2009.
- [86] Y. Li, D. Sameoto and C. Menon. Properties validation of an anisotropic dry adhesion designed for legged climbing robots, *Proceedings of IEEE International Conference on Robotics and Biomimetics*, 1906-1911, 2009.
- [87] C. Greiner, E. Arzt and A. del Campo. Hierarchical Gecko-like adhesives, *Advanced Materials*, **21**(4), 479-482, 2009.
- [88] A. Parness, D. Soto, N. Esparza, N. Gravish, M. Wilkinson, K. Autumn and M. Cutkosky. *Journal of the Royal Society Interface*, **6**(41), 1223-1232.
- [89] S. Vajpayee, R. Long, L. Shen, A. Jagota and C. Hui. Effect of rate on adhesion and static friction of a film-terminated fibrillar interface. *Langmuir*, **25**(5), 2765-2771. 2009. Available: <http://dx.doi.org/10.1021/la8033885>.
- [90] E. Cheung and M. Sitti. Adhesion of biologically inspired polymer microfibers on soft surfaces. *Langmuir*, **25**(12), 6613-6616. 2009. Available: <http://dx.doi.org/10.1021/la900997p>.
- [91] S. Kim and M. Sitti. Biologically inspired polymer microfibers with spatulate tips as repeatable fibrillar adhesives. *Applied Physics Letters*, **89** (26), 261911-261913, 2006.
- [92] M. P. Murphy, B. Aksak and M. Sitti. Adhesion and anisotropic friction enhancements of angled heterogeneous micro-fiber arrays with spherical and spatula tips. *Journal of Adhesion Science & Technology*, **21**(12), 1281-1296, 2007.
- [93] Y. Xia and G. M. Whitesides. SOFT LITHOGRAPHY. *Annual Review of Materials Science*, **28**(1), 153-184. 1998. Available: <http://dx.doi.org/10.1146/annurev.matsci.28.1.153>.
- [94] J. Krahn and C. Menon, "Electro-dry-adhesion," *Langmuir*, **28**, 5438-5443, 2012.
- [95] L. Yang, N. Shirahata, G. Saini, F. Zhang, L. Pei, M. C. Asplund, D. G. Kurth, K. Ariga, K. Sautter, T. Nakanishi, V. Smentkowski and M. R. Linford. Effect of surface free energy on PDMS transfer in microcontact printing and its application to ToF-SIMS to probe

surface energies. *Langmuir*, **25**(10), 5674-5683, 2009. Available: <http://dx.doi.org/10.1021/la804272n>.

[96] J. A. Wigenius, M. Hamed and O. Inganäs. Limits to Nanopatterning of Fluids on Surfaces in Soft Lithography, *Advanced Functional Materials*, **18**(17), 2563-2571, 2008.

[97] S. Yunus, D. L. De Crombrughe, C. Poleunis and A. Delcorte. Diffusion of oligomers from polydimethylsiloxane stamps in microcontact printing: Surface analysis and possible application. *Surface Interface Analysis*, **39**(12-13), 922-925, 2007. Available: <http://dx.doi.org/10.1002/sia.2623>.

[98] R. B. A. Sharpe, D. Burdinski, C. D. Van Marel, J. A. J. Jansen, J. Huskens, H. J. W. Zandvliet, D. N. Reinhoudt and B. Poelsema. Ink dependence of poly(dimethylsiloxane) contamination in microcontact printing. *Langmuir*, **22**(13), 5945-5951. 2006. Available: <http://dx.doi.org/10.1021/la053298l>.

[99] K. Glasmastar, J. Gold, A. Andersson, D. S. Sutherland and B. Kasemo. Silicone transfer during microcontact printing. *Langmuir*, **19**(13), 5475-5483, 2003. Available: <http://dx.doi.org/10.1021/la026558x>.

[100] D. J. Graham, D. D. Price and B. D. Ratner. Solution assembled and microcontact printed monolayers of dodecanethiol on gold: A multivariate exploration of chemistry and contamination. *Langmuir*, **18**(5), 1518-1527, 2002. Available: <http://dx.doi.org/10.1021/la010059z>.

[101] I. Böhm, A. Lampert, M. Buck, F. Eisert and M. Grunze. A spectroscopic study of thiol layers prepared by contact printing. *Applied Surface Science*, **141**(3-4), 237-243. 1999.

[102] Y. Zhou, R. Valiokas and B. Liedberg. Structural characterization of microcontact printed arrays of hexa(ethylene glycol)-terminated alkanethiols on gold. *Langmuir*, **20**(15), 6206-6215, 2004. Available: <http://dx.doi.org/10.1021/la049421a>.

[103] B. A. Langowski and K. E. Uhrich. Oxygen plasma-treatment effects on si transfer. *Langmuir*, **21**(14), 6366-6372. 2005. Available: <http://dx.doi.org/10.1021/la046795v>.

[104] N. R. Thomson, C. L. Bower and D. W. McComb. Identification of mechanisms competing with self-assembly during directed colloidal deposition. *Journal of Materials Chemistry*, **18**(21), 2500-2505.

[105] A. Perl, M. Peter, B. J. Ravoo, D. N. Reinhoudt and J. Huskens. Heavyweight dendritic inks for positive microcontact printing. *Langmuir*, **22**(18), 7568-7573. 2006. Available: <http://dx.doi.org/10.1021/la060625w>.

[106] Y. Zhao, M. Li, Q. Lu and Z. Shi. Superhydrophobic polyimide films with a hierarchical topography: Combined replica molding and layer-by-layer assembly. *Langmuir*, **24**(21), 12651-12657, 2008. Available: <http://dx.doi.org/10.1021/la8024364>.

- [107] N. Iyer, N. Saka and Jung-Hoon Chun. Contamination of silicon surface due to contact with solid polymers. *Proceedings of IEEE Transactions on Semiconductor Manufacturing*, **14**, 85-96, 2001.
- [108] D. Trimbach, H. Stapert, J. van Orselen, K. Jandt, C. Bastiaansen and D. Broer. Improved Microcontact Printing of Proteins using Hydrophilic Thermoplastic Elastomers as Stamp Materials. *Advanced Engineering Materials*, **9**(12), 1123-1128, 2007
- [109] A. L. Briseno, M. Roberts, M. Ling, H. Moon, E. J. Nemanick and Z. Bao. Patterning organic semiconductors using Dry[®] poly(dimethylsiloxane) elastomeric stamps for thin film transistors. *Journal of the American Chemical Society*, **128**(12), 3880-3881, 2006. Available: <http://dx.doi.org/10.1021/ja058226v>.
- [110] Z. Yang, A. M. Belu, A. Liebmann-Vinson, H. Sugg and A. Chilkoti. Molecular imaging of a micropatterned biological ligand on an activated polymer surface. *Langmuir*, **16**(19), 7482-7492, 2000. Available: <http://dx.doi.org/10.1021/la0000623>.
- [111] X. Wang, M. Östblom, T. Johansson and O. Inganäs. PEDOT surface energy pattern controls fluorescent polymer deposition by dewetting. *Thin Solid Films*, **449**(1-2), 125-132, 2004.
- [112] B. D. - Ratner and D. G. Castner. *Surface Analysis-The Principle Techniques*, Chapter 2, John Wiley and Sons, 2009
- [113] Vickerman J C and Gilmore I S, *Surface Analysis- the Principal Techniques*. Singapore: Wiley, 2009.
- [114] The NIST reference on constants, units and uncertainty. National Institute of Standards and Technology, Available at: <http://physics.nist.gov/cgi-bin/cuu/Value?h>. Date accessed: March 25, 2014.
- [115] S. Kim, E. Cheung and M. Sitti. Wet self-cleaning of biologically inspired elastomer mushroom shaped microfibrillar adhesives. *Langmuir* **25**(13), pp. 7196-7199. 2009. Available: <http://dx.doi.org/10.1021/la900732h>.
- [116] M. D. Bartlett, A. B. Croll, D. R. King, B. M. Paret, D. J. Irschick and A. J. Crosby. Looking beyond fibrillar features to scale gecko-like adhesion. *Adv Mater* **24**(8), pp. 1078-1083. 2012. Available: <http://dx.doi.org/10.1002/adma.201104191>.
- [117] Nanolab Technologies XPS Binding Energies(BE) and Scofield's Relative Sensitivity Factor (RSF) Chart. Available at: <http://www.nanolabtechnologies.com/pdf/Scofield-Table-of-BEs-and-RSFs.pdf>; Date accessed: March 23 2014.
- [118] N. Lakhera, A. Graucob, A. S. Schneider, E. Kroner, E. Arzt, C. M. Yakacki and C. P. Frick. Effect of viscoelasticity on the spherical and flat adhesion characteristics of photopolymerizable acrylate polymer networks. *International Journal of Adhesion and*

Adhesives. **44**, 184-194. 2013. Available:

<http://www.sciencedirect.com/science/article/pii/S0143749613000456>.

[119] Kraton Performance Polymers Inc Brochure, Kraton Polymers. Available at:

<http://docs.kraton.com/kraton/attachments/downloads/81311AM.pdf>; Date accessed: March 23, 2014.

[120] E. Roy, J. Galas and T. Veres. Thermoplastic elastomers for microfluidics: Towards a high-throughput fabrication method of multilayered microfluidic devices. *Lab Chip* **11**(18), pp. 3193-3196. 2011. Available: <http://dx.doi.org/10.1039/C1LC20251K>.

[121] Kraton Polymers Kraton G1645 M Polymer Data Sheet; Available at:

http://docs.kraton.com/tl_warehouse/pdf_data_docs/WG_4244_WG4F23.tmp.pdf;
Date accessed: March 23, 2014.

[122] Kraton Polymers Kraton G1657 M Polymer Data Sheet. Available at:

http://docs.kraton.com/tl_warehouse/pdf_data_docs/WG_4244_WG93AE.tmp.pdf;
Date accessed: March 23, 2014.

[123] E. Kroner, R. Maboudian and E. Arzt. Adhesion characteristics of PDMS surfaces during repeated pull-off force measurements. *Advanced Engineering Materials*, **12**(5), 398-404, 2010. Available: <http://dx.doi.org/10.1002/adem.201000090>.

[124] J. Davies, S. Haq, T. Hawke and J. P. Sargent. A practical approach to the development of a synthetic gecko tape. *International Journal of Adhesion and Adhesives*, **29**(4), 380-390. 2009. Available:

<http://www.sciencedirect.com/science/article/pii/S0143749608000808>.

[125] M. P. Murphy, S. Kim and M. Sitti. Enhanced adhesion by gecko-inspired hierarchical fibrillar adhesives. *ACS Applied Materials and Interfaces*, **1**(4), 849-855, 2009. Available: <http://dx.doi.org/10.1021/am8002439>.

[126] W. B. Khaled and D. Sameoto. Manufacture of mushroom shaped dry adhesives by thermo-compression molding of thermoplastic elastomers. *Proceedings of the Annual Meeting of the Adhesion Society*, 2014. Available at:

http://www.adhesionsociety.org/wp-content/uploads/2014_Annual-Meeting/Abstracts/Khaled_2014_Extended_Abstract.pdf

[127] W. B. Khaled and D. Sameoto. THE DELIBERATE DEFECT: A FACILE METHOD FOR MASS MANUFACTURE OF ANISOTROPIC DRY ADHESIVES. *Proceedings of the Annual Meeting of the Adhesion Society*, 2013, Available at:

https://www.adhesionsociety.org/wp-content/uploads/2013-Annual-Meeting-Abstracts/Khaled_The_2013.pdf

[128] W. B. Khaled and D. Sameoto. Fabrication and characterization of thermoplastic elastomer dry adhesives with high strength and low contamination. *ACS Appl. Mater. Interfaces* 2014. Available: <http://dx.doi.org/10.1021/am500616a>.

Appendix

Macro code for the hot-embossing:

SU-8 H4.mcr

Close door()

Open File Protocol (New, View, Print=0(0,1,2))

Open File Measure()

Initialize Force Control (true/false=0)

Heating (Top=65.0°C, Bottom=60.0°C)

Close Chamber()

Evacuate Chamber()

Wait Time (Time = 30.00s)

Position relative (Position= 20.00000mm, Velocity= 10.00000mm/min)

Show Chart Window(Show/Hide =11/0)

Touch Force (Force =100N)

Temperature >=(Temperature= 60.0 deg, Channel=12)

Temper(Top= 65.0 deg, Bottom= 65.0 deg)

Force-Force controlled (Force=50N, Velocity= 0.50000mm/min)

Wait Time (Time= 300.00s)

Force-Force controlled (Force= 50N, Velocity= 0.50000mm/min)

Wait Time (Time= 120.00s)

Cooling (Top=30.0deg, Bottom= 30.0deg)

Temperature <=(Temperature=40.0deg, Channel =12)

Temper (Top= 30.0 deg, Bottom= 30.0 deg)

Wait Time (Time=60.00s)

Open Chamber fast()

Close File Measure()

Show Chart Window (Show/Hide= 01/0)

Step-by-Step Hot-embossing Technique:

- 1) Spin SU-8 2005 at 3000 rpm on a 4 x 4 in² clean borofloat glass substrate to produce a 4.5 μm thick layer.
- 2) Prebake at 90 °C for 5 minutes in a convection oven followed by exposure to 160 mJ/cm² of UV through mask 1.
- 3) Post-exposure bake at 90°C for 30 minutes.
- 4) Spin develop with SU-8 developer to produce arrays of circular and square caps.
- 5) Spin a thin layer of HPR 504 at 500 rpm for 5 s followed by 3000 rpm for 40 s.
- 6) Expose to $\sim 30\text{mJ/cm}^2$ of UV through mask 2 and develop in 354 developer until it looks visibly developed to create a mask for subsequent RIE.
- 7) Etch down a defect of around 800nm deep by RIE using the following parameters: 100 sccm of O₂ and 5 sccm of CF₄ (which is equivalent to 11.7 % flow rate in the μ -etch, nanoFab), 150 W (50 % in μ -etch, nanoFab) RF power and 125 millitorr chamber pressure.
- 8) Remove the residual HPR 504 by blanket exposure to UV development in 354 developer. This will create the positive mold for the stamp.
- 9) Silanize the mold for 2 hours and make a negative template with PDMS. Use a rubber ring and teflon coated glass plate on top to ensure uniform thickness of the PDMS template.
- 10) Spin a 4.5 μm layer of SU-8 on PMMA using the same parameters as outlined in step 1.
- 11) Prebake to remove the solvents at 90 °C in a convection oven for 5 min.
- 12) Put the PMMA substrate in the hot-embosser with the negative PDMS template on it. Make sure there is no trapped air in between them.
- 13) Use the hot-embossing macro SU8_H4.mcr to emboss the structures. Change the embossing parameters if necessary.
- 14) After the embossing is complete, blanket expose the embossed PMMA substrate to UV followed by baking at 90 °C for 30 minute.
- 15) Reactive ion etch to remove excess SU-8 using the following parameters: 75 sccm (75 %) of O₂, 59.5 sccm (25 % of CF₄), 150 W (50 %) RF power, 125 millitorr chamber pressure, 15 minute (optimum time is between 12-15 minute).
- 16) Expose to DUV and develop in SU-8 developer for the required amount of time. The development time was around 20 minute for W3 mold.

Bibliography

- [1] K. Autumn. Properties, principles, and parameters of the gecko adhesive system. *Biological Adhesives*, Springer, Berlin, 225-256. 2006. Available: http://dx.doi.org/10.1007/978-3-540-31049-5_12.
- [2] K. Autumn, M. Sitti, Y. A. Liang, A. M. Peattie, W. R. Hansen, S. Sponberg, T. W. Kenny, R. Fearing, J. N. Israelachvili and R. J. Full, "Evidence for van der Waals adhesion in gecko setae," *Proceedings of the National Academy of Sciences*, **99**, 12252-12256, September 17, 2002.
- [3] G. Huber, H. Mantz, R. Spolenak, K. Mecke, K. Jacobs, S. N. Gorb and E. Arzt. Evidence for capillarity contributions to gecko adhesion from single spatula nanomechanical measurements. *Proceedings of the National Academy of Sciences of the United States of America*. **102**(45), 16293-16296, 2005. Available: <http://www.pnas.org/content/102/45/16293.abstract>.
- [4] W. Sun, P. Neuzil, T. S. Kustandi, S. Oh and V. D. Samper. The nature of the gecko lizard adhesive force. *Biophysics Journal*, **89**(2), L14-L17, 2005.
- [5] P. H. Niewiarowski, S. Lopez, L. Ge, E. Hagan and A. Dhinojwala. Sticky gecko feet: The role of temperature and humidity. *PLoS ONE*, **3**(5), 2192, 2008. Available: <http://dx.plos.org/10.1371/journal.pone.0002192>.
- [6] J. B. Puthoff, M. S. Prowse, M. Wilkinson and K. Autumn. Changes in materials properties explain the effects of humidity on gecko adhesion. *The Journal of Experimental Biology*, **213**(21), 3699-3704, 2010.
- [7] M. S. Prowse, M. Wilkinson, J. B. Puthoff, G. Mayer and K. Autumn. Effects of humidity on the mechanical properties of gecko setae. *Acta Biomaterialia*, **7**(2), 733-738. 2011.
- [8] J. N. Israelachvili. *Intermolecular and Surface Forces*, 3rd edition, Elsevier, 2011.
- [9] J. Kwak and T. Kim. A review of adhesion and friction models for gecko feet. *International Journal of Precision Engineering and Manufacturing*, **11**(1), 171-186. 2010. Available: <http://dx.doi.org/10.1007/s12541-010-0020-5>.
- [10] R. S. Bradley. LXXIX. the cohesive force between solid surfaces and the surface energy of solids. *Philosophical Magazine Series 7*, **13**(86), 853-862. 1932. Available: <http://www.tandfonline.com/doi/abs/10.1080/14786449209461990>.
- [11] H. Hertz. On the contact of elastic solids. *J.Reine Angew.Math*, **92**(156-171), 110. 1881.

- [12] K. L. Johnson, K. Kendall and A. D. Roberts. Surface energy and the contact of elastic solids. *Proceedings of the Royal Society of London. A. Mathematical and Physical Sciences*, **324**(1558), 301-313. 1971.
- [13] D. Tabor. Surface forces and surface interactions. *Journal of Colloid Interface Science*, **58**(1), 2-13. 1977.
- [14] V. M. Muller, V. S. Yushchenko and B. V. Derjaguin. On the influence of molecular forces on the deformation of an elastic sphere and its sticking to a rigid plane. *Journal of Colloid Interface Science*, **77**(1), 91-101. 1980.
- [15] B. V. Derjaguin, V. M. Muller and Y. P. Toporov. Effect of contact deformations on the adhesion of particles. *Journal of Colloid Interface Science*, **53**(2), 314-326. 1975.
- [16] D. Maugis. Adhesion of spheres: The JKR-DMT transition using a dugdale model. *Journal of Colloid Interface Science*, **150**(1), 243-269, 1992.
- [17] Y. - Zhao, L. S. Wang and T. X. Yu. Mechanics of adhesion in MEMS—a review. *Journal of Adhesion Science and Technology*, **17**(4), 519-546. 2003. Available: <http://dx.doi.org/10.1163/15685610360554393>.
- [18] R. Spolenak, S. Gorb, H. Gao and E. Arzt. Effects of contact shape on the scaling of biological attachments. *Proceedings of the Royal Society A: Mathematical, Physical and Engineering Science*, **461**(2054), 305-319. 2005.
- [19] K. Kendall. The adhesion and surface energy of elastic solids. *Journal of Physics D: Applied Physics*, **4**(8), 1186, 1971. Available: <http://stacks.iop.org/0022-3727/4/i=8/a=320>.
- [20] M. Kamperman, E. Kroner, A. Del Campo, R. M. McMeeking and E. Arzt. Functional adhesive surfaces with "gecko" effect: The concept of contact splitting. *Advanced Engineering Materials*, **12**(5), 335-348, 2010. Available: <http://dx.doi.org/10.1002/adem.201000104>.
- [21] H. Gao, X. Wang, H. Yao, S. Gorb and E. Arzt. Mechanics of hierarchical adhesion structures of geckos. *Mechanics of Materials*, **37**(2-3), 275-285, 2005. Available: <http://dx.doi.org/10.1016/j.mechmat.2004.03.008>.
- [22] K. Kendall. Thin-film peeling-the elastic term. *Journal of Physics D: Applied Physics*, **8**(13), 1449, 1975. Available: <http://stacks.iop.org/0022-3727/8/i=13/a=005>.
- [23] K. Autumn. Gecko adhesion: Structure, function, and applications. *MRS Bulltin*, **32**(6), 473-478, 2007.
- [24] K. Jin, Y. Tian, J. S. Erickson, J. Puthoff, K. Autumn and N. S. Pesika. Design and fabrication of Gecko-inspired adhesives. *Langmuir*, **28**, 5737-5742, 2012.

- [25] K. Autumn and W. Hansen. Ultrahydrophobicity indicates a non-adhesive default state in gecko setae. *Journal of Comparative Physiology A*, **192**(11), 1205-1212, 2006. Available: <http://dx.doi.org/10.1007/s00359-006-0149-y>.
- [26] N. W. Rizzo, K. H. Gardner, D. J. Walls, N. M. Keiper-Hrynko, T. S. Ganzke and D. L. Hallahan. *Journal of the Royal Society Interface*, **3**(8), 441-451, 2006.
- [27] B. Zhao, N. Pesika, H. Zeng, Z. Wei, Y. Chen, K. Autumn, K. Turner and J. Israelachvili. Role of tilted adhesion fibrils (setae) in the adhesion and locomotion of gecko-like systems. *The Journal of Physical Chemistry B*, **113**(12), 3615-3621, 2009. Available: <http://dx.doi.org/10.1021/jp806079d>.
- [28] K. Autumn, Y. A. Liang, S. T. Hsieh, W. Zesch, W. P. Chan, T. W. Kenny, R. Fearing and R. J. Full. Adhesive force of a single gecko foot-hair. *Nature*, **405**(6787), 681-685, 2000. Available: <http://dx.doi.org/10.1038/35015073>.
- [29] B. Zhao, N. Pesika, K. Rosenberg, Y. Tian, H. Zeng, P. McGuiggan, K. Autumn and J. Israelachvili. Adhesion and friction force coupling of gecko setal arrays: implications for structured adhesive surfaces. *Langmuir*, **24**(4), 1517-1524, 2008. Available: <http://dx.doi.org/10.1021/la702126k>.
- [30] K. Autumn, A. Dittmore, D. Santos, M. Spenko and M. Cutkosky. Frictional adhesion: A new angle on gecko attachment. *Journal of Experimental Biology*, **209**(18), 3569-3579, 2006.
- [31] J. Lee, R. S. Fearing and K. Komvopoulos. Directional adhesion of gecko-inspired angled microfiber arrays. *Applied Physics Letters*, **93**(19), 191910, 2008. Available: <http://dx.doi.org/10.1063/1.3006334>.
- [32] H. E. Jeong, J. Lee, H. N. Kim, S. H. Moon and K. Y. Suh. A nontransferring dry adhesive with hierarchical polymer nanohairs. *Proceedings of the National Academy of Sciences*, **106**(14), 5639-5644, 2009. Available: <http://www.pnas.org/content/106/14/5639.abstract>.
- [33] M. K. Kwak, H. E. Jeong, W. G. Bae, H. Jung and K. Y. Suh. Anisotropic adhesion properties of triangular-tip-shaped micropillars. *Small*, **7**(16), 2296-2300, 2011. Available: <http://dx.doi.org/10.1002/sml.201100455>.
- [34] M. P. Murphy, B. Aksak and M. Sitti. Gecko-inspired directional and controllable adhesion. *Small*, **5**(2), 170-175, 2009. Available: <http://dx.doi.org/10.1002/sml.200801161>.
- [35] S. Kim, M. Spenko, S. Trujillo, B. Heyneman, D. Santos and M. R. Cutkosky. Smooth vertical surface climbing with directional adhesion. *IEEE Transactions on Robotics*, **24**(1), 65-74, 2008. Available: <http://dx.doi.org/10.1109/TRO.2007.909786>.

- [36] J. Tamelier, S. Chary and K. L. Turner, "Vertical anisotropic microfibers for a gecko-inspired adhesive," *Langmuir*, **28**, 8746-8752, 2012.
- [37] D. Sameoto, H. Sharif, J. P. Díaz Téllez, B. Ferguson and C. Menon. Nonangled anisotropic elastomeric dry adhesives with tailorable normal adhesion strength and high directionality. *Journal of Adhesion Science and Technology*, **28**(3-4), 1-13, 2012. Available: <http://dx.doi.org/10.1080/01694243.2012.693809>.
- [38] M. Moon, T. Cha, K. Lee, A. Vaziri and H. Kim. Tilted janus polymer pillars. *Soft Matter*, **6**(16), 3924-3929, 2010. Available: <http://dx.doi.org/10.1039/c0sm00126k>.
- [39] M. Zhou, K. Liu, J. Wan, X. Li, K. Jiang, H. Zeng, X. Zhang, Y. Meng, S. Wen, H. Zhu and Y. Tian. Anisotropic interfacial friction of inclined multiwall carbon nanotube array surface. *Carbon*, **50**(15), 5372-5379, 2012. Available: <http://www.sciencedirect.com/science/article/pii/S000862231200601X>.
- [40] D. Sameoto and C. Menon. Direct molding of dry adhesives with anisotropic peel strength using an offset lift-off photoresist mold, *Journal of Micromechanics and Microengineering*, **19**(11), 115026, 2009.
- [41] P. L. Dickrell, S. B. Sinnott, D. W. Hahn, N. R. Raravikar, L. S. Schadler, P. M. Ajayan and W. G. Sawyer. Frictional anisotropy of oriented carbon nanotube surfaces. *Tribology Letters*, **18**(1), 59-62, 2005. Available: <http://dx.doi.org/10.1007/s11249-004-1752-0>.
- [42] L. Ge, S. Sethi, L. Ci, P. M. Ajayan and A. Dhinojwala. Carbon nanotube-based synthetic gecko tapes. *Proceedings of the National Academy of Sciences*, **104**(26), 10792-10795. 2007.
- [43] R. T. Pack, J. L. Christopher Jr. and K. Kawamura. A rubber-tuator-based structure-climbing inspection robot. *Proceedings of IEEE International Conference on Robotics and Automation*, 1997.
- [44] T. Yano, T. Suwa, M. Murakami and T. Yamamoto. Development of a semi self-contained wall climbing robot with scanning type suction cups. *Proceedings of the IEEE/RSJ International Conference on Intelligent Robots and Systems*, 1997.
- [45] A. Nagakubo and S. Hirose. Walking and running of the quadruped wall-climbing robot. *Proceedings of IEEE International Conference on Robotics and Automation*, 1994 .
- [46] G. La Rosa, M. Messina, G. Muscato and R. Sinatra. A low-cost lightweight climbing robot for the inspection of vertical surfaces. *Mechatronics*, **12**(1), 71-96, 2002.
- [47] J. Zhu, D. Sun and S. Tso. Development of a tracked climbing robot. *Journal of Intelligent and Robotic Systems*, **35**(4), 427-443, 2002. Available: <http://dx.doi.org/10.1023/A%3A1022383216233>.

- [48] A. Parness, T. Hilgendorf, P. Daniel, M. Frost, V. White and B. Kennedy. Controllable ON-OFF adhesion for earth orbit grappling applications. *Proceedings of IEEE Aerospace Conference*, 2013.
- [49] K. Daltorio, S. Gorb, A. Peressadko, A. Horchler, R. Ritzmann and R. Quinn. "A robot that climbs walls using micro-structured polymer feet," *Proceedings of the 8th International Conference on Climbing and Walking Robots and the Support Technologies for Mobile Machines*, 2006. Available: http://dx.doi.org/10.1007/3-540-26415-9_15.
- [50] E. W. Hawkes, E. V. Eason, A. T. Asbeck and M. R. Cutkosky. The gecko's toe: Scaling directional adhesives for climbing applications. *IEEE Xplore*, **18**(2), 2012. Available: <http://dx.doi.org/10.1109/TMECH.2012.2209672>.
- [51] C. Menon, M. Murphy and M. Sitti. Gecko inspired surface climbing robots. *Proceedings of IEEE International Conference on Robotics and Biomimetics*, 2004.
- [52] B. Aksak, M. P. Murphy and M. Sitti. Gecko inspired micro-fibrillar adhesives for wall climbing robots on micro/nanoscale rough surfaces. *Proceedings of IEEE International Conference on Robotics and Automation*, 2008.
- [53] M. Henrey, J. Krahn, A. Ahmed, K. Wormnes and C. Menon. Climbing with structured dry adhesives: sticky robots for scaling smooth vertical surfaces, *Proceedings of ASTRA 13*, 2013.
- [54] Y. Menguc, S. Y. Yang, S. Kim, J. A. Rogers and M. Sitti. Gecko-inspired controllable adhesive structures applied to micromanipulation. *Advanced Functional Materials*, **22**(6), pp. 1246-1254. 2012. Available: <http://dx.doi.org/10.1002/adfm.201101783>.
- [55] A. Carlson, H. Kim-Lee, J. Wu, P. Elvikis, H. Cheng, A. Kovalsky, S. Elgan, Q. Yu, P. M. Ferreira, Y. Huang, K. T. Turner and J. A. Rogers. Shear-enhanced adhesiveless transfer printing for use in deterministic materials assembly. *Applied Physics Letters*, **98**(26), 2011. Available: <http://dx.doi.org/10.1063/1.3605558>.
- [56] S. Kim, J. Wu, A. Carlson, S. H. Jin, A. Kovalsky, P. Glass, Z. Liu, N. Ahmed, S. L. Elgan, W. Chen, P. M. Ferreira, M. Sitti, Y. Huang and J. A. Rogers. Microstructured elastomeric surfaces with reversible adhesion and examples of their use in deterministic assembly by transfer printing. *Proceedings of the National Academy of Sciences*, **107**(40), 17095-17100, 2010.
- [57] S. Y. Yang, A. Carlson, H. Cheng, Q. Yu, N. Ahmed, J. Wu, S. Kim, M. Sitti, P. M. Ferreira, Y. Huang and J. A. Rogers. Elastomer surfaces with directionally dependent adhesion strength and their use in transfer printing with continuous roll-to-roll applications. *Advanced Materials*, **24**(16), 2117-2122. 2012. Available: <http://dx.doi.org/10.1002/adma.201104975>.
- [58] Ferguson, B. J. Improved Gecko Inspired Dry Adhesives Applied to the Packaging of MEMS. MSc Thesis, University of Alberta, Edmonton, Canada, 2013..

- [59] M. K. Kwak, H. Jeong and K. Y. Suh. Rational design and enhanced biocompatibility of a dry adhesive medical skin patch. *Adv Mater* 23(34), pp. 3949-3953, 2011. Available: <http://dx.doi.org/10.1002/adma.201101694>.
- [60] D. Sameoto and C. Menon, Deep UV patterning of acrylic masters for molding biomimetic dry adhesives, *Journal of Micromechanics and Microengineering*, **20**, 115037, 2010.
- [61] D. Sameoto and B. Ferguson. Robust large-area synthetic dry adhesives. *Journal of Adhesion Science and Technology*, **28**(3-4), 1-17, 2012. Available: <http://dx.doi.org/10.1080/01694243.2012.693802>.
- [62] G. Carbone, E. Pierro and S. N. Gorb. Origin of the superior adhesive performance of mushroom-shaped microstructured surfaces. *Soft Matter*, **7**(12), 5545-5552, 2010.
- [63] G. Carbone and E. Pierro. A review of adhesion mechanisms of mushroom-shaped microstructured adhesives. *Meccanica*, **48**(8), 1819-1833, 2013. Available: <http://dx.doi.org/10.1007/s11012-013-9724-9>.
- [64] A. V. Spuskanyuk, R. M. McMeeking, V. S. Deshpande and E. Arzt. The effect of shape on the adhesion of fibrillar surfaces. *Acta Biomaterialia*, **4**(6), 1669-1676, 2008. Available: <http://www.sciencedirect.com/science/article/pii/S1742706108001645>.
- [65] Walid Bin Khaled and Dan Sameoto. Anisotropic dry adhesive via cap defects. *Bioinspiration & Biomimetics*, **8**(4), 044002, 2013. Available: <http://stacks.iop.org/1748-3190/8/i=4/a=044002>.
- [66] Juvinall R C and Marshek K M, *Fundamentals of Machine Component Design*. New York: Wiley, 1991.
- [67] Thomson W T and Dahleh M D, *Theory of Vibrations with Application*. New Jersey: Prentice Hall, 1998.
- [68] D. Paretkar, M. Kamperman, D. Martina, J. Zhao, C. Creton, A. Lindner, A. Jagota, R. McMeeking and E. Arzt. Preload-responsive adhesion: Effects of aspect ratio, tip shape and alignment. *Journal of the Royal Society Interface*, **10**(83), 2013. Available: <http://dx.doi.org/10.1098/rsif.2013.0171>.
- [69] D. Sameoto. Dry adhesives for MEMS assembly, manipulation and integration: Progress and challenges. *Proceedings of 5th International Symposium on Dielectrics for Nanosystems: Materials Science, Processing, Reliability and Manufacturing*, 2012. Available: <http://dx.doi.org/10.1149/1.3700916>.
- [70] M Haiducu and M Rahbar and I G Foulds and R W Johnstone and D Sameoto and M. Parameswaran. Deep-UV patterning of commercial grade PMMA for low-cost, large-scale microfluidics. *Journal of Micromechanics and Microengineering*, **18**(11), 115029, 2008. Available: <http://stacks.iop.org/0960-1317/18/i=11/a=115029>.

- [71] D. Sameoto, Y. Li and C. Menon. Micromask generation for polymer morphology control: Nanohair fabrication for synthetic dry adhesives. *Proceedings of 3rd International Conference on Smart Materials, Structures and Systems - Smart Materials and Micro/Nanosystems*, 2008.
- [72] B. Kim, S. Lee, J. Lee, S. Cho, H. Park, S. Yeom and S. Park. A comparison among neo-hookean model, mooney-rivlin model, and ogden model for chloroprene rubber. *International Journal of Precision Engineering and Manufacturing*, **13**(5), pp. 759-764, 2012. Available: <http://dx.doi.org/10.1007/s12541-012-0099-y>.
- [73] A. Ali, M. Hosseini and B. B. Sahari. A review of constitutive models for rubber-like materials. *American Journal of Engineering and Applied Sciences*, **3**(1), 232-9, 2010. Available: <http://dx.doi.org/10.3844/ajeassp.2010.232.239>.
- [74] Bscheiden B, Ferguson B and Sameoto D, Hyperelastic simulation for accurate prediction of gecko inspired dry adhesive deformed shape and stress distribution prior to detachment, *Proceedings of the Annual Meeting of the Adhesion Society*, 2013.
- [75] G. Carbone, E. Pierro and S. N. Gorb. Origin of the superior adhesive performance of mushroom-shaped microstructured surfaces. *Soft Matter*, **7**(12), 5545-5552, 2011. Available: <http://dx.doi.org/10.1039/C0SM01482F>.
- [76] Spuskanyuk, A.V.; McMeeking, R.M.; Deshpande, V.S.; Arzt, E. The effect of shape on the adhesion of fibrillar adhesives; *Acta Biomaterialia*, **4**(6), 1669-1676, 2008.
- [77] H. Gao and H. Yao. Shape insensitive optimal adhesion of nanoscale fibrillar structures. *Proceedings of the National Academy of Sciences of the United States of America*, **101**(21), 7851-7856. 2004.
- [78] D. Sameoto and C. Menon, "Recent advances in the fabrication and adhesion testing of biomimetic dry adhesives," *Smart Materials and Structure*, **19**(10), 2010.
- [79] B. Aksak, M. P. Murphy and M. Sitti. Adhesion of biologically inspired vertical and angled polymer microfiber arrays. *Langmuir*, **23**(6), 3322-3332, 2007. Available: <http://dx.doi.org/10.1021/la062697t>.
- [80] BJB Enterprises. ST-1060 A/B Data Sheet. <http://www.bjbenterprises.com/pdf/ST-1060.pdf>; Date accessed: March 23 2014.
- [81] M. B. Ranade. Adhesion and removal of fine particles on surfaces. *Aerosol Science and Technology*, **7**(2), 161-176. 1987.
- [82] S. Kim, A. Carlson, H. Cheng, S. Lee, Jung-Ki Park, Y. Huang and J. A. Rogers. Enhanced adhesion with pedestal-shaped elastomeric stamps for transfer printing. *Applied Physics Letters*, **100**(17), 171909, 2012. Available: <http://dx.doi.org/10.1063/1.4706257>.

- [83] A. Carlson, H. Kim-Lee, J. Wu, P. Elvikis, H. Cheng, A. Kovalsky, S. Elgan, Q. Yu, P. M. Ferreira, Y. Huang, K. T. Turner and J. A. Rogers. Shear-enhanced adhesiveless transfer printing for use in deterministic materials assembly. *Applied Physics Letters*, **98**(26), 2011. Available: <http://dx.doi.org/10.1063/1.3605558>.
- [84] D. Sameoto. Dry adhesives for MEMS assembly, manipulation and integration: Progress and challenges. *Proceedings of 5th International Symposium on Dielectrics for Nanosystems: Materials Science, Processing, Reliability and Manufacturing*, 2012. Available: <http://dx.doi.org/10.1149/1.3700916>.
- [85] D. Sameoto and C. Menon; A low-cost, high-yield fabrication method for producing optimized biomimetic dry adhesives, *J Micromech Microengineering*, **19**, 115002, 2009.
- [86] Y. Li, D. Sameoto and C. Menon. Properties validation of an anisotropic dry adhesion designed for legged climbing robots, *Proceedings of IEEE International Conference on Robotics and Biomimetics*, 1906-1911, 2009.
- [87] C. Greiner, E. Arzt and A. del Campo. Hierarchical Gecko-like adhesives, *Advanced Materials*, **21**(4), 479-482, 2009.
- [88] A. Parness, D. Soto, N. Esparza, N. Gravish, M. Wilkinson, K. Autumn and M. Cutkosky. *Journal of the Royal Society Interface*, **6**(41), 1223-1232.
- [89] S. Vajpayee, R. Long, L. Shen, A. Jagota and C. Hui. Effect of rate on adhesion and static friction of a film-terminated fibrillar interface. *Langmuir*, **25**(5), 2765-2771. 2009. Available: <http://dx.doi.org/10.1021/la8033885>.
- [90] E. Cheung and M. Sitti. Adhesion of biologically inspired polymer microfibers on soft surfaces. *Langmuir*, **25**(12), 6613-6616. 2009. Available: <http://dx.doi.org/10.1021/la900997p>.
- [91] S. Kim and M. Sitti. Biologically inspired polymer microfibers with spatulate tips as repeatable fibrillar adhesives. *Applied Physics Letters*, **89** (26), 261911-261913, 2006.
- [92] M. P. Murphy, B. Aksak and M. Sitti. Adhesion and anisotropic friction enhancements of angled heterogeneous micro-fiber arrays with spherical and spatula tips. *Journal of Adhesion Science & Technology*, **21**(12), 1281-1296, 2007.
- [93] Y. Xia and G. M. Whitesides. SOFT LITHOGRAPHY. *Annual Review of Materials Science*, **28**(1), 153-184. 1998. Available: <http://dx.doi.org/10.1146/annurev.matsci.28.1.153>.
- [94] J. Krahn and C. Menon, "Electro-dry-adhesion," *Langmuir*, **28**, 5438-5443, 2012.
- [95] L. Yang, N. Shirahata, G. Saini, F. Zhang, L. Pei, M. C. Asplund, D. G. Kurth, K. Ariga, K. Sautter, T. Nakanishi, V. Smentkowski and M. R. Linford. Effect of surface free energy on PDMS transfer in microcontact printing and its application to ToF-SIMS to probe

surface energies. *Langmuir*, **25**(10), 5674-5683, 2009. Available: <http://dx.doi.org/10.1021/la804272n>.

[96] J. A. Wigenius, M. Hamed and O. Inganäs. Limits to Nanopatterning of Fluids on Surfaces in Soft Lithography, *Advanced Functional Materials*, **18**(17), 2563-2571, 2008.

[97] S. Yunus, D. L. De Crombrughe, C. Poleunis and A. Delcorte. Diffusion of oligomers from polydimethylsiloxane stamps in microcontact printing: Surface analysis and possible application. *Surface Interface Analysis*, **39**(12-13), 922-925, 2007. Available: <http://dx.doi.org/10.1002/sia.2623>.

[98] R. B. A. Sharpe, D. Burdinski, C. D. Van Marel, J. A. J. Jansen, J. Huskens, H. J. W. Zandvliet, D. N. Reinhoudt and B. Poelsema. Ink dependence of poly(dimethylsiloxane) contamination in microcontact printing. *Langmuir*, **22**(13), 5945-5951. 2006. Available: <http://dx.doi.org/10.1021/la053298l>.

[99] K. Glasmastar, J. Gold, A. Andersson, D. S. Sutherland and B. Kasemo. Silicone transfer during microcontact printing. *Langmuir*, **19**(13), 5475-5483, 2003. Available: <http://dx.doi.org/10.1021/la026558x>.

[100] D. J. Graham, D. D. Price and B. D. Ratner. Solution assembled and microcontact printed monolayers of dodecanethiol on gold: A multivariate exploration of chemistry and contamination. *Langmuir*, **18**(5), 1518-1527, 2002. Available: <http://dx.doi.org/10.1021/la010059z>.

[101] I. Böhm, A. Lampert, M. Buck, F. Eisert and M. Grunze. A spectroscopic study of thiol layers prepared by contact printing. *Applied Surface Science*, **141**(3-4), 237-243. 1999.

[102] Y. Zhou, R. Valiokas and B. Liedberg. Structural characterization of microcontact printed arrays of hexa(ethylene glycol)-terminated alkanethiols on gold. *Langmuir*, **20**(15), 6206-6215, 2004. Available: <http://dx.doi.org/10.1021/la049421a>.

[103] B. A. Langowski and K. E. Uhrich. Oxygen plasma-treatment effects on si transfer. *Langmuir*, **21**(14), 6366-6372. 2005. Available: <http://dx.doi.org/10.1021/la046795v>.

[104] N. R. Thomson, C. L. Bower and D. W. McComb. Identification of mechanisms competing with self-assembly during directed colloidal deposition. *Journal of Materials Chemistry*, **18**(21), 2500-2505.

[105] A. Perl, M. Peter, B. J. Ravoo, D. N. Reinhoudt and J. Huskens. Heavyweight dendritic inks for positive microcontact printing. *Langmuir*, **22**(18), 7568-7573. 2006. Available: <http://dx.doi.org/10.1021/la060625w>.

[106] Y. Zhao, M. Li, Q. Lu and Z. Shi. Superhydrophobic polyimide films with a hierarchical topography: Combined replica molding and layer-by-layer assembly. *Langmuir*, **24**(21), 12651-12657, 2008. Available: <http://dx.doi.org/10.1021/la8024364>.

- [107] N. Iyer, N. Saka and Jung-Hoon Chun. Contamination of silicon surface due to contact with solid polymers. *Proceedings of IEEE Transactions on Semiconductor Manufacturing*, **14**, 85-96, 2001.
- [108] D. Trimbach, H. Stapert, J. van Orselen, K. Jandt, C. Bastiaansen and D. Broer. Improved Microcontact Printing of Proteins using Hydrophilic Thermoplastic Elastomers as Stamp Materials. *Advanced Engineering Materials*, **9**(12), 1123-1128, 2007
- [109] A. L. Briseno, M. Roberts, M. Ling, H. Moon, E. J. Nemanick and Z. Bao. Patterning organic semiconductors using Dry² poly(dimethylsiloxane) elastomeric stamps for thin film transistors. *Journal of the American Chemical Society*, **128**(12), 3880-3881, 2006. Available: <http://dx.doi.org/10.1021/ja058226v>.
- [110] Z. Yang, A. M. Belu, A. Liebmann-Vinson, H. Sugg and A. Chilkoti. Molecular imaging of a micropatterned biological ligand on an activated polymer surface. *Langmuir*, **16**(19), 7482-7492, 2000. Available: <http://dx.doi.org/10.1021/la0000623>.
- [111] X. Wang, M. Östblom, T. Johansson and O. Inganäs. PEDOT surface energy pattern controls fluorescent polymer deposition by dewetting. *Thin Solid Films*, **449**(1-2), 125-132, 2004.
- [112] B. D. - Ratner and D. G. Castner. *Surface Analysis-The Principle Techniques*, Chapter 2, John Wiley and Sons, 2009
- [113] Vickerman J C and Gilmore I S, *Surface Analysis- the Principal Techniques*. Singapore: Wiley, 2009.
- [114] The NIST reference on constants, units and uncertainty. National Institute of Standards and Technology, Available at: <http://physics.nist.gov/cgi-bin/cuu/Value?h>. Date accessed: March 25, 2014.
- [115] S. Kim, E. Cheung and M. Sitti. Wet self-cleaning of biologically inspired elastomer mushroom shaped microfibrillar adhesives. *Langmuir* **25**(13), pp. 7196-7199. 2009. Available: <http://dx.doi.org/10.1021/la900732h>.
- [116] M. D. Bartlett, A. B. Croll, D. R. King, B. M. Paret, D. J. Irschick and A. J. Crosby. Looking beyond fibrillar features to scale gecko-like adhesion. *Adv Mater* **24**(8), pp. 1078-1083. 2012. Available: <http://dx.doi.org/10.1002/adma.201104191>.
- [117] Nanolab Technologies XPS Binding Energies(BE) and Scofield's Relative Sensitivity Factor (RSF) Chart. Available at: <http://www.nanolabtechnologies.com/pdf/Scofield-Table-of-BEs-and-RSFs.pdf>; Date accessed: March 23 2014.
- [118] N. Lakhera, A. Graucob, A. S. Schneider, E. Kroner, E. Arzt, C. M. Yakacki and C. P. Frick. Effect of viscoelasticity on the spherical and flat adhesion characteristics of photopolymerizable acrylate polymer networks. *International Journal of Adhesion and*

- Adhesives*. **44**, 184-194. 2013. Available:
<http://www.sciencedirect.com/science/article/pii/S0143749613000456>.
- [119] Kraton Performance Polymers Inc Brochure, Kraton Polymers. Available at:
<http://docs.kraton.com/kraton/attachments/downloads/81311AM.pdf>; Date accessed:
 March 23, 2014.
- [120] E. Roy, J. Galas and T. Veres. Thermoplastic elastomers for microfluidics: Towards a high-throughput fabrication method of multilayered microfluidic devices. *Lab Chip* **11**(18), pp. 3193-3196. 2011. Available: <http://dx.doi.org/10.1039/C1LC20251K>.
- [121] Kraton Polymers Kraton G1645 M Polymer Data Sheet; Available at:
http://docs.kraton.com/tl_warehouse/pdf_data_docs/WG_4244_WG4F23.tmp.pdf;
 Date accessed: March 23, 2014.
- [122] Kraton Polymers Kraton G1657 M Polymer Data Sheet. Available at:
http://docs.kraton.com/tl_warehouse/pdf_data_docs/WG_4244_WG93AE.tmp.pdf;
 Date accessed: March 23, 2014.
- [123] E. Kroner, R. Maboudian and E. Arzt. Adhesion characteristics of PDMS surfaces during repeated pull-off force measurements. *Advanced Engineering Materials*, **12**(5), 398-404, 2010. Available: <http://dx.doi.org/10.1002/adem.201000090>.
- [124] J. Davies, S. Haq, T. Hawke and J. P. Sargent. A practical approach to the development of a synthetic gecko tape. *International Journal of Adhesion and Adhesives*, **29**(4), 380-390. 2009. Available:
<http://www.sciencedirect.com/science/article/pii/S0143749608000808>.
- [125] M. P. Murphy, S. Kim and M. Sitti. Enhanced adhesion by gecko-inspired hierarchical fibrillar adhesives. *ACS Applied Materials and Interfaces*, **1**(4), 849-855, 2009. Available: <http://dx.doi.org/10.1021/am8002439>.
- [126] W. B. Khaled and D. Sameoto. Manufacture of mushroom shaped dry adhesives by thermo-compression molding of thermoplastic elastomers. *Proceedings of the Annual Meeting of the Adhesion Society*, 2014. Available at:
http://www.adhesionsociety.org/wp-content/uploads/2014_Annual-Meeting/Abstracts/Khaled_2014_Extended_Abstract.pdf
- [127] W. B. Khaled and D. Sameoto. THE DELIBERATE DEFECT: A FACILE METHOD FOR MASS MANUFACTURE OF ANISOTROPIC DRY ADHESIVES. *Proceedings of the Annual Meeting of the Adhesion Society*, 2013, Available at:
https://www.adhesionsociety.org/wp-content/uploads/2013-Annual-Meeting-Abstracts/Khaled_The_2013.pdf
- [128] W. B. Khaled and D. Sameoto. Fabrication and characterization of thermoplastic elastomer dry adhesives with high strength and low contamination. *ACS Appl. Mater. Interfaces* 2014. Available: <http://dx.doi.org/10.1021/am500616a>.